Freie Universität Berlin

Kumulative Dissertation

Tectonic Signal Propagation into the Oligocene to early Miocene Upper Austrian Foreland Basin – a Comparison of different Methods

vorgelegt von

Julian Alexander Hülscher

Zur Erlangung des

Doktorgrades der Naturwissenschaften

im

Fachbereich Geowissenschaften

Institut für Geologische Wissenschaften

Fachrichtung Tektonik und Sedimentäre Systeme

Freie Universität Berlin

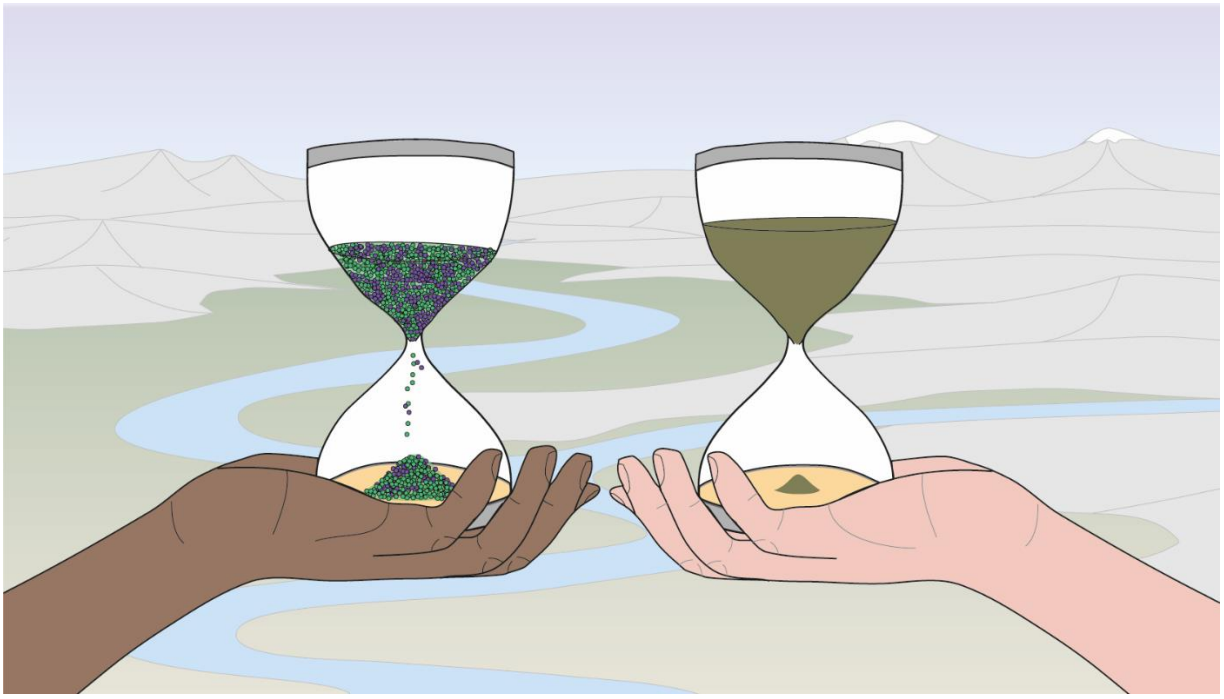

“A man who looks at a rock must have a lot on his mind.
Or nothing.”

Linda Hamilton – Rachel Wando in
Dante’s Peak (1997)

Eidesstattliche Erklärung

Hiermit erkläre ich, Julian Alexander Hülscher, dass diese Arbeit mit dem Titel „Tectonic Signal Propagation into the Oligocene to early Miocene Upper Austrian Foreland Basin – a Comparison of different Methods“ ausschließlich auf Grundlage der angegebenen Hilfsmittel und Hilfen selbstständig von mir verfasst wurde. Die Arbeit wurde nicht in einem früheren Promotionsverfahren eingereicht.

Diese Arbeit wurde vom Promotionsausschuss des Fachbereichs Geowissenschaften am 24. September 2021 genehmigt.

Erstgutachter: Prof. Dr. Anne Bernhardt
Zweitgutachter: Prof. Dr. Fritz Schlunegger

Die Disputation erfolgte am 11. Oktober 2021.

Berlin, den 11. Januar 2022

Julian Alexander Hülscher

Abstract

Changes in sediment flux, architecture, and/or provenance in the infill of peri-orogenic basins have been interpreted to argue for or against tectonic or climatic changes in the hinterland. However, our interpretation of these changes is still hampered because the progradation of such environmental signals in the sediment-routing system from source to sink is still poorly understood. The present work quantifies how quickly tectonic perturbations in the hinterland are recognizable in the sedimentary archive in geological deep-time (>10 Ma) by using several different proxies in the sediment-routing systems of the Oligocene/Miocene European Alps and its foreland basin in Upper Austria.

In a first step, the depositional ages of the sediments were constrained. Benthic foraminifera and geochemical analysis were carried out to identify lithostratigraphic boundaries and were combined with calcareous nannoplankton and stable carbon isotopy of bulk sediment analysis for absolute dating. Well-cutting samples were taken from three wells that penetrate the Puchkirchen Group and the overlying Hall Formation. During sedimentation of the Puchkirchen Group (26.9 – 19.6 Ma), eastward transport of sediment via a submarine channel controlled the depositional processes. The Base Hall Unconformity marks the beginning of the Hall Formation (19.6 – 18.1 Ma), in which the channel sedimentation ended at 19 Ma and deposition of northward progradation of clinoforms initiated.

Provenance information from the sand-sized sediment fraction in the Upper Austrian Northern Alpine Foreland Basin were gained by a single-grain apatite multi-proxy approach. Twenty-two sandstone samples of the Puchkirchen Group and the overlying Hall Formation were collected and connected with the newly acquired depositional ages. Apatites were analyzed for their trace-element geochemistry, fission track ages (AFT), U-Pb and Sm-Nd isotopic composition. The results revealed a provenance change at 23.3 Ma with increasing input from a late Variscan high-grade metamorphic Upper Austroalpine source with increased εNd values. Accompanied by decreasing AFT lag times after 24 Ma, the data suggest an exhumation event that started around 29-27 Ma in the Eastern Alps. Both findings are attributed to the surface response of the initial exhumation of the Tauern Window which triggered slow exhumation (0.3-0.6 mm/a) of the overlying Austroalpine units before the lateral escape towards the east at 23-21 Ma caused a significant increase in exhumation rates.

The provenance of the clay-sized sediment was constrained by Nd isotope analysis on 30 well-cutting samples. In contrast to the single-grain analysis, the bulk-rock clay analysis revealed a stable provenance with εNd values around -9.7 (± 0.5) from 27 to 19 Ma. However, after 19 Ma, the εNd values increased to -9.2 (± 0.5). The interpreted total signal lag time in response to the Tauern Window exhumation from 28 ± 1 Ma onward is significantly shorter (3.4 – 6 m.y.) in the sand-sized apatites compared to in the clay-sized fraction (8.0 – 10.3 m.y.). This delay is due to the different signal recording in the bulk-rock and single-grain methods. Whereas single-grain distributions of orogen-wide sediment-routing systems can be biased towards small source areas with high mineral-fertility and erosion rates, bulk-rock methods dilute such extreme values. This difference in provenance change recording delivers valuable information about the extent of the perturbated source area.

This study shows, how tectonic exhumation processes influence sediment architecture, flux, and provenance of a submarine, distal foreland basin over time. Especially the characterization of the same parameter (flux or provenance) of a sediment-routing system with different methods holds great potential for future research. As different methods highlight different characteristics of the same parameter, this combination enables a previously unattained understanding of underlying environmental changes.

Zusammenfassung

Veränderungen in sedimentären Akkumulationsraten, Architektur und/oder Herkunft in der Verfüllung von Vorlandbecken sind in der Vergangenheit dafür benutzt worden, für oder gegen tektonische oder klimatische Veränderungen im Liefergebiet zu argumentieren. Jedoch ist unser Verständnis dieser Veränderungen immer noch unvollständig, da die Weiterleitung dieser Signale von der Quelle bis zur Senke immer noch unvollständig verstanden ist. Diese Arbeit quantifiziert, wie schnell sich tektonische Hebungsereignisse im Hinterland in den Sedimenten des Vorlandes widerspiegeln. Dabei werden verschiedene Methodiken benutzt und das sedimentäre Verteilungssystem der Oligozänen/Miozänen Europäischen Alpen und ihres Vorlandes in Oberösterreich untersucht.

In einem ersten Schritt wurden die Ablagerungsalter der Sedimente bestimmt. Dafür wurden Analyse der benthischen Foraminiferen und der Gesamtgesteinsgeochemie durchgeführt und um Analysen des kalkigen Nannoplanktons und stabiler Kohlenstoffisotope ergänzt. Spülproben aus drei Bohrungen, die die Puchkirchen Gruppe und die darüber liegende Hall Formation durchschlagen, wurden beprobt. Während der Ablagerung der Puchkirchen Gruppe (26.9 – 19.6 Ma) war die Sedimentation im Becken durch den ostwärts gerichteten Sedimenttransport in einem submarinen, turbiditischen Kanal dominiert. Die Basale Hall Diskordanz markiert den Beginn der Hall Formation (19.6 – 18.1 Ma), in welcher die Sedimentation durch den turbiditischen Kanal endete (19 Ma) und die Progradation von Klinoformen nach Norden begann.

Die Herkunft der Sedimente der Sandkorngröße in der Oberöstereichischen Molasse wurde durch eine multimethodische Analyse der Apatiteinzelkörner bestimmt. 22 Sandsteinproben wurden dafür aus der Puchkirchen Gruppe und der Hall Formation entnommen und diese mit den neuen Ablagerungsaltern verknüpft. Die Apatite wurden auf ihre Spurenelementzusammensetzung, Spaltspuren (AFT), U-Pb und Sm-Nd Isotopie untersucht. Anhand dieser Ergebnisse konnte gezeigt werden, dass sich der Eintrag aus einer spätvariszischen, hochgradig metamorphen oberaustroalpinen Quelle mit erhöhten εNd Werten um 23.3 Ma erhöht. Dieser erhöhte Eintrag geht einher mit einer Verkürzung der AFT Latenzzeit, was zusammen darauf hindeutet, dass es von 29-27 Ma an zu einer schnelleren Exhumation in den Ostalpen kam. Die Ergebnisse werden als Resultat der Initiierung der langsamen Exhumierung (0.3-0.6 mm/a) des Tauern Fensters interpretiert.

Die Herkunft der Sedimente der Tonkorngröße wurde anhand von Nd Isotopenmessungen an 30 Spülproben bestimmt. Im Gegensatz zu den Apatitkörnern zeigen die Gesamtgesteins-messungen der Tonkorngröße eine stabile Herkunft zwischen 27 und 19 Ma mit einem εNd Wert um -9.7 (± 0.5). In den Proben mit Ablagerungsaltern <19 Ma steigen die εNd Werte auf -9.2 (± 0.5). Die totale Signallaufzeit in Reaktion auf die Tauernfensterexhumierung ab 28 ± 1 Ma ist sehr viel kürzer (3.4 – 6 m.y.) in den sandkorngroßen Apatiten, verglichen mit der Tonfraktion (8.0 – 10.3 m.y.). Diese Verspätung wird auf die unterschiedliche Signalübertragung zwischen der Gesamtgesteins- und Einzelkornmethodik zurückgeführt. Während Einzelkornverteilungen von gebirgsweiten Sedimentverteilungssystemen kleine Gebiete mit hoher Erosions- und Mineralfertilitätsrate überproportional abbilden, werden diese in Gesamtgesteinsmethodiken unterrepräsentiert und Extremwerte verwässert. Diese Unterschiede liefern wertvolle Informationen über die Größe des gestörten Quellengebiets.

Die vorliegende Studie zeigt, wie tektonische Exhumierungsprozesse sich in sedimentären Akkumulationsraten, Architektur und Herkunft eines tiefmarinen, distalen Vorlandbeckens widerspiegeln. Besonders die Bestimmung des gleichen Parameters (Akkumulationsraten oder Herkunft) eines Sedimentverteilungssystemen mit unterschiedlichen Methodiken hat großes Potential. Die verschiedenen Methodiken stellen unterschiedliche Aspekte des gleichen Parameters heraus, was ein zuvor unerreichtes Verständnisniveau der zugrundeliegenden Umweltveränderung ermöglicht.

Acknowledgements

In the last almost five years here at the FU Berlin I received a lot support from my family and many friends and colleagues without I wouldn't been able to finish this work. First and foremost, I have to thank my supervisors Anne Bernhardt and Ed Sobel who guided me through the depths and shallows of the work. I benefited greatly from their help, knowledge and experiences. At the same time, I always appreciated the freedom they gave me to make my own mistakes and experiences.
Furthermore, I would like to thank Patrick Grunert who introduced me to the field of marine Molasse stratigraphy. Gero Fischer was an indispensable help during the first two years when the both of us jumped into the biostratigraphy of the Upper Austrian Foreland. I owe particular thanks to the RAG Austria and their team for the support, trust and the access to their drill cores, well-cuttings and 3D seismic-reflection dataset.
In general, I have to thank my colleagues at the Campus Lankwitz who turned these years into a great period of time. Jan Pleuger, thanks for the beers, cigarettes, and discussions about Alpine geology, wine, and fishing. I would like to thank Lorenzo Gemignani for discussions about provenance and the detrital approach. Eline LeBreton helped me to better understand the basin evolution and the geodynamics of the greater Alpine area. I would like to thank Mark Handy for the discussions about slab-dynamics in the Oligocene/Miocene Alps and his comments on two manuscripts.
One of the greatest experiences I made at the Campus is that I found friends here. I would like to thank Philip Groß for the beers we drank together and the introduction into the Tauern Window geology. I thank Vincent Verwater for the discussions about the Southern Alps. Emanuel Kästle helped me to better understand the different geophysical methods and I enjoyed a couple of long evenings with him ("Hauschulzes Sitzfleisch"). Marc Grund provided venison and information about Albanian geology which I both enjoyed. I would like to thank Sarah Mosser for her view on statistics (keep fighting!) and the long coffee breaks, and Konstantin Huber, Saskia Bläsing, Charlotte Läuchli, Iris Wannhoff, and Sascha Zertani who made the time truly enjoyable.
Without my family this work would not have been possible, I have to thank them for their support, critic and guidance. Last but not least, Lena, thank you very much for all the sense and nonsense in my life.

Organization of this Thesis

The presented thesis is organized into five chapters. Whereas two of them have been published in peer-reviewed journals (Chapter 2) or accepted for publication (Chapter 3), Chapter 4 will be submitted to a peer-reviewed journal. In this section, the structure of the thesis and the contribution of the different authors to the chapters are outlined.

Chapter 1: Introduction

The chapter introduces the reader to the main topics of the thesis, outlines the research questions and the methods that were used to tackle those questions.

Chapter 2: Selective recording of tectonic forcings in an Oligocene/Miocene submarine channel system: Insights from new age constraints and sediment volumes from the Austrian Northern Alpine Foreland Basin

Julian Hülscher, Gero Fischer, Patrick Grunert, Gerald Auer, Anne Bernhardt

Published in Frontiers in Earth Science 7 (2019): 302.
DOI: 10.3389/feart.2019.00302

Chapter 2 focuses on the Oligocene to early Miocene stratigraphy of the Upper Austrian Northern Alpine Foreland Basin and the information about hinterland processes that can be gained from sediment architecture and accumulation rates in the basin.
Julian Hülscher organized the sampling campaign, undertook the seismic interpretation and volume calculation, interpreted the results, and created most of the figures. Gero Fischer draw the remaining figures and conducted the foraminiferal analyses under the supervision of Patrick Grunert. Gerald Auer carried out the calcareous nannoplankton analyses. The manuscript was written by Julian Hülscher with major contributions from Anne Bernhardt, Gero Fischer, Patrick Grunert and Gerald Auer. Lukas Karal prepared rock powder for bulk-rock analyses, which were conducted by Claudia Puschenjak (University of Graz) and Prof. Joachimski (GeoZentrum Nordbayern, University of Nürnberg-Erlangen). Anne Bernhardt developed the project idea.

Chapter 3: Detrital apatite geochemistry and thermochronology from the Oligocene/Miocene Alpine foreland record the early exhumation of the Tauern Window

Julian Hülscher, Edward R. Sobel, Vincent Verwater, Philip Groß, David Chew, Anne Bernhardt

Published in Basin Research, 33, 3021– 3044.
DOI: 10.1111/bre.12593

This part of the thesis is a provenance and low-temperature thermochronology study of sand-sized sediments in the Upper Austrian Molasse Basin. Apatite single-grain U-Pb dating and trace-element analyses were combined with fission track dating of the same apatites to gain insights about the source and the exhumation history of the Oligocene/Miocene foreland sediments.
Julian Hülscher took the drill core samples and connected them with the 3D seismic reflection dataset and updated basin stratigraphy from Chapter 2. He conducted the fission track analysis under the supervision of Edward R. Sobel. Sample preparation was done by Edward R. Sobel and Julian Hülscher. David Chew and Julian Hülscher analyzed the apatites for their trace-element geochemistry and U-Pb isotopic composition. The datasets were merged and interpreted by Julian Hülscher who wrote the manuscript with Vincent Verwater and Philip Groß. It benefited greatly from the suggestions made by Anne Bernhardt, Edward R. Sobel and David Chew. Anne Bernhardt, Edward R. Sobel, and Julian Hülscher developed the project idea.

Chapter 4: Early bird apatites overhaul clays in provenance-change recording by 4-5 m.y.

Julian Hülscher, Edward R. Sobel, Niklas Kallnik, J. Elis Hoffmann, Ian L. Millar, Kai Hartmann, Anne Bernhardt

To be submitted to Geology

The fourth chapter focuses on the questions if and how changes in sedimentary provenance are recorded in different grain-size fractions. Therefore, the previously analyzed apatites from Chapter 3, were analyzed for their Sm-Nd isotopic composition. These results were compared to newly acquired $^{143}Nd/^{144}Nd$ isotopic ratios of clay-sized bulk-rock samples from drill cutting of the Upper Austrian Northern Alpine Foreland Basin.
Julian Hülscher sampled the drill cores and well cuttings and prepared together with Edward R. Sobel the apatite samples. Niklas Kallnik prepared the well cutting samples and conducted

the chemical Nd separation under the supervision of J. Elis Hoffmann. Ian L. Millar analyzed the apatites for their Sm-Nd isotopic composition. Kai Hartmann conducted the Monte-Carlo simulation of the clay-sized bulk-rock Nd isotopic results. Julian Hülscher wrote the manuscript which benefited greatly from the suggestions of all co-authors. Andreas Stracke analyzed the Nd isotopic composition of the clay-sized samples at the Westfälische Wilhelms-Universität, Münster. Anne Bernhardt, Edward R. Sobel, and Julian Hülscher developed the project idea.

Chapter 5: Conclusions

This chapter returns to the posed research questions from the first chapter and highlights the main conclusions that can be drawn from the presented work.

Chapter 6: Outlook

In this chapter, the outcome of the thesis is used to point towards potential future research opportunities.

Table of contents

List of Figures

List of Tables

Chapter 1: Introduction

The infill of sedimentary basins is our main source of information to reconstruct the tectonic and/or climatic evolution of the Earth's surface. By analyzing these archives, we gain information about the conditions under which the sediments were produced in the source area and transported into the sedimentary sink. Changes in sediment flux, architecture, geochemistry, and/or petrography, so-called 'environmental signals' (Tofelde et al., 2021), in a sedimentary archive can be interpreted to argue for or against changes in the hinterland (Clift et al., 2008; Füchtbauer, 1964; Govin et al., 2020; Gulick et al., 2015; Hu et al., 2012; Huber et al., 2018; Schlunegger and Castelltort, 2016). However, this information transfer from the source to the sink (Fig. 1.1) is only possible if the different compartments of the system, are acting together and transport the information unchanged from one endmember to the other (Allen, 2008), an assumption which is often oversimplified (Tofelde et al., 2021).

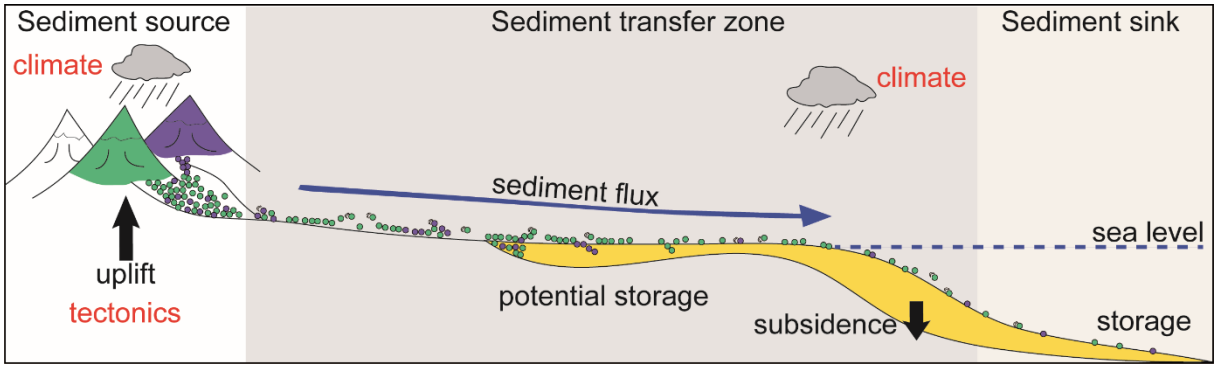

Figure 1.1: Conceptional idea of a sediment-routing system with the different compartments. The differently colored grains represent different sources. Modified after Romans et al. (2016).

Environmental signals from the source area may need several thousand or even several hundred thousand years to travel into the depositional zone (Castelltort and Van Den Driessche, 2003; Clift and Giosan, 2014; Duller et al., 2019) and can be destroyed (Jerolmack and Paola, 2010), buffered (Clift and Giosan, 2014), diluted (Wittmann et al., 2016) or amplified (Simpson and Castelltort, 2012) on their way downstream (Fig. 1.1).

The conceptual idea that the interplay between climate and tectonics is expressed in a sediment-routing system (SRS) is relatively new (Allen, 2008). This new aspect has triggered a boom in environmental-signal-propagation-research in the last decade and a cascade of review articles has been published recently (Caracciolo, 2020; Romans et al., 2016; Straub et al., 2020; Tofelde et al., 2021). However, the linkage between sediment source and sink on geological timescales is still poorly understood (Romans et al., 2016), partly because an attempt to correlate changes in the sediment sink with changes in the source necessarily

involves information about sea-level and sediment-routing changes (Carvajal and Steel, 2011). This information can be hard to gain in geological deep-time (> 10 Ma) and introduces large uncertainties onto interpretations.

This thesis aims to bridge this gap of knowledge. It focuses on the environmental signal propagation in response to tectonically induced exhumation events in the Oligocene to Miocene European Alps (Fig. 1.2). The following main research questions are addressed in the course of this thesis:

- Can the expected environmental signals caused by tectonic perturbations be found in the deep-marine sediment archive? If so, how long do they take to reach the sink?
- How is the sedimentary response to the environmental perturbation (*sensu* Tofelde et al. (2021)) imaged by different sedimentary proxies?
- Are there different progradation times for different grain-size fractions (sand-size vs. clay-size)?

To answer these questions in geological deep-time, the European Alps were chosen as research area because the orogen is one of the most extensively studied orogens in the world and phases of exhumation and their tectonic drivers are relatively well understood (Favaro et al., 2015; Handy et al., 2010; Handy et al., 2015; Schlunegger and Castelltort, 2016; Schmid et al., 2004). Three main tectonic/erosional events are investigated in this thesis as initiators of environmental signals: the exhumation of the Lepontine Dome in the Central Alps starting at ~32 Ma (Schlunegger and Castelltort, 2016); the exhumation of the Tauern Window in the Eastern Alps starting at ~28 Ma (Favaro et al., 2015); and the redeposition of the Augenstein Formation into the Northern Alpine Foreland Basin (NAFB) starting at ~21 Ma (Frisch et al., 2001).

Just as the well-investigated Alpine source area, the NAFB (Fig. 1.2) is one of the most thoroughly studied foreland-basin systems worldwide (Berger et al., 2005b; De Ruig and Hubbard, 2006; Garefalakis and Schlunegger, 2019; Gross et al., 2018; Hubbard et al., 2009; Kuhlemann and Kempf, 2002; Schlunegger et al., 1997) and important variables such as sea-level fluctuation (Zweigel, 1998) or sediment-routing pathways (Brügel et al., 2000, 2003; Füchtbauer, 1964; Ortner and Stingl, 2001; Platt and Keller, 1992) have already been comprehensively investigated. The present study is located in the eastern part of the NAFB in Upper Austria. Here, deep-marine environmental conditions persisted from the Oligocene to early Miocene (Rögl et al., 1979), in contrast to the Swiss and German part of the basin where continental sedimentation prevailed during that time (Platt and Keller, 1992). Depositional processes in the Upper Austrian NAFB were controlled from ~27 Ma until 19 Ma by a 3-6 km wide gravity-flow dominated channel system that transported sediment from west to east along

the basin axis for > 100 km (Bernhardt et al., 2012; De Ruig and Hubbard, 2006; Hubbard et al., 2009). As the SRS approach requires information about sediment provenance, architecture, transport, and deposition and resulting stratigraphy, comprehensive datasets containing such information were collected in the course of this study. The Oligocene to early Miocene succession of the Upper Austrian NAFB is nowadays buried beneath younger sediments. Therefore, the study is based on drill-core and well-cutting samples and on the interpretation of a large-scale 3D seismic-reflection dataset (6000 km^2, >5 km depth, Fig. 1.2). The samples and the 3D seismic dataset were provided by the company RAG Austria.

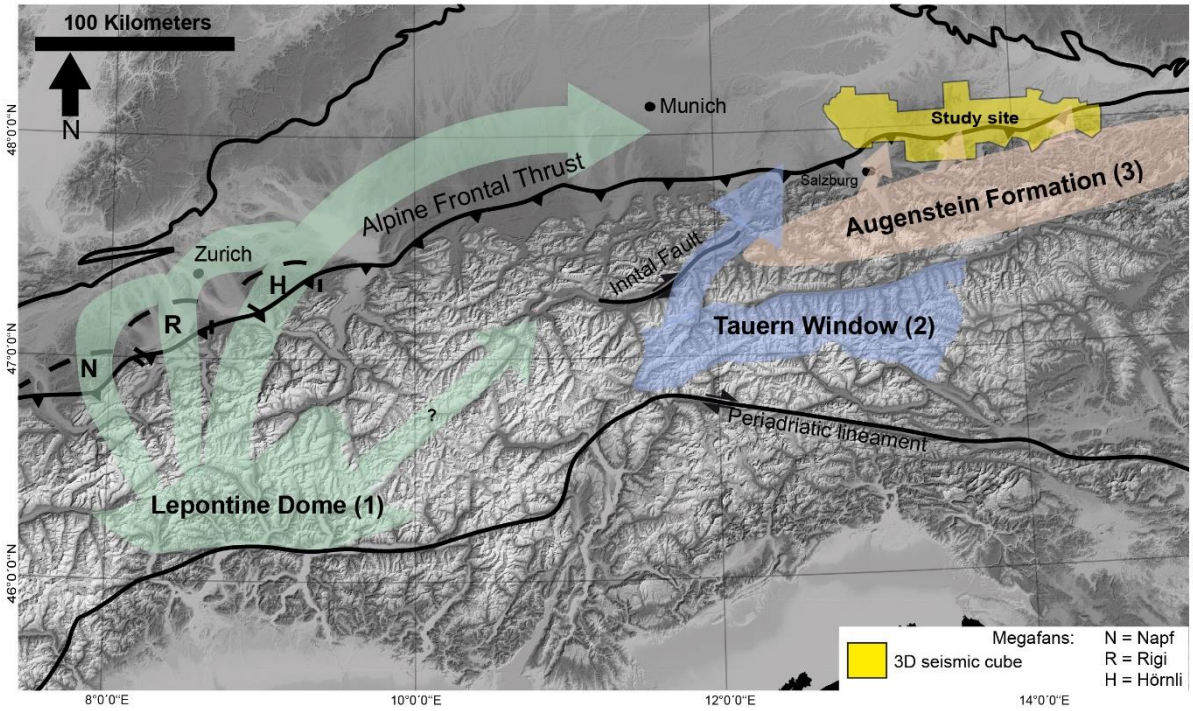

Figure 1.2: Map of the European Alps with the location of the three tectonically-induced exhumation events as initiators of environmental signals and the study site investigated in this thesis. (1) Exhumation of the Lepontine Dome in the Central Alps, (2) Exhumation of the Tauern Window in the Eastern Alps, and (3) exhumation and redeposition of the Augenstein Formation.

The results presented in this thesis have major implications for our understanding of the NAFB and the Alps and their evolution in Oligocene/Miocene times. Apart from the conceptual questions on the SRS approach, this thesis therefore will, also tackle the following research questions:

- What are the ages and durations of the Oligocene/early Miocene formations and unconformities in the Upper Austrian NAFB?
- What processes controlled the basin evolution in the Upper Austrian NAFB?
- How is the Late Oligocene exhumation period of the Tauern Window from ~28 Ma onward (Favaro et al., 2015) mirrored in the foreland sediments? How much material

was removed by erosional denudation from the Austroalpine nappes above the future Tauern Window before the beginning of lateral-escape tectonics at 23-21 Ma?

The results needed to answer these questions were gained by the combination of several different methods:

- A stratigraphic analysis based on the analysis and interpretation of the benthic foraminiferal assemblage and bulk-rock geochemistry (total organic carbon, S, $CaCO_3$) of well-cuttings from three wells in the basin was conducted to identify lithostratigraphic boundaries. Additionally, the samples were analyzed for their calcareous nannoplankton and stable carbon isotopic composition ($\delta^{13}C_{carb}$) to further constrain the absolute depositional ages of the sediments.
- Information about sediment architecture and volume in the Upper Austrian NAFB was collected via an extensive mapping campaign in the 3D seismic-reflection dataset. In connection with the newly acquired depositional ages, sediment accumulation rates were calculated.
- The exhumation history of the Alpine hinterland was constrained by apatite fission track (AFT) analysis of apatites separated from drill core samples. The results were connected with the newly acquired depositional ages to calculate AFT lag times.
- The sources of the sediments in the Upper Austrian NAFB were determined for two different grain-size fractions individually. The same sand-sized apatite grains that were previously dated via AFT were analyzed for their U-Pb and Sm-Nd isotopic composition as well as for their trace-element geochemistry. Additionally, 30 well-cutting samples were analyzed for their $^{143}Nd/^{144}Nd$ isotopic composition of the clay-sized bulk-rock sediment.

Due to this comprehensive approach that links geochemical, thermochronological and isotopic information of single grains and bulk-rock samples with bio- and chemostratigraphic information and seismic interpretation, this thesis relates information from the foreland to processes in the hinterland. Combined with information from the comprehensive published literature, this enables the quantification of total signal lag times (*sensu* Tofelde et al. (2021)) for different methods and grain-size fractions. With these – for geological deep-time – unique constrains, new insights are gained into the raised questions about signal propagation and delay that will ultimately help to improve our understanding of SRSs and their interaction with external perturbations.

This thesis is based on the research project “Towards the inversion of tectonic signals from deep-marine archives: Competing tectonic signal propagation from across the Alps into the marine sink” which has been initiated by Anne Bernhardt (Freie Universität Berlin) and Edward

R. Sobel (University of Potsdam). The project was funded by the Deutsche Forschungsgemeinschaft (Grants: BE 5070/ 7-1 and SO 436/ 16-1). Even though it was officially not part of the priority program SPP2017 “Mountain Building in Four Dimensions (MB-4D)”, this thesis benefited from a strong collaboration with researchers which are part of the MB-4D and the European AlpArray Working Group.

Chapter 2: Selective recording of tectonic forcings in an Oligocene/ Miocene submarine channel system: Insights from new age constraints and sediment volumes from the Austrian Northern Alpine Foreland Basin

This chapter has been published as:
Hülscher J., Fischer G., Grunert P., Auer G. and Bernhardt A. (2019). Selective Recording of Tectonic Forcings in an Oligocene/Miocene Submarine Channel System: Insights From New Age Constraints and Sediment Volumes From the Austrian Northern Alpine Foreland Basin. In: Frontiers in Earth Science. 7:302. DOI: 10.3389/feart.2019.00302

Abstract

Detailed characterization of variations in sediment architecture, flux, and transport processes in peri-orogenic basins offers insights into external climatic or tectonic forcings. We tested how four well-known tectonic/erosional events in the Oligocene/Miocene Alpine source area are recorded in the sediment-accumulation rates (SARs) of the deep-marine sink in the Northern Alpine Foreland Basin (NAFB): exhumation of the Lepontine Dome (starting at 30 Ma) and the Tauern Window (23-21 Ma), erosion of the Augenstein Formation (~21 Ma), and the visco-elastic relaxation of the European Plate. The Upper Austrian NAFB offers a unique opportunity to investigate external forcings on sedimentary infill due to the large amount of data on the Alpine hinterland and foreland. Deep-marine sedimentation, forming the Puchkirchen Group and the basal Hall Formation, was controlled by a basin-axial submarine channel (3–5 km wide, >100 km length). Two basin-wide unconformities were recognized in seismic-reflection data: the Northern Slope Unconformity (NSU) and the Base Hall Unconformity (BHU). We combine biostratigraphic and chemostratigraphic analyses of 316 drill-cutting samples from three wells with a large 3D-seismic-reflection dataset (3300 km^2, >5 km depth) to determine age and duration of the unconformities and to calculate spatially averaged SARs for the submarine channel and its overbanks, separately. Deepening of the basin, recorded by the NSU, occurred between 28.1 and 26.9 Ma. The Puchkirchen Group (26.9–19.6 Ma) is characterized by constant SARs (within standard deviation) in the channel [432–623 (t/m^2/Ma)] and on the overbanks [240–340 (t/m^2/Ma)]. The visco-elastic relaxation of the European Plate results in low SARs on the overbanks [186 (t/m^2/Ma)], a decrease in sediment grain size in channel deposits and a decrease in sea level at the BHU (19.6–19.0 Ma). In the upper Hall Formation (19.0–18.1 Ma), clinoforms prograding from the south filled up the basin [1497 (t/m^2/Ma)] within 1 Myrs. We conclude that only two of the tectonic signals are recorded in this part of the deep-marine sink, erosion of Augenstein Formation and visco-elastic relaxation of the European Plate; the exhumation of the Tauern Window and Lepontine Dome remain unrecorded.

2.1 Introduction

Sediment production, paleotopography, sediment-routing and transport processes control the temporal and spatial infill of peri-orogenic basins. The identification of the dominating control

processes offers insights into the underlying external environmental forcing mechanisms such as climatic transitions or deep-seated tectonic processes (Clift, 2006; Guillocheau et al., 2012; Gulick et al., 2015). Calculation of spatially averaged sediment-accumulation rates (SARs) allow to investigate these external environmental forcings and intrinsic controls within the sediment-routing system (Romans et al., 2016). Nevertheless, the correct interpretation of external environmental forcing from the sedimentary record remains challenging as its signal might be buffered (Clift and Giosan, 2014), shredded (Jerolmack and Paola, 2010), delayed (Schlunegger and Castelltort, 2016), or masked by autogenic processes (Murray et al., 2009). The attempt of correlating changes in the stratigraphic record to changes in external forcing necessarily involves an evaluation of preceding and contemporaneous tectonic events, sea-level changes, and changes in sediment-routing pathways, as all these internal factors shape the production and storage of sediments in all compartments of the source-to-sink system (Carvajal and Steel, 2011). Moreover, the precise evaluation of all depositional environments of the sedimentary system, both in space and in time, is crucial, as environmental signals may be recorded differently in different depositional environments within a single sedimentary system (e.g., Romans et al., 2016).

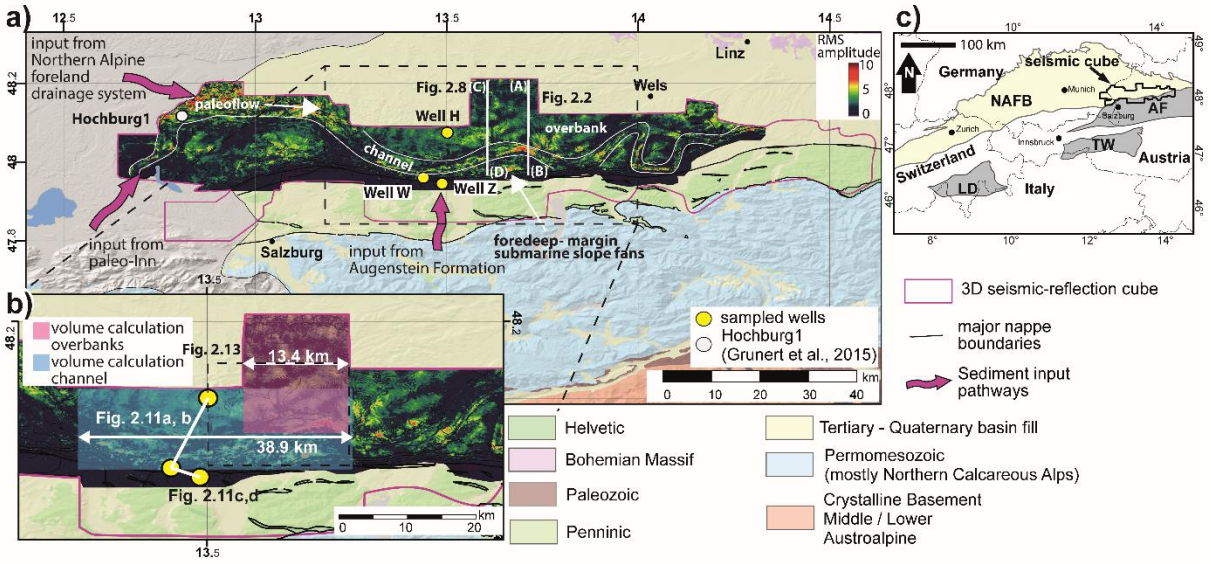

Figure 2.1 a): Simplified geological map of the Upper Austrian NAFB and position of the three analyzed wells and reference well Hochburg1 (Grunert et al., 2015). The pink outline shows the extent of the 3D-seismic cube provided by RAG. The inset shows a root mean square (RMS) amplitude map of the seismic-reflection surface of the Base Hall Unconformity outlining the axial channel, the extensive overbank deposits on the northern basin margin and the slope fans on the southern tectonically active margin. b) Detail of a) with location and extent of the volume calculation, the position of the three wells and the seismic cross sections between them. c) Present location of the NAFB, the Lepontine Dome (LD), Tauern Window (TW), and 3D-seismic cube in Central Europe. Additionally, the approximated position of the nowadays mostly eroded Augenstein Formation (AF) is marked.

The Upper Austrian Northern Alpine Foreland Basin (NAFB, Fig. 2.1) offers an excellent opportunity to investigate such signals. The sediment-source area, the European Alps, form one of the most extensively studied orogens in the world with well-constrained phases of uplift and denudation, and relatively well understood tectonic drivers (e.g. Handy et al., 2015). Similarly, the Upper Austrian NAFB is one of the most thoroughly studied foreland-basin systems (Gross et al., 2018). During the deposition of the Oligocene to Miocene Zupfing Formation, Puchkirchen Group – consisting of the Lower (LPF) and Upper Puchkirchen (UPF) Formations – and the lower Hall Formation, sediment routing in the basin was largely controlled by a submarine channel system along the basin axis (Figs. 2.2, 2.3) (De Ruig and Hubbard, 2006; Hubbard et al., 2009). This channel system received detritus (Fig. 2.4) from the Central and Eastern Alps (Sharman et al., 2018) and separated the basin into a wide, gently sloping northern (De Ruig and Hubbard, 2006) and a steep tectonically active southern margin (Covault et al., 2009). The deep-marine conditions of the Upper Austrian NAFB are in contrast to the fluvial, continental depositional environment in Oligocene/Miocene (Lower Freshwater Molasse, Fig. 2.3) times in the central and western part of the NAFB (Kuhlemann and Kempf, 2002). Due to its economic importance as a hydrocarbon province (Boote et al., 2018), the basin is densely covered by exploration and production wells and by a large, 3D seismic-reflection dataset covering 3300 km^2 and >5 km in depth (Fig. 2.1). The post-stack, 3D time-migrated seismic-reflection data cube and the well data are provided by the RAG Austria AG (Vienna).

To relate changes in sediment fill to external or internal forcings, well-constrained stratigraphic control is essential. A long history of stratigraphic work in the Upper Austrian NAFB indicate Chattian to earliest Aquitanian age for the Lower and Upper Puchkirchen formations and a Burdigalian age for the Hall Formation (Küpper and Steininger, 1975; Papp, 1975; Rögl et al., 1979). However, recent publications suggest a younger, late Chattian to Burdigalian age (24.5 to 19.5 - 18.9 Ma) for the Puchkirchen Group on the northern basin slope (Grunert et al., 2015; Grunert et al., 2013) in agreement with previous interpretations from surface outcrops of coeval lithostratigraphic units in Bavaria (Martini, 1981; Reiser, 1987; Wenger, 1987).

In this study, we re-evaluate and extend the stratigraphic concept introduced by Grunert et al. (2013, 2015) for the late Oligocene/early Miocene Upper Austrian NAFB by using benthic foraminifera and geochemistry (TOC, S, $CaCO_3$) for the identification of lithostratigraphic boundaries, calcareous nannoplankton and stable carbon isotopic composition ($\delta^{13}C_{carb}$) of bulk sediment for chronostratigraphic information. Drill cuttings from three wells were analyzed, one from the northern and two from the southern basin margin (Fig. 2.1, Well H, W, Z). The new age constraints are then used to calculate spatially averaged SARs ($t/m^2/Ma$) for discrete time intervals by using the 3D seismic-reflection cube and well data. We calculated sediment

volumes as this reduces the dependence on timescales <10^1 a (Sadler and Jerolmack, 2015) below the maximal resolution estimated to c. 100 ka based on the available bio- and chemostratigraphic constraints.

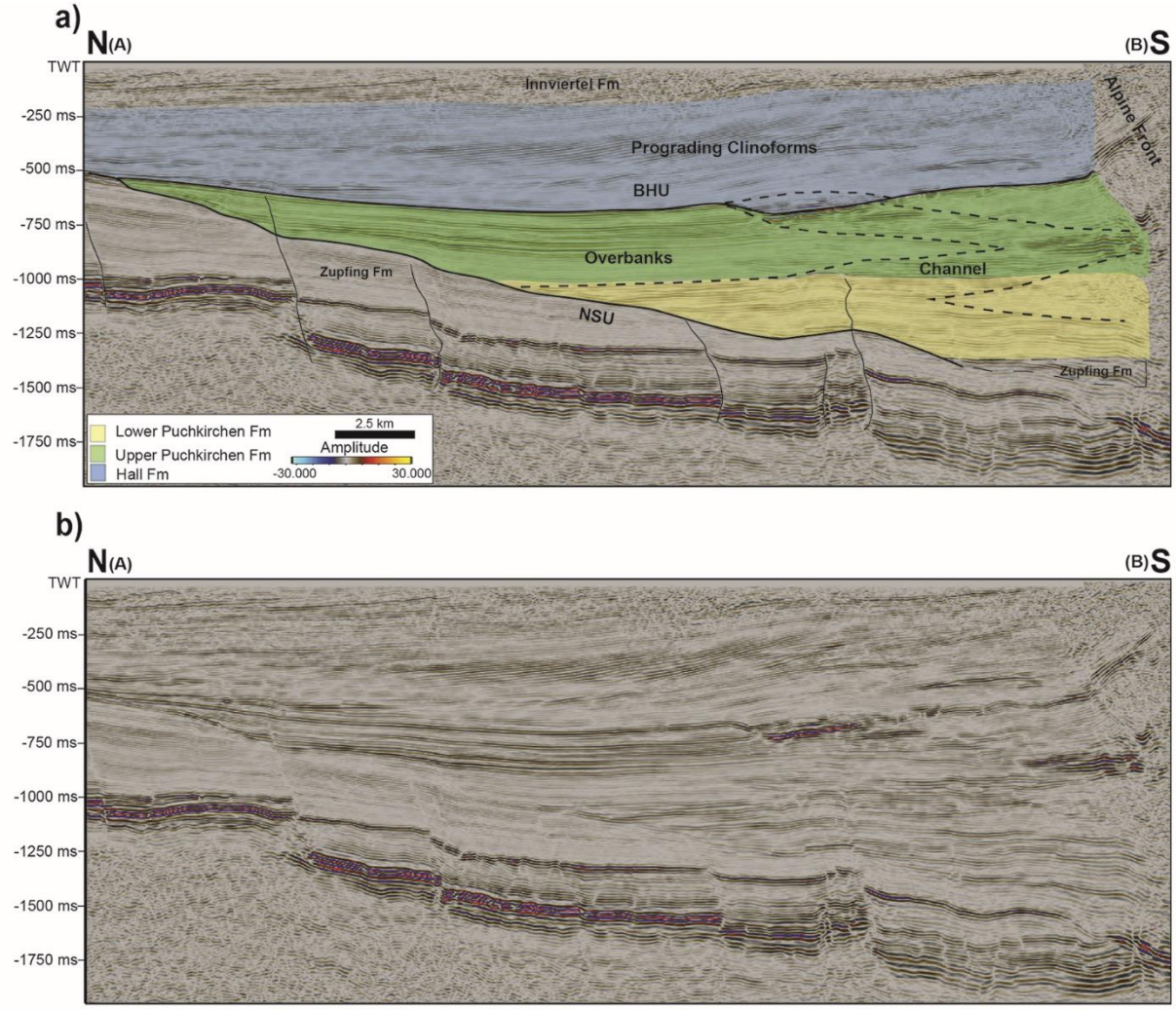

Figure 2.2: Cross section (N – S) through the Upper Austrian Molasse Basin (for position see Figure 2.1) showing the lateral migration of the main channel belt in the Puchkirchen and Hall formations (black, dotted lines). On the northern slope the NSU (thick black line) is visible with the Zupfing Formation below it. The wide (≤15 km) overbanks of the UPF and BHF north of the channel are illustrated. The BHU is characterized by truncated reflectors in the channel and two strong reflectors on the overbanks. Above the BHU a small segment with transparent reflectors is visible before clinoforms start to prograde from the southern margin into the basin. a) Interpreted seismic cross section; b) uninterpreted seismic cross section.

We hypothesize to detect the externally induced signals of four tectonic events in the Alps (for a detailed discussion of expected environmental signals see section 2.2.1): 1) the exhumation of the Lepontine Dome led to a doubling in SAR from 25 Ma onward; 2) the exhumation of the Tauern Window increased the SAR in early Miocene times; 3) a reduction of SAR due to uplift

in the foreland and decreasing elevation in the hinterland at the BHU; 4) the unroofing and erosion of the Augenstein Formation increase the SAR from 21 Ma onward. Our results shed new light on the development of the Upper Austrian NAFB during the Oligocene and Miocene and the forcings that controlled the sediment fill and the formation of two basin-wide unconformities in the basin.

2.2 Geological Overview and Stratigraphy

The NAFB is located on the northern border of the Alpine orogen in Central Europe (Fig. 2.1) and extends from Switzerland through Germany and into Austria for c. 1000 km in a west-east direction and up to 120 km in a north-south direction (Kuhlemann and Kempf, 2002). The development of the NAFB commenced in the upper Eocene due to flexure of the southern European continent. From 32-30 Ma to ~6 Ma, proximal, conglomeratic sediments (the Molasse) were deposited in the basin (Sissingh, 1998). The molasse sediments in the German and Swiss part of the basin are characterized by two shallowing-upward megacycles, which are further subdivided into the Lower Marine Molasse (32-28 Ma), the Lower Freshwater Molasse (28-20 Ma), the Upper Marine Molasse (20-16 Ma), and the Upper Freshwater Molasse (16-6 Ma) (Kuhlemann and Kempf, 2002).

The eastern part of the NAFB is located in Upper Austria (Fig. 2.1) and hosted a deep-marine environment (1000 – 1500 m water depth (Rögl et al., 1979)) in the Oligocene and early Miocene (Wagner, 1998). After a period of neritic environmental conditions in the Eggerding Formation (nannoplankton zone (NP) 23, Fig. 2.3) the basin rapidly deepened (Sachsenhofer et al., 2010; Soliman, 2012) and deep-marine (water depth ~1000 m) conditions are recorded in the overlying Zupfing Formation (ZFM) (Wagner, 1998). The ZFM contains the Rupelian/Chattian boundary (Fig. 2.3) and is located in NP 24 (Soliman, 2012; Wagner, 1998). The benthic index foraminifera of the ZFM are *Cancris bavaricus* and *Uvigerina moravia* (Cicha et al., 1998).

During deposition of the ZFM and the overlying LPF, UPF, and basal Hall Formation (BHF), the basin was characterized by a gently sloping northern margin and a steep, tectonically active southern margin (Figs. 2.1, 2.2, 2.3). Depositional processes in the basin were largely controlled by a 3-6 km wide, deep-marine, gravity-flow dominated channel system flowing parallel to the Alpine front from west to east for >100 km (De Ruig and Hubbard, 2006). The submarine channel system is characterized by intercalated sandstones (structured and structureless), conglomerates (clast-supported and matrix-supported) and silty marls which are interpreted as the deposits of turbidity currents (high to low density), debris flows, and hemipelagic suspension settling (De Ruig and Hubbard, 2006; Hubbard et al., 2009; Bernhardt

et al., 2012). To the north, the channel is flanked by wide overbank deposits (≤15 km, Fig. 2.2), which are formed by hemipelagic silty marls and subordinate turbiditic sandstones resulting from northward-directed overspill of sediment by gravity flows in the channel (Bernhardt et al., 2012; De Ruig and Hubbard, 2006; Hubbard et al., 2009; Masalimova et al., 2015). From the southern basin margin, submarine turbidite fans prograded northward into the basin (Covault et al., 2009) and large (≤ 30 km^3) mass-wasting events were shed into the channel (Kremer et al., 2018).

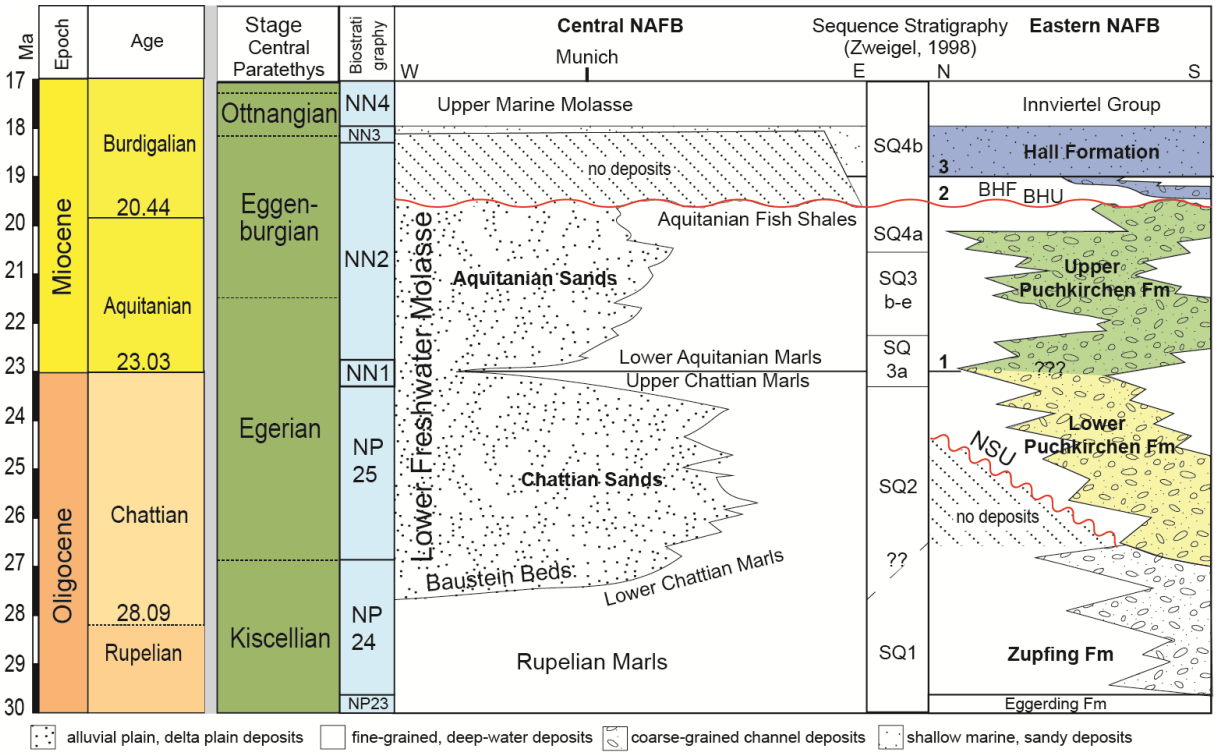

Figure 2.3: Schematic correlation of the global stages (Gradstein et al., 2012), the stages of the Central Paratethys (Piller et al., 2007), the calcareous nannoplankton after Backman et al. (2012) and Agnini et al. (2014), the stratigraphic and facies evolution (from W to E) in the central NAFB (Kuhlemann and Kempf, 2002), the sequence stratigraphy for the eastern NAFB (Zweigel, 1998), and the stratigraphy and facies evolution (N-S cross section) in the deep-marine Puchkirchen Trough. Depositional ages of the Eggerding and Zupfing Fm from Sachsenhofer et al. (2010) and Soliman (2012). Please note: Correlation between the eastern and the central NAFB is highly speculative. Only the Oligocene/Miocene (1) boundary (SQ 3a), the BHU (2), and the maximum flooding surface (mfs) in the HFM (3) can be used as reliable temporal markers.

The lower boundary of the LPF is defined by the occurrence of the agglutinated foraminifer *Psammosiphonella cylindrica* (formerly "*Rhabdammina linearis*"). The agglutinated species *Reticulophragmium acutidorsatum*, *R. rotundidorsatum* and *R. aff. amplectens* are typical. Of the calcareous foraminiferal species, *Uvigerina steyri* is common (Cicha et al., 1998). The lower boundary of the UPF is defined by the first occurrence of *Gaudryinopsis austriacus* (sometimes referred to as "*Bigenerina sp. 7*") and the disappearance of *Psammosiphonella*

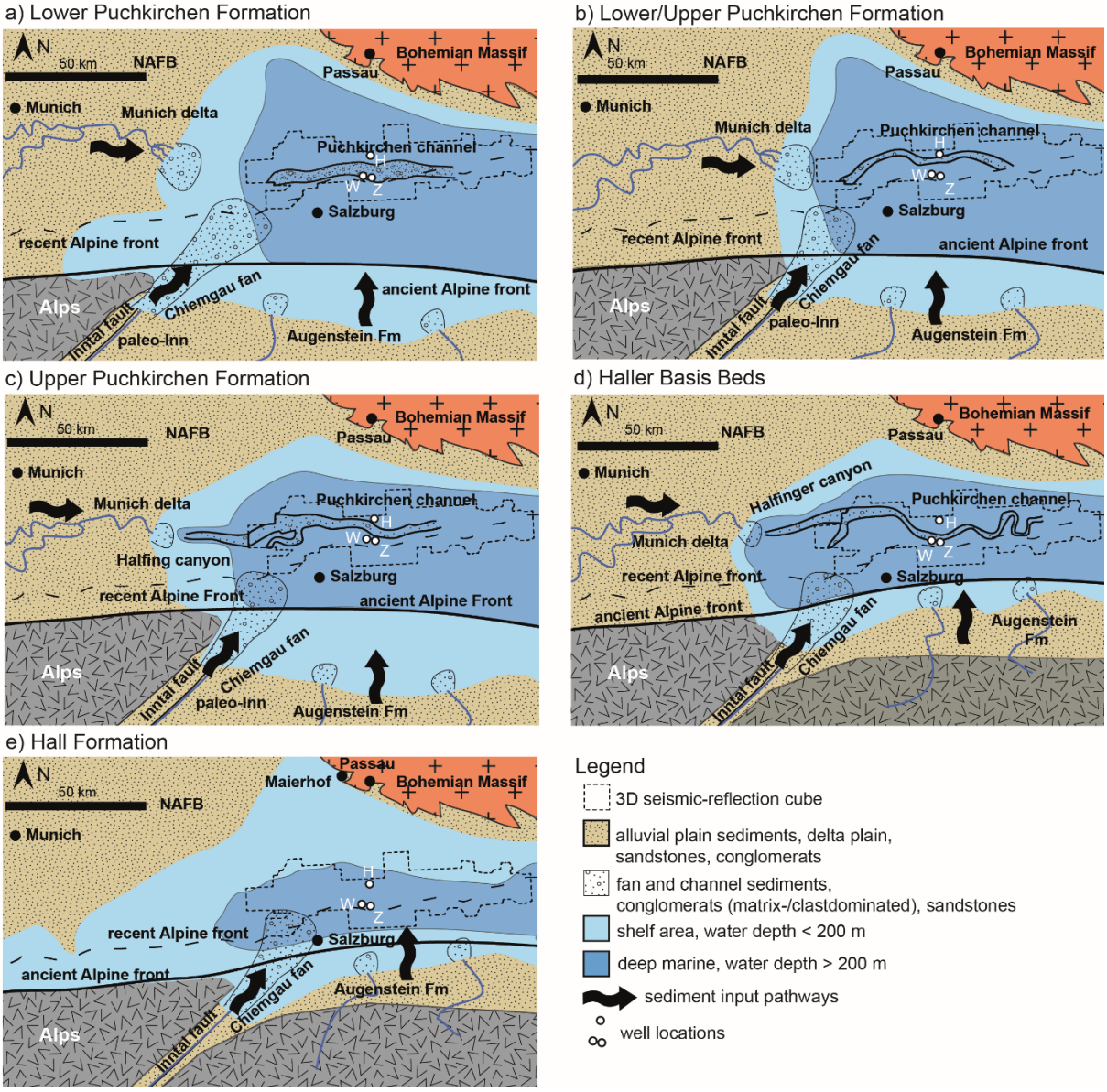

Figure 2.4: Paleogeographic reconstructions of the Upper Austrian and SE German NAFB during the late Oligocene through Early Miocene (a–e) and their main sediment input pathways. Channel geometries were mapped in the 3D seismic cube. Information compiled from Reiser (1987), Wenger (1987), Lemcke (1988), Zweigel (1998), Kuhlemann and Kempf (2002), and Grunert et al. (2013). During the deposition of the LPF (a) the channel shows a low sinuosity and is located at the southern basin margin. The Puchkirchen Trough was fed from the paleo-Inn, the Augenstein deposits, and the Munich delta from which clinoforms prograded into the basin, the shoreline moved to the east. At the L/UPF boundary (b) the shoreline reached its easternmost position; the channel started to meander and reached its northernmost position. In the UPF (c) the depositional system on the Bavarian Shelf changed, the Halfing canyon developed and was connected to the Puchkirchen channel. The shoreline was located further to the west compared to b). During the formation of the BHU (d) a major sea-level fall occurred and the channel acquired its highest sinuosity; the Halfinger canyon was still active. In the HFM (e) the sedimentation system in the Molasse Basin changed completely due to reestablishment of marine conditions in the western NAFB (Upper Marine Molasse), channel sedimentation ended and clinoforms started to prograde into the basin from the south.

Channel sedimentation terminated contemporaneously with a rise in sea level during the deposition of the BHF (Fig. 2.3), a deep-marine environment dominated by hemipelagic sediments (Fig. 2.2) was established in the Hall Formation (HFM) (Grunert et al., 2013; Zweigel, 1998). Clinoforms started to prograde from the southern margin during the middle HFM and filled the basin. The overlying mid-Burdigalian Innviertel Group was deposited in a tide-influenced shelf sea (< 200 m water depth) (Grunert et al., 2013; Grunert et al., 2012). The base of the Innviertel Group (Fig. 2.3) is marked by the first occurrence of *Amphicoryna ottnangensis* (Cicha et al., 1998).

Two large unconformities have been described in the basin, the Northern Slope Unconformity (NSU) and the Base Hall Unconformity (BHU, from bottom to top, Fig. 2.2) (De Ruig and Hubbard, 2006; Masalimova et al., 2015). The NSU is located on the northern basin slope and is present for at least 20 km in N-S direction and 100 km in W-E direction throughout the entire 3D seismic-reflection cube. Puchkirchen Group strata lap onto the unconformity. Masalimova et al. (2015) interpreted the unconformity as an over-steepened slope, characterized by sediment bypass. The age and duration of the NSU and the process that led to the oversteepening of the slope are currently unknown (Masalimova et al., 2015).

The BHU (Fig. 2.2) separates the UPF from the HFM and forms a basin-wide, deep-marine unconformity which was also described on the Bavarian Shelf to the east (De Ruig and Hubbard, 2006; Zweigel, 1998). In the 3D seismic-reflection data, the unconformity is characterized within the submarine channel system by truncated reflectors and on both margins by two high-impedance reflectors (Fig. 2.2). Zweigel (1998), Jin et al. (1995), and Wenger (1987) pointed to a sea-level fall at the UPF/HFM boundary (Fig. 2.4). Grunert et al. (2015) suggest an age of 19.5 – 18.9 Ma for the formation of the BHU. Additionally, Zweigel (1998) and Kuhlemann (2000) proposed a decrease in the subsidence and sedimentation rates at that time.

The so-called Puchkirchen Trough was fed by three different sources (Kuhlemann and Kempf, 2002). 1) A large, eastward prograding delta close to the present position of Munich received sediment from the Central Alps (Kuhlemann and Kempf, 2002; Sharman et al., 2018) (Fig. 2.4). 2) The paleo-Inn Fan fed by intra-Alpine material served as a second source for detritus to the Puchkirchen Trough (Kuhlemann and Kempf, 2002). 3) A series of rivers were running from the central Eastern Alps through the Augenstein deposits into the NAFB (Covault et al., 2009; Frisch et al., 2001). With the change of the paleo-drainage system at the beginning of the UMM, the NAFB was flooded (Fig. 2.4), the Puchkirchen Trough was cut off from the Central Alpine sediment supply (Grunert et al., 2013; Kuhlemann and Kempf, 2002).

2.2.1 Expected tectonic forcing

We hypothesize to detect the externally induced signals of four tectonic events in the results of the SARs calculation:

(1) The exhumation of the Lepontine Dome in the Central Alps (Fig. 2.1c) – starting ~32 Ma, accelerating at 25.5 Ma (Schlunegger and Castelltort, 2016) – has led to a two fold increase of SARs on the proximal megafans in the Swiss NAFB (250-450 m/Ma to 400-600 m/Ma, compacted rates) at 25.5 Ma (Schlunegger and Norton, 2015). Zweigel (1998) also reported an increase of SAR on the Bavarian Shelf (Fig. 2.4) from 25 Ma onward. We expect to see a similar two-fold increase in the SARs of the Upper Austrian NAFB.

(2) Between 23 and 21 Ma, the rapid exhumation of the Tauern Window (Fig. 2.1c) began in the Eastern Alps (Favaro et al., 2015; Scharf et al., 2013a). In the proximal Chiemgau Fan (Fig. 2.4), the Chattian deposits reach a (compacted) thickness of 1200-1500 m, whereas the Aquitanian contains 1250 m thick deposits (Ganss, 1977). SARs increase from 237-296 m/Ma in Chattian times to 483 m/Ma in Aquitanian times. Due to the short lag time (2-4 Ma) of apatite fission track ages in the Aquitanian deposits (deposition age: 22 Ma) (Kuhlemann et al., 2006), the increase in SARs is interpreted to be related to the exhumation of the Tauern Window. Therefore, we expect to find a similar ~65 – 100 % increase in our SAR in Aquitanian times.

(3) Zweigel (1998) explains her findings in the German NAFB (low SARs, angular unconformity, uplift in the northern part of the basin, sea-level decrease, reduction in deposited grain size) during the establishment of the BHU with the model of a visco-elastic relaxation of the European Plate. A visco-elastic behaving lithosphere loses strength with time depending on temperature, rheology, and initial stress of the lithospheric plate. Even without an additional load, the elevation in the hinterland can be reduced and the forebulge can migrate to the orogenic front (Beaumont, 1981), leading to a reduction in grain size and sediment flux from the hinterland, whereas the foreland is uplifted causing the angular unconformity and the decrease in sea level (Zweigel, 1998). An alternative explanation for Zweigel's (1998) findings might be the proposed slab-tearing event underneath the Eastern Alps at 20-25 Ma that may have led to a retreat and steepening of the European slab (Handy et al., 2015), causing a decrease in elevation in the orogen. The proposed slab-polarity switch underneath the Eastern Alps (Lippitsch et al., 2003) is still controversially discussed. However, the published literature does not conclude which of those models is more realistic. We hypothesize to find a reduction in SAR and redeposition of shelf strata.

(4) The unroofing and redeposition of the Augenstein Formation (Fig. 2.4) into the Puchkirchen Trough, caused by the beginning uplift of the underlying but sealed Northern Calcareous Alps, started ~ 21 Ma (Frisch et al., 2001). These fluvial sands and gravels with an estimated thickness of 1.8-2.2 km are today only persevered as relicts, hampering a precise evaluation

of the expected material that might have been relocated (Frisch et al., 2001). However, we expect to detect an increase in the SAR with the beginning of the unroofing and the redeposition of the Augenstein Formation into the Puchkirchen Trough.

2.3 Methods

Samples for bio- and chemostratigraphy were collected from three drill sites (sampling interval 10–40 m), one from the northern margin (Well H; Figs. 2.1, 2.5) and two from the southern margin of the basin (Well W and Well Z, Figs. 2.6, 2.7). In Well W, a ~800 m thick mass-wasting deposit shed from the south was excluded from sampling (Fig. 2.6). All named depth (m) are measured depth and not corrected for deflection of the wells.

2.3.1 Biostratigraphy

For the analysis of foraminiferal assemblages, the drill-cuttings (each representing about 2 m of sediment thickness) were wet-sieved (20 – 100 g per sample) under addition of diluted hydrogen peroxide (30%) through mesh-sizes of 250 µm, 125 µm and 63 µm. The fraction >250 µm was barren of foraminifera, all analyses were therefore conducted on the 125 to 250 µm size fraction. Taxonomic identification relied on the Atlas of Oligocene – Miocene foraminifera of the Central Paratethys (Cicha et al., 1998). For Well Z, already existing biostratigraphic constraints from a RAG internal report were used (Ćorić and Spezzaferri, 2009).

The preparation of smear slides followed the methodology of Bown (1998). Sediment was suspended in NH_3-buffered ultrapure milli-Q water and fully disaggregated by ultrasonic treatment. One drop of the suspension was placed on coverslips (24 x 30 mm) and slowly dried at a temperature of ~ 50° C. The slides were mounted using Norland No. 61® optical adhesive and investigated using an Olympus BX53 light microscope under parallel and crossed nicols at a 1000X magnification. Coccoliths were identified to species level if possible, following the taxonomic concepts of Bown (1998) and Galovic and Young (2012), supplemented by the Nannotax 3 website (Young et al., 2014) and the handbook of calcareous nannofossils (Aubry 1984, 1988, 1989, 1999, 2013). Calcareous nannoplankton zonation used in this study is based on the standard zonation of Martini (1971, recalibrated in Gradstein et al. (2012)) as well as the revised zonal scheme of Backman et al. (2012) and Agnini et al. (2014).

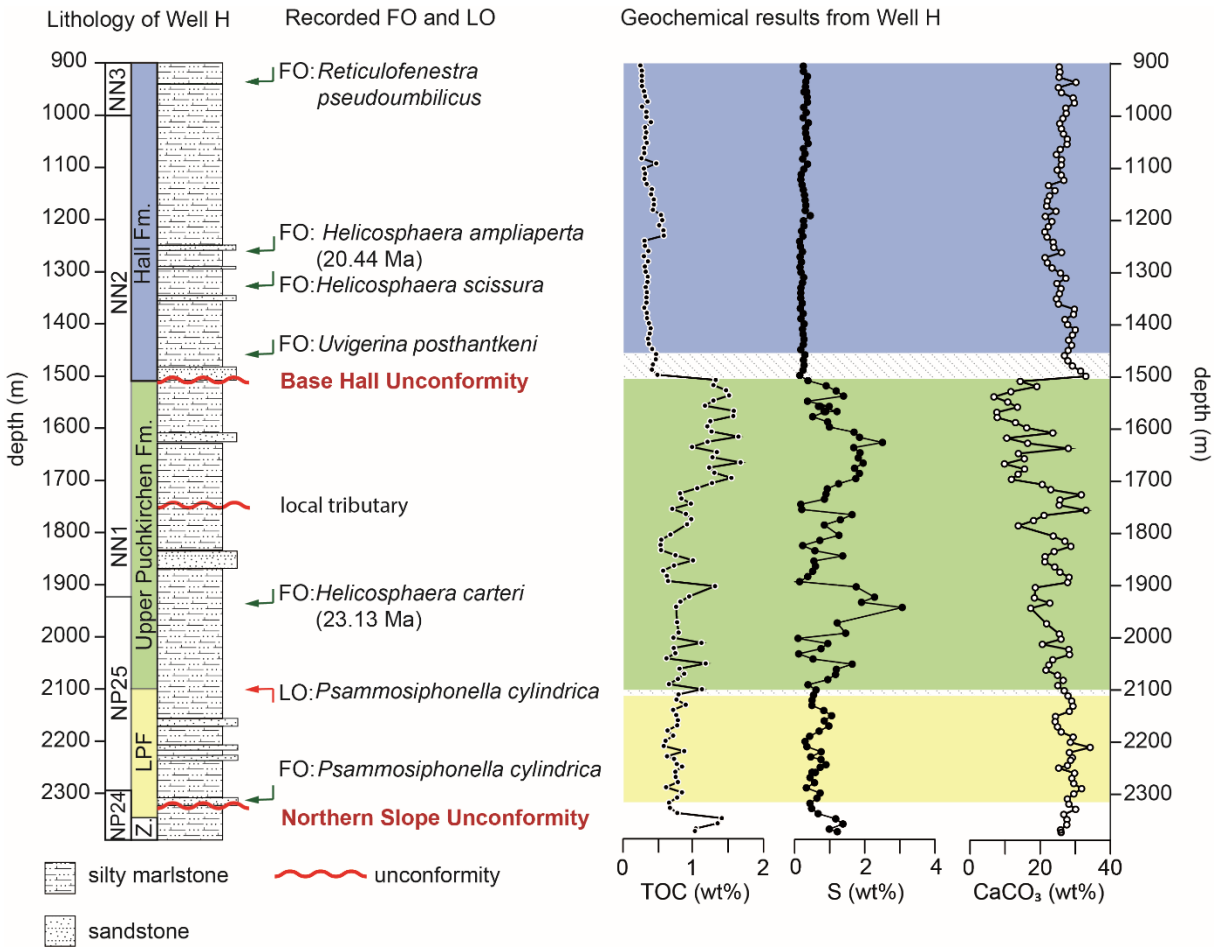

Figure 2.5: Simplified lithological section of Well H (see Fig. 2.1 for location) with first (FO) and last occurrence (LO) of index taxa (nannofossils and benthic foraminifera). Total organic carbon (TOC) and sulfur (S) increase from moderate levels with low variance in the LPF (from 2100 m) to very high levels in the upper half of the UPF showing greater variance, indicating highly unstable ecologic conditions. Above the BHU, TOC, and S values drop to very low and stable levels, while $CaCO_3$ dramatically increases. Uncertainties are due to sampling resolution and preservation. See text for discussion.

2.3.2 Chemostratigraphy

From Well H, W, and Z, 151, 103, and 71 samples, respectively, were chosen for analyses of stable carbon isotopes ($\delta^{13}C_{carb}$), total organic carbon content (TOC), sulfur content (S), and carbonate content. $\delta^{13}C_{carb}$ measurements were performed at the GeoZentrum Nordbayern, University of Nürnberg-Erlangen, using a Gasbench II connected to a ThermoFisher Delta V Plus mass spectrometer. Samples were dried, homogenized with a mortar and the carbonate powders reacted with 100 % phosphoric acid at 70°C. Values are reported in the conventional $\delta^{13}C_{carb}$ notation in ‰ relative to Vienna Pee Dee Belemnite standard (VPDB). Reproducibility and accuracy were monitored by replicate analysis of laboratory standards calibrated by

assigning $\delta^{13}C_{carb}$ values of +1.95 ‰ to NBS19 and -47.3 ‰ to IAEA-CO9. Reproducibility for $\delta^{13}C_{carb}$ was ±0.05 ‰.

The measurements for TOC, S and carbonate content were performed at the Institute for Earth Science, University of Graz, using a Leco CS-300 device. The dried, homogenized and mortared samples were analyzed for their total carbon (TC) and TOC content, total inorganic carbon (TIC) was calculated by subtracting TOC from TC. Carbonate content was calculated from TIC as calcite equivalent percentages ($CaCO_3$ = 8.34*TIC; Grunert et al., 2015).

2.3.3 Seismic interpretation and sediment-accumulation rates

Sediment-mass calculations were performed by using Petrel E&P software platform [(*) = Mark of Schlumberger], a cell-based modeling software, by integrating the 3D reflection-seismic data and density well logs. Two models were built (Fig. 2.1b), one including the channel-belt strata (in the following referred to as “channel model”) and one including the overbank deposits (“overbanks model”). The term geobody is used here to describe the separation of the models into different 3-dimensional segments for which masses were calculated (Fig. 2.8). The SARs are spatially averaged over large areas (variations between 31 km^2 to 255 km^2, Tab. 2.1) and long-time intervals (0.4 to 3.9 m.y.) and, hence, should be time-scale invariant according to Sadler and Jerolmack (2015). The local erosional processes which may influence small scale SAR calculations are averaged out with increasing temporal and spatially scale (Sadler and Jerolmack, 2015).

The seismic-reflection data have a dominant frequency of ~28 Hz and the average velocity in the area of interest is c. 3700 m/s, which results in a theoretical vertical resolution of ~33 m (De Ruig and Hubbard, 2006; Masalimova et al., 2015). The extent of the channel-belt strata and overbank deposits was mapped out based on 3-dimensional, time-migrated seismic reflectors. The models were built by using the ‘Structural Modeling’ toolbox in Petrel(*). The toolbox generates a grid, based on input data (geometry, upper, and lower boundary, cell size) with a certain number of cells. Cell size was established as 10 m*10 m*5.5 milliseconds. Mapped seismic-reflection horizons were merged into geobodies and were loaded via the Geometrical Modeling tool into the model (Fig. 2.8). This tool allows the user to generate properties for cells in the model. The model was converted into elevation depth (m) by using an in-house velocity model provided by RAG, which changed the individual z-axis of each cell (variation between 7 and 15 m).

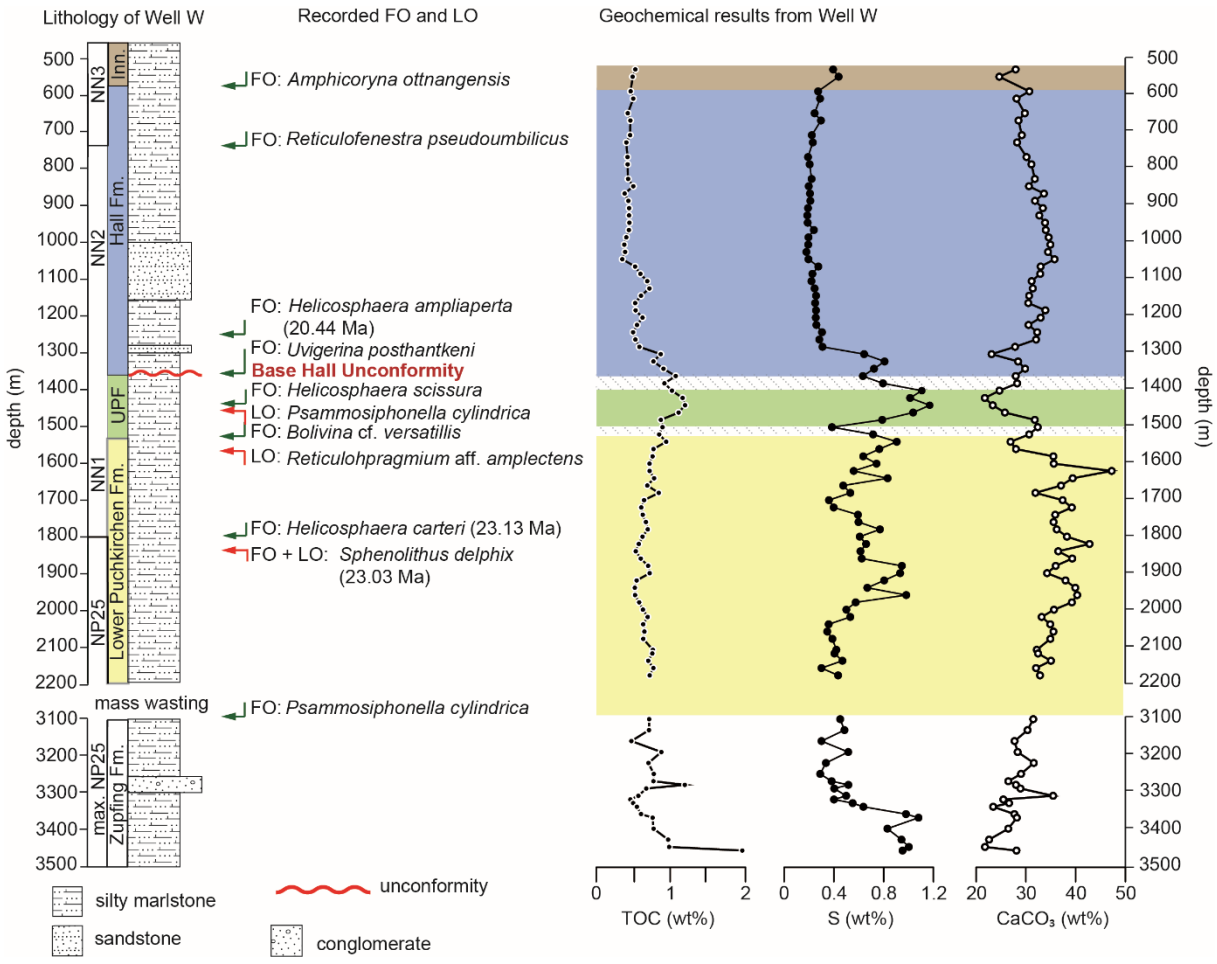

Figure 2.6: Simplified lithological section of Well W (for position see Fig. 2.1) with FO and LO of index taxa (nannofossils and benthic foraminifera), above 3200 m TOC- and S-values decrease compared to the underlying section and TOC-values show low variance, while S-values fluctuate heavily, until 1600m, the $CaCO_3$-content steadily rises. The UPF shows higher S and slightly higher TOC and greatly decreased $CaCO_3$-values. In the HFM, after 1300 m, TOC- and S-values drop to very low and stable levels, while $CaCO_3$ increases. Uncertainties are due to sampling resolution and preservation. See text for discussion.

Density (ρ ($\frac{kg}{m^3}$)) and lithology well data of 52 and 16 wells for the channel and overbank model, respectively, were downsampled into the depth-converted models. The downsampling for the lithological logs was accomplished by using the "most of" average method. Each model cell is assigned to a single lithology that is given by the most abundant lithology in the well section within the model cell, e.g. a 40% claystone and 60% sandstone cell will be assigned as a sandstone cell. Based on these modelled cells along the well paths, Petrel's (*) 'Facies Modeling' process assigns lithologies to the cells in between the individual wells using the horizontal and vertical trends in the data to guide the interpolation process.

The downsampling of the density data was performed by using the arithmetic mean of the well data for each individual cell intersected by a well. Data was then interpolated between the

individual wells of the model by using Petrel's (*) 'Petrophysical Modeling' tool. The interpolation of the density data between the wells is based on the results of the facies modeling, so that the modeled density data reflects the modeled trends from the lithological interpolation.

Masses are calculated by using $m\ (kg) = V\ (m^3) *\ \rho\ (\frac{kg}{m^3})$ for each individual cell and then summed up for an entire geobody. Calculations were run for three geobodies in the channel model and six geobodies within the overbank model (Tab. 2.1, Fig. 2.8). Geobody boundaries were selected based on good temporal control on base and top. For each geobody, a calculation with a minimum (-5%), average and maximum (+5%) ρ was run (Tab. 2.1). The mass of each geobody was calculated twice, first within the mapped boundaries and a second time by adding a 35 m segment on every boundary to account for erroneous seismic-reflection interpretation and the resolution of the seismic-reflection data. The calculated masses were divided by the base area (A (m^2)) of the geobody (Tab. 2.1) resulting in the areal density N ($\frac{kg}{m^2}$).

Calculated SARs (Q_S) are based on the presented bio- and chemostratigraphic results (tn, tm,…). For the geobodies in the channel model, the temporal information from the overbank geobodies was assumed (Tab. 2.1), except for the beginning of the LPF (see section 5.3). The calculated areal densities were divided by the time interval following $Q_S(kg/(m^2 * Ma)) = \frac{N}{t_n - t_m}$. The results represent the arithmetical mean rates and standard deviation (1σ; SD) from the six calculated rates of every geobody. Every geobody was calculated also in age brackets t ± 0.1 Ma based on the highest temporal resolution of our bio- and chemostratigraphic results. We note that this is an optimist boundary condition for temporal uncertainty quantification, however, the influence of spatial uncertainties on uncertainty dimensions exceeds the temporal ones (Tab. 2.1). To further constrain the sediment transport direction in the upper HFM clinoforms were mapped in the 3D seismic data (Fig. A1.1).

Table 2.1: Results from the channel and overbank model of the volume and SAR calculation.

Data Volume calculation	Area Size (km²)		Volume (km³)		Mass sediments (×10⁸ t)		Time markers from the bio-/chemostratigraphy		Depositional ages (Ma)		SAR (1σ SD) (t/m²/Ma)
	min	max	min	max	min	max	Beginning	End	Beginning	End	
Channel geobodies											
Lower Puckirchen Formation Geobody	169.8	478.3	131.0	160.5	3603.3	4960.9	Beginning NP25	Boundary L/UPF [2]	26.9	23.5	390 (±103)
Upper Puchkirchen Formation Geobody	102.4	293.5	160.0	226.8	3896.2	5888.9	Boundary L/UPF	BHU [5]	23.5	19.6	518 (±39)
Haller Basis Beds	177.8	181.4	19.3	35.6	456.6	876.7	BHU	MFS above BHU [6]	19.6	19	622 (±189)
Overbank geobodies											
Geobody 1	31.7	32.5	2.2	3.8	54.8	103.5	Peak 1 [1]	Boundary L/UPF [2]	24.5	23.5	243 (±65)
Geobody 2	140.0	140.8	13.0	20.2	320.6	547.3	Boundary L/UPF	FO *H. carteri* [3]	23.5	23.1	869 (±277)
Geobody 3	255.3	256.1	49.1	61.6	1190.7	1650.5	FO *H. carteri*	Peak 11 [4]	23.1	21.5	339 (±44)
Geobody 4	238.0	238.8	38.5	48.8	909.4	1273.6	Peak 11	BHU [5]	21.5	19.6	240 (±31)
Geobody 5	245.8	246.6	5.6	16.1	132.0	419.2	BHU	MFS above BHU [6]	19.6	19	185 (±94)
Geobody 6	202.4	203.2	103.2	113.0	2477.7	2952.6	MFS above BHU	Hall/Innviertel FM boundary [7]	19	18.1	1497 (±159)

Note that the maximal and minimal area size of the channel model vary greatly due to the different width of the channel through time (Hubbard et al., 2009). Depositional ages are gained from 1 = onset of sedimentation on the northern slope; 2 = $\delta^{13}C_{carb}$ -peak 4 (Well H); 3 = FO *Helicosphaera carteri* (Well H); 4 = $\delta^{13}C_{carb}$ -peak 11 (Well H); 5 = $\delta^{13}C_{carb}$ -peak 14 (Well H); 6 = mfs and Sr-Isotopy from Maierhof; 7 = Hall Fm./Innviertel Group boundary (Grunert et al., 2013)

2.4 Results

2.4.1 Foraminifera and calcareous nannoplankton

The abundance of benthic foraminifera is generally <50 specimen per sample and several barren intervals are present (see Tab. A1.1 for a complete list of species and Fig. A1.2 for representative specimens). Especially the index species are very rare and often poorly preserved. Calcareous nannoplankton abundance in the samples ranges from common to very rare, with index species often being very rare (see Tab. A1.2 and Fig. A1.3 for complete list and representative specimens). Their preservation ranges from good to poor. The scarcity and preservation state impose a challenge for taxonomic identification and biostratigraphic interpretation. We had to resort to secondary marker species, co-occurrences and the interpretation of the assemblage as a whole.

2.4.1.1 Well H

The FO and LO of *Psammosiphonella cylindrica* indicates the Lower Puchkirchen Formation between 2325 and 2100 m (Fig. 2.5). The fauna in the lower part of the LPF (2325–2190 m) consists of *Lenticulina sp*., *Praeglobobulimina sp*., *Virgulinella sp.*, *Psammosiphonella cylindrica*, *Heterolepa sp*., *Bathysiphon sp*., *Bulimina sp*., *Cibicides sp*. and *Asterigerinata sp*. Following a widespread absence of foraminifera for several tens of meters, *Praeglobobulimina sp.* re-appears as first species at 2150 m and soon dominates the assemblages, outnumbering the few *Bathysiphon sp.* and *Bolivina sp.* This is followed above by a second interval of widespread absence of foraminifera for 30 meters. In the UPF (from 2100 m), some *Bathysiphon* specimens were found while above 1960 m Bulimina sp. and *Lenticulina sp.* occur.

Above 1960 up to 1450 m benthic foraminifera are generally scarce (Tab. A1.1). Only between 1540 m to 1510 m depth, very few specimens of *Bulimina sp.*, *Lenticulina sp.* and *Cibicidoides sp.* occur. *Uvigerina posthantkeni* and some *Lenticulina* specimens were found just above this interval at 1455 m marking the base of the Hall Formation. All samples above 1455 m are barren of benthic foraminifera.

The FO of *Helicosphaera carteri* was found at 1920 m (Fig. 2.5). The FO of *Helicosphaera ampliaperta* at 1260 m, shows specimen already at full size (> 10 µm; Fig. A1.3). The FO of *R. pseudoumbilicus* >7µm is recorded at 910 m. Samples barren of nannofossils are recorded for 2165 m, intervals from 2110 to 2085 m, 1900 to 1800 m, and sample 1540 m (Tab. A1.2).

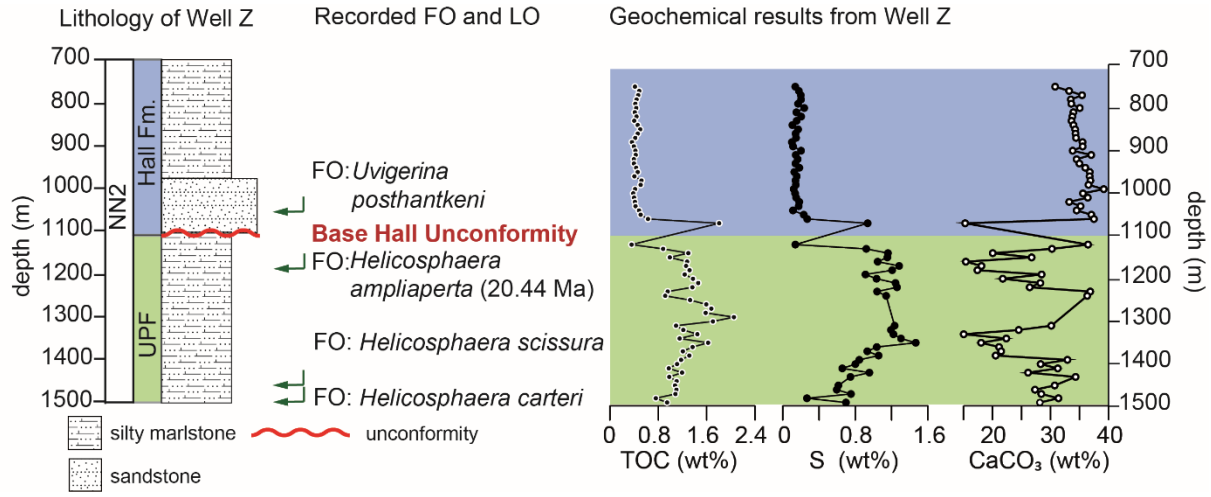

Figure 2.7: Simplified lithological section of Well Z (for position see Fig. 2.1) with FO and LO of index taxa [nannofossils and benthic foraminifera (Ćorić and Spezzaferri, 2009)], TOC- and S-values are high in the UPF and $CaCO_3$-content is highly variable (A1-horizon after Gross et al., 2018). At 1125 m TOC- and S-contents show a decrease, increase again and finally decrease to low and stable levels until the end of the section. See text for discussion.

2.4.1.2 Well W

The samples from 3470 to 3100 m are barren, with only a few, single specimens of no stratigraphic relevance (Fig. 2.6). The FO of *Psammosiphonella cylindrica* at 3100 m marks the beginning of the LPF. The LO of *Reticulophragmium aff. amplectens* (1560 m) and the FO of *Bolivina versatilis* (1520 m) indicate the boundary of the Upper and Lower Puchkirchen Formation between 1560 and 1520 m. The FOs of *Uvigerina posthantkeni* and *Fontbotia wuellerstorfi* (1360 m) mark the onset of the Hall Formation. The base of the Innviertel Group is marked by the FO of *Amphicoryna ottnangensis* at 580 m (Fig. 2.6).

From 3230 to 3100 m, *Bulimina sp.*, *Heterolepa sp.*, few *Praeglobobulimina sp.*, and *Valvulineria sp.* were found. *Valvulineria sp.* becomes increasingly rare above 2200 m and is replaced by *Praeglobobulimina sp.*, becoming very common especially from 2200 to 2152 m. In the same interval *Cibicides sp.* becomes a relevant constituent of the assemblage. From 1800 m upward, the samples are functionally barren up to 1600 m. With the onset of the Upper Puchkirchen Formation at 1520 m, a new faunal assemblage is established consisting of *Bolivina sp.*, *Lenticulina sp.*, *Heterolepa sp.*, *Bulimina sp.* and *Asterigerinata sp.* All samples from the 900 to 760 m interval and from 520 m to 420 m are barren (Tab. A1.1).

The FOs of the calcareous nannofossil taxa *Helicosphaera carteri* and *Sphenolithus delphix* occur at 1800 m (Fig. 2.6). The crossover in the dominance of *Helicosphaera euphratis* and *Helicosphaera carteri* was identified at 1400 m, shortly above the FO of *Helicosphaera scissura* at 1424 m. At 1260 m also the FO of already comparatively large (>10 µm) *Helicosphaera*

ampliaperta was recorded. *Reticulofenestra pseudoumbilicus* first occurs at 760 m. The interval of 1440 to 1520 m, 1220 to 1240 m, 820 to 1140 m and the sample from 400 m are devoid of nannofossils (Tab. A1.2).

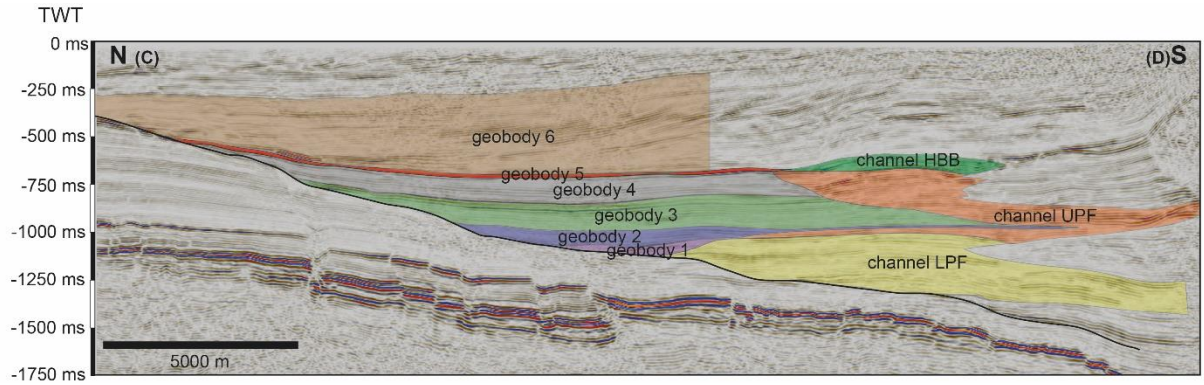

Figure 2.8: Cross section (N – S) through the Upper Austrian Molasse Basin (for position see Fig. 2.1) showing the extent of the geobodies in the channel and overbank model. Note the varying base area of the geobodies.

2.4.2 TOC, S, and Carbonate Content

2.4.2.1 Well H

In Well H (Tab. A1.3), the lowermost samples (2385 – 2360 m) show high TOC (Average (A) = 1.2 wt%, standard deviation (σ) = 0.2 wt%) and S (A = 1.2 wt%, σ = 0.1 wt%) values that rapidly decrease at 2350 m (A = 0.8 wt% TOC and 0.6 wt% S; Fig. 2.5). These TOC contents are stable with small variations until 2100 m (S σ = 0.2 wt%; TOC σ = 0.1 wt%). The $CaCO_3$ content remains stable from 2385 m until 2100 m with an average of 28 wt% (σ = 2 wt%). From 2100 m until 1510 m, $CaCO_3$ content shows higher variations (σ = 7 wt%, A = 20 wt%) and TOC (A = 1.0 wt%, σ = 0.3 wt%) and S (A = 1.1 wt%, σ = 0.6 wt%) contents are high compared to the underlying interval. Especially, from 1700 m until 1510 m, the S content and TOC (Fig. 2.5) are high (> 1wt%, σ < 0.5 wt%) and the $CaCO_3$ content decreases (< 20 wt%, σ = 6 wt%). At 1500 m, the TOC and S content both decrease and remain stable until the top of the section with low variations (TOC A = 0.4 wt%, σ = 0.1 wt%; S A = 0.3 wt%, σ = 0.1 wt%), whereas the $CaCO_3$ content increases to values around 25 wt% (σ = 3 wt%).

2.4.2.2 Well W

The variations of the LECO data in Well W (Tab. A1.3) are similar to the variations in Well H. The deepest samples (3460 – 3370 m) show high TOC (A = 1.1 wt%, σ = 0.4 wt%) and S contents (A = 1.0 wt%, σ = 0.8 wt%) but low carbonate contents (A = 25 wt%, σ = 3 wt%) (Fig. 2.6). From 3360 m upward until 1560 m, the TOC shows only minor variations (σ = 0.1 wt%) around an average content of 0.7 wt%. The S content (A = 0.6 wt%) is more variable (σ = 0.2 wt%) in this section and the $CaCO_3$ content is high compared to the underlying section (A = 35 wt%, σ = 4 wt%). From 1540 to 1380 m, the TOC (A = 1.0 wt%, σ = 0.1) and S (A = 0.9 wt%, σ = 0.3 wt%) values are increased, whereas the carbonate content is decreased (A = 27 wt%, σ = 4 wt%). At 1380 m, a decrease in the S content (from 1.1 to 0.3 wt%) and TOC (from 1.0 to 0.6 wt%) starts that lasts until 1280 m, in the same interval the $CaCO_3$ content increases (from 25 to 32 wt%; Fig. 2.6). After this decrease, TOC (A = 0.5 wt%, σ = 0.2 wt%), S (A = 0.3 wt%, σ = 0.2 wt%), and carbonate content (A = 31 wt%, σ = 3 wt%) show little variation until the top of the sampled section.

2.4.2.3 Well Z

In Well Z (Tab. A1.3) from 1495 m upward high TOC (A = 1.2 wt%, σ = 0.2 wt%) and S content (A = 1.0 wt%, σ = 0.3 wt%) with high standard deviations (Fig. 2.7) were found, accompanied by $CaCO_3$ contents of 26 wt% (σ = 6 wt%), At 1125 m the TOC and S values decrease and rapidly increase to >1wt% at 1075 m again, where the $CaCO_3$ is low again (15 wt%). From 1065 m until the top of the sampled interval (755 m), the TOC (A = 0.4 wt%, σ = 0.1 wt%) and S (A = 0.2 wt%, σ = 0.1 wt%) are low and show low standard deviations. In contrast, the carbonate content is high (A = 35 wt%, σ = 2 wt%) in this uppermost section.

2.4.3 $\delta^{13}C_{carb}$

Results for $\delta^{13}C_{carb}$ are shown in detail in Fig. 2.9 (Well H, Z) and Appendix 1 (Well W, Fig. A1.4, Tab. A1.3). $\delta^{13}C_{carb}$ from Well H varies between -2.03 and +1.34 ‰ with the lowest values at the lowest part of the sampled section (2385 – 2350 m). At 2290 m, the $\delta^{13}C_{carb}$ values show a first maximum (0.82 ‰). They then decrease to values around 0.23 ‰ from 2250 to 2020 m with distinct negative and positive peaks at 2120 m and 2070 m, respectively. From 2020 to 1840 m, the $\delta^{13}C_{carb}$ data show an increase to values around 1.00 ‰ (Fig. 2.9).

This plateau is present until 1740 m. At this depth, $\delta^{13}C_{carb}$ values show a decreasing trend until a minimum value of -1.27 ‰ at 1480 m. An interruption of this decreasing trend appears between 1610 and 1560 m with values up to 0.94 ‰. From 1480 to 1360 m, the $\delta^{13}C_{carb}$ values again increase to around 0.04 ‰ which then vary (σ= 0.19 ‰) around this value until the top of the section at 700 m. An outlier is present at 1090 m with a $\delta^{13}C_{carb}$ of -0.88 ‰.

Data from Well W $\delta^{13}C_{carb}$ show a large variability between -4.85 and 2.86 ‰. The section from 3640 to 3100 m is characterized by values around 0.50 to 1.00 ‰, except for the deepest sample, which shows a value of -4.85 ‰. From 2200 m to 1360 m, the values vary between 0.40 and 0.70 ‰. Exceptions are the intervals from 2020 to 1960 m (-0.10 to 0.22 ‰), from 1660 to 1620 m (1.06 to 2.68 ‰) and at 1500 m with a value of -0.51 ‰. Isotopic values from 1360 to 1260 m show a pronounced decrease from 0.77 to -0.56 ‰. Above 1260 m depth, the values show an increasing trend to 0.37 ‰ at 820 m. From 820 m to 400 m, $\delta^{13}C_{carb}$ data show only small variation (σ = 0.08 ‰) around 0.20 ‰ except for an outlier at 420 m depth with a value of -1.45 ‰.

Well Z shows $\delta^{13}C_{carb}$ values from -1.12 to 1.58 ‰ (Fig. 2.9). The lowest part of the sampled section shows a plateau with mean $\delta^{13}C_{carb}$ values around 0.69 ‰ and σ = 0.09 ‰, with two outliers at 1435 and 1395 m (Fig. 2.9). Isotopic values then decrease until 1295 m to -0.67 ‰ and vary until 1175 m around 0.14 ‰ (σ = 0.11 ‰). From 1175 m upward, the values decrease until they reach -1.12 ‰ at 1135 m. The values then increase slightly to -0.20 ‰ until 925 m, an outlier is located at 1075 m (-0.10 ‰). From 925 m until the top of the section at 755 m, the $\delta^{13}C_{carb}$ values show only small variations (σ = 0.01 ‰) around -0.36 ‰.

2.4.4 Sediment-accumulation rates and transport direction

In the channel model, SARs vary between 390 and 622 (t/m^2/Ma) (Fig. 2.10). In the LPF, the geobody (Fig. 2.10) shows a SAR 390 (± 103) (t/m^2/Ma). The UPF has a slightly increased SAR of 518 (± 39) (t/m^2/Ma) and in the BHF the rates reach a maximum of 622 (± 189) (t/m^2/Ma) (Tab. 2.1, Fig. 2.10). The SARs of all three geobodies in the channel model overlap within their 1σ SD.

SARs of the overbank model vary widely between 186 to 1497 (t/m^2/Ma) (Fig. 2.10). Geobody 1 (Fig. 2.8) shows a SAR of 243 (± 65) (t/m^2/Ma). In geobody 2, the SAR increases to 869 (± 277) (t/m^2/Ma), and geobody 3 shows a SAR of 340 (± 44) (t/m^2/Ma). In geobody 4, the SAR decreases to values of 240 (± 31) (t/m^2/Ma). This decrease in SAR is continued in geobody 5 with a rate of 186 (± 94) (t/m^2/Ma). Geobody 6 shows the highest SARs of both models of 1497 (± 159) (t/m^2/Ma) (Tab. 2.1, Figs. 2.8, 2.10).

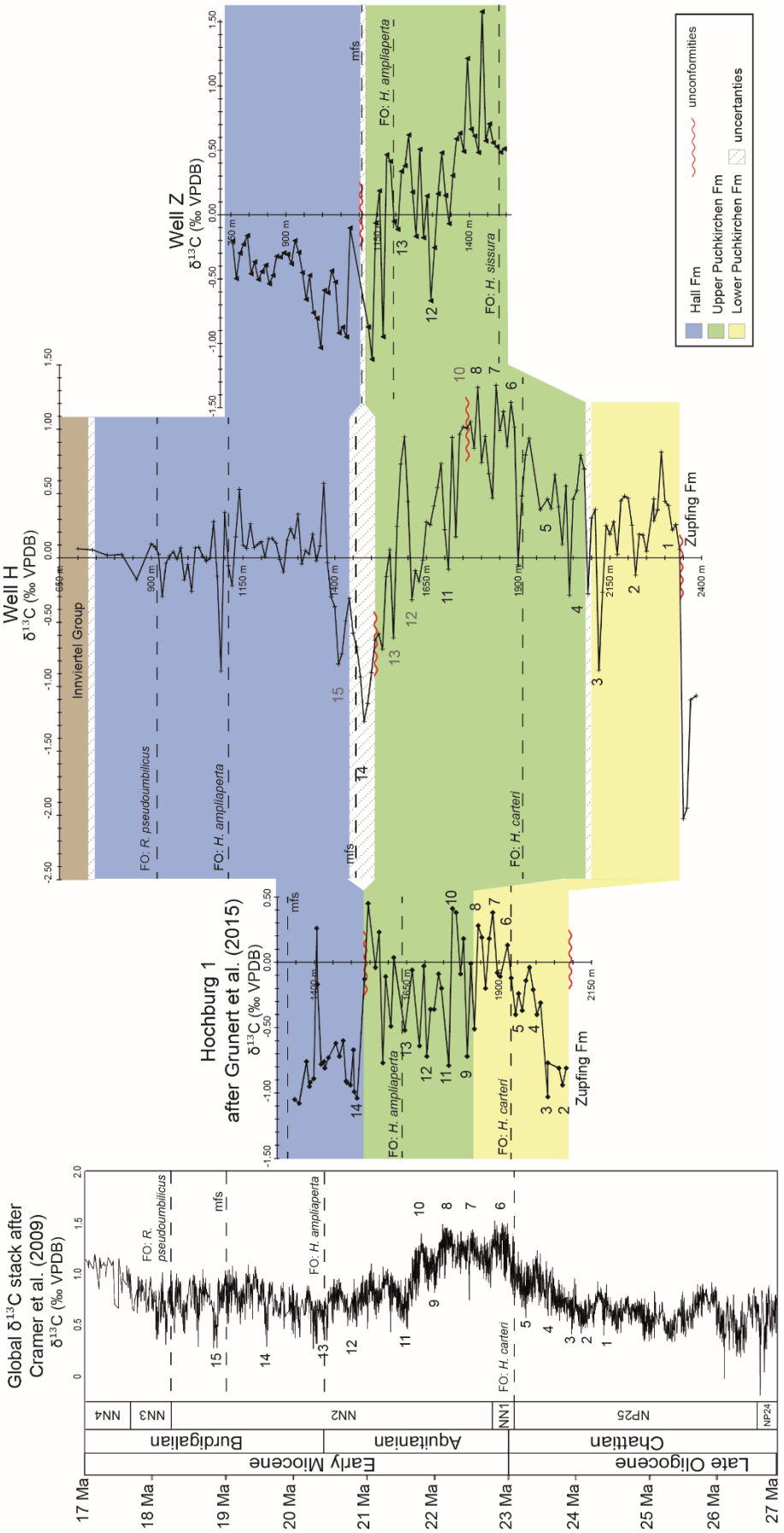
Well Z
δ13C (‰ VPDB)
Well H
δ13C (‰ VPDB)
Hochburg 1
after Grunert et al. (2015)
δ13C (‰ VPDB)
Global δ13C stack after
Cramer et al. (2009)
δ13C (‰ VPDB)
Innviertel Group
Hall Fm
Upper Puchkirchen Fm
Lower Puchkirchen Fm
unconformities
uncertainties
FO: R. pseudoumbilicus
FO: H. ampliaperta
FO: H. sissura
FO: H. carteri
mfs
Zupfing Fm
17 Ma
18 Ma
19 Ma
20 Ma
21 Ma
22 Ma
23 Ma
24 Ma
25 Ma
26 Ma
27 Ma
Early Miocene
Late Oligocene
Burdigalian
Aquitanian
Chattian
NN4
NN3
NN2
NN1
NP25
NP24

Figure 2.9 (previous page): Correlation of $\delta^{13}C_{carb}$ data from the Upper Austrian NAFB (Hochburg1, Well H and Z) and the global stack of Cramer et al. (2009). Numbers indicate minima and maxima in the global stack that are used for correlation. FO of *Helicosphaera ampliaperta*, *Helicosphaera carteri,* and *Reticulofenestra pseudoumbilicus* are shown. Maximum flooding surface (mfs) is taken from Grunert et al. (2013) in Hochburg1 and correlated by seismic interpretation to Well H and Z.

The rates of overbank geobodies 1, 3, and 4 illustrate the "background" SAR (243 ± 65 (t/m^2/Ma) from 24.5 to 23.5 Ma; 340 ± 44 (t/m^2/Ma) from 23.1 to 21.5 Ma; 240 ± 31 (t/m^2/Ma) from 21.5 to 19.6 Ma). The differences (increase of ~40% from geobody 1 to 3, decrease of ~30% from geobody 3 to 4) overlap in their 1σ standard deviation.

Due to insufficient age-control points, the channel model consists of a single geobody in the UPF. To enable direct comparison of the SARs between the channel and the overbanks in the UPF, we combined geobody 2, 3, 4 of the overbank model (Fig. 2.10b). SAR in the overbank model in the UPF is 355 (± 46) (t/m^2/Ma), ~ 2/3 of the SAR in the channel model during UPF (518 (± 39) (t/m^2/Ma); Fig. 2.10).

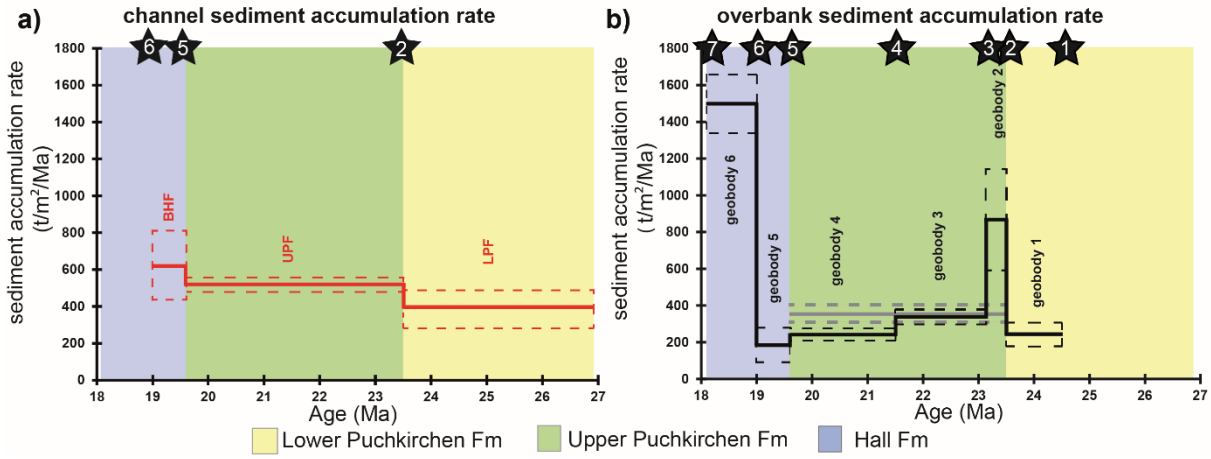

Figure 2.10: Calculated sediment accumulation rates [SARs, (t/m^2/Ma)] of the channel a) and the northern overbanks b), stars indicate the bio- and/or chemostratigraphic constrains of Well H (see Tab. 2.1); 1 = Peak 1 in $\delta^{13}C_{carb}$; 2 = U/LPF boundary (Peak 4 in $\delta^{13}C_{carb}$); 3 = FO *Helicosphaera carteri*; 4 = Peak 11 ($\delta^{13}C_{carb}$ Well H); 5 = Peak 14 ($\delta^{13}C_{carb}$ Well H); 6 = mfs and Sr-Isotoic composition from Maierhof; 7 = Hall/Innviertel boundary (Grunert et al., 2013). The gray bar in b) indicates the combined, average SAR during the UPF onto the northern overbanks. SARs in the channel show variation within their 1σ standard deviation (SD). Note that during geobody 6 (star 6–7) channel sedimentation had ended; therefore, geobody 6 does not represent an overbank setting.

The results of the clinoform dip-azimuth calculation show small variations between the eastern part (NNW dip) of the basin and the western part (NNE dip). However, a dominating northern dip direction was found in the whole basin (Fig. A1.1).

2.5 Discussion

2.5.1 Formation boundaries

In Well H (Fig. 2.5), the ZFM occurs from 2375 to 2325 m. Due to the absence of foraminiferal index species, this interpretation relies on the geochemical data (high TOC and S values, highly negative $\delta^{13}C_{carb}$ values). As nannofossil markers indicative of NP25 or younger are absent, we suggest an age of NP24 which is in agreement with Soliman (2012) and Sachsenhofer et al. (2010). The base of the LPF is defined in Well H by the FO of *Psammosiphonella cylindrica* (2325 m), what is supported by an increase in abundances diversity of the fauna (Fig. 2.5). A distinctive decrease from very high S and TOC values (Fig. 2.5) implies dysoxic to anoxic conditions compared to the more oxygenated conditions of the LPF.

The base of the UPF is located at 2100 m based on the LO of *Psammosiphonella cylindrica* (Fig. 2.5) which is in agreement with the more variable TOC (σ = 0.3 wt%), S (σ = 0.6 wt%), and $CaCO_3$ (σ = 7 wt%) content compared to the LPF (TOC σ = 0.1 wt%; S σ = 0.2 wt%; $CaCO_3$ σ = 2 wt%) (Grunert et al., 2015). The FO of *Helicosphaera carteri* at 1920 m indicates nannoplankton zone NN1 (Aubry, 1989). Below 1920 m, we interpret NP 25 based on the general assemblage including common and continuous occurrences of *Sphenolithus ciperoensis* and *Reticulofenestra bisecta*.

The HFM is defined by the FO of *Uvigerina posthantkeni* at 1455 m in Well H. However, based on a pronounced decrease in both, TOC and S, the base of the HFM is placed about 50 m deeper in the section at 1500 m (Fig. 2.5). This significant change in the geochemical signature is typical for the base of the HFM (Sachsenhofer et al., 2017). Hence, we regard this change as a more reliable marker for the HFM than *U. posthantkeni*, which occurs in a single sample between foraminifera-barren intervals (Tab. A1.1). In the HFM the FO of *H. ampliaperta* together with *Helicosphaera scissura* at 1120 m indicates NN2 and the FO of *R. pseudoumbilicus* >7 µm indicates nannofossil zones NN3–NN4 at 910 m (Fig. 2.5). Both findings support the stratigraphic concept of Grunert et al. (2013).

In Well W, the ZFM (3470 – 3200 m) appears similar to the ZFM in Well H, without indicators for neither NP24 nor NP25, high TOC and S values and no index foraminifera indicating the ZFM (Fig. 2.6) nor the Puchkirchen Group. The $CaCO_3$ content is low (A = 25 wt%) and matches values reported in Sachsenhofer et al. (2010) for the ZFM, we assigned these to the ZFM.

From 3320 m upward, the geochemical data show low variability, which is indicative for the LPF (Grunert et al., 2015). Nevertheless, due to the FO *Psammosiphonella cylindrica* (3100

m), we interpret the base of the LPF to be located at 3100 m. The FO of *H. carteri* and presence of *S. delphix* (23.21 – 22.97 Ma; Backman et al. (2012)) indicate the Oligocene/Miocene boundary and the lower boundary of NN1 at 1800 m. The base of the UPF is located between 1560 and 1520 m (Fig. 2.6). The FO of *H. scissura* is recorded at 1424 m, a clear indicator for NN2 (Fig. 2.6; Backman et al, 2012).

The HFM was defined by the FO of *U. posthantkeni* at 1360 m. This is supported by the decrease of TOC and S values that initiates at 1360 m but terminates at 1300 m (Fig. 2.6). The FO of *H. ampliaperta* at 1260 m indicates mid-NN2. The FO of *R. pseudoumbilicus* >7 µm indicates NN3 at 760 m. The FO of *Amphicoryna ottnangensis* (580 m) points to the Innviertel Group.

In Well Z, the geochemical data at 1500 m depth indicates that the section is part of the UPF. TOC and S content are above 1 wt% in the section until 1150 m where both contents decrease (Fig. 2.7). At 1125 m, both curves indicate a minimum, which we interpret as the BHU (Fig. 2.7), whereas the FO of *U. posthantkeni* is recorded shortly above that at 1110 m. The FO of *H. ampliaperta* at 1190 m indicates mid-NN2 (Ćorić and Spezzaferri, 2009).

When our new data are compared to the stratigraphic concept of Grunert et al. (2015), the positions of FOs of the calcareous nannoplankton with regard to the formation boundaries from foraminiferal analysis vary between the analyzed drill sites and the published data. The findings of Well H indicate the FO of *H. carteri* in the UPF (Figs. 2.3, 2.11) whereas Grunert et al. (2015) report it from the LPF. The FO of *H. ampliaperta* in Well H is located in the HFM, which Grunert et al. (2015) found in the UPF. An earlier occurrence is possibly not recorded as the 400 m below the FO are barren of nannofossils. In Well W, the FOs of *H. carteri* and *S. delphix* (1800 m) mark the Oligocene/Miocene boundary within the LPF (Figs. 2.6, 2.11) and support the results of Grunert et al. (2015). However, the FO of *H. ampliaperta* is recorded within the HFM at this site. *H. ampliaperta* specimens were large in size (~10 µm), indicating that the recorded FO does not correspond to the actual base of the taxon range, as specimens are generally smaller (~ 4 – 6 µm) at its stratigraphic base occurrence (Grunert et al., 2015; Holcová, 2009). The FO of *H. scissura* is already recorded below the BHU. This FO normally occurs before *H. ampliaperta* (Grunert et al., 2015). Therefore, we interpret the FO of *H. ampliaperta* in Well W as delayed, due to the erosive activity of the channel at the BHU (Fig. 2.11). In Well Z, the FO *H. ampliaperta* is also reported below the BHU (Ćorić and Spezzaferri, 2009) which agrees with the concept of Grunert et al. (2015).

Sample contamination of the investigated drill cuttings by sediment movement during the drilling process and upward transport of cuttings potentially pose significant obstacles for biostratigraphic interpretation. We consider contamination unlikely in the present study, because the order of FO of the index nannofossils in each sampled well is agreement with

their order of appearance in the open ocean (Martini, 1971). The results of the $\delta^{13}C_{carb}$ analysis and its good match to the global record (Cramer et al., 2009) further suggest comparable depositional ages. This illustrates that the temporal lag of migration of the nannoplankton between the open ocean and the Oligocene/Miocene western part of the Paratethys – a highly restricted marginal sea (Rögl, 1998) – is small and mainly controlled by our sampling rate and/or the preservation.

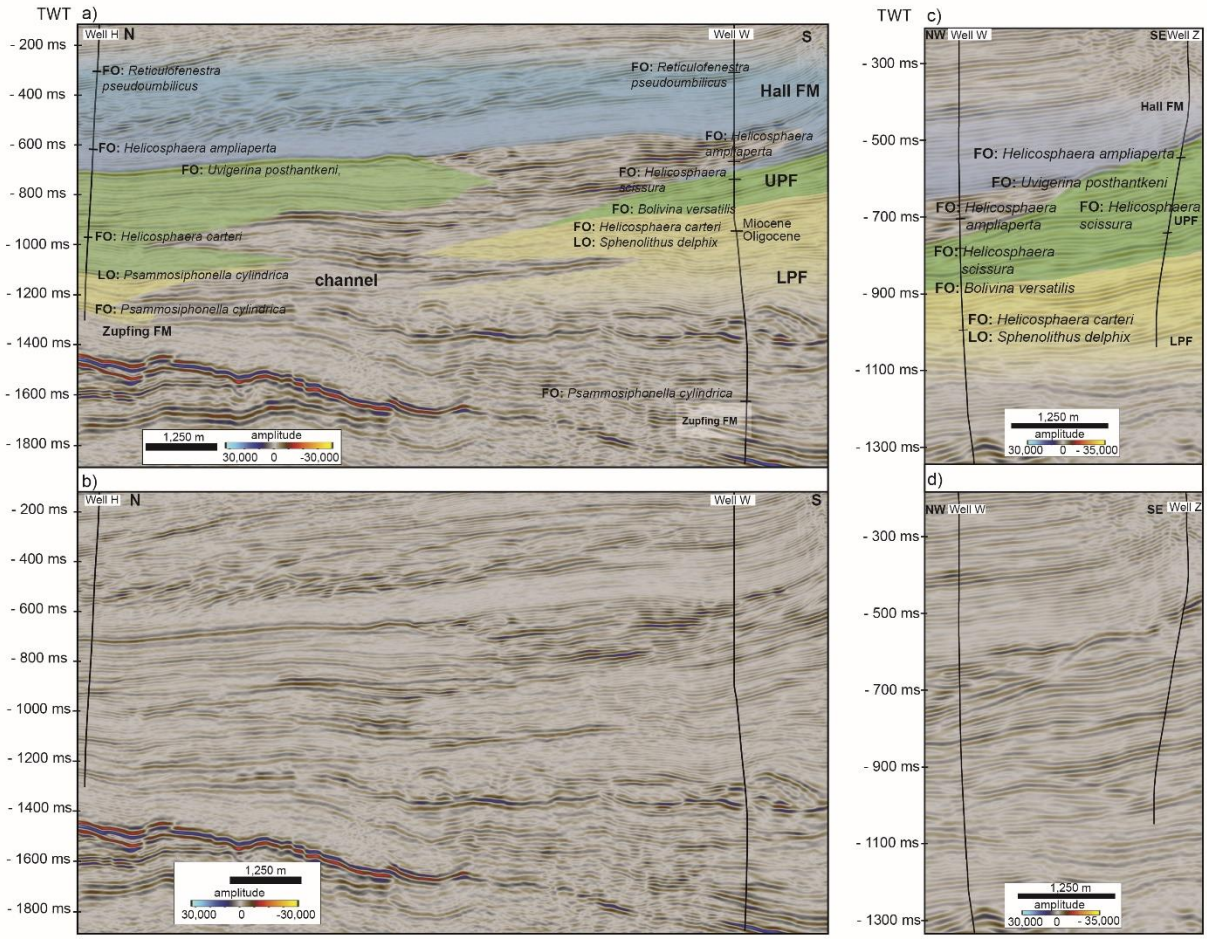

Figure 2.11 a, b: Seismic cross section from Well H to W (for location see Fig. 2.1), (a) interpreted section, (b) un-interpreted section, with first and last occurrences of index taxa, note the difference in strata thickness on the northern and southern side of the channel. In Well W, the boundary of ZFM/LPF was drilled ~600 m deeper, than in Well H. The boundary LPF/UPF differs significantly on the northern and southern side of the channel, probably due to differences in biofacies, while the facies independent nannofossil *Helicosphaera carteri* has its FO approximately at the same depth. **c, d:** Seismic cross section from Well Z to W (for location see Fig. 2.1), (c) interpreted section, (d) un-interpreted section, with first and last occurrences of index taxa, note the great lateral variability of sediment thickness on the southern slope and the filled up, paleo-relief created by slope failure. The erosive character of the channel is well visible in Well W and is responsible for the delayed FO of *Helicosphaera ampliaperta*. Note that the UPF/LPF boundary in Well Z is correlated from Well W. In a and c the channel was excluded from the interpretation.

The variations in the position of the Oligocene/Miocene boundary (LPF in Well W and Hochburg1; Grunert et al., 2015; UPF in Well H, Figs. 2.5, 2.6, 2.11) is attributed to the facies-dependency of benthic foraminifera that are used to define the formations (Küpper and Steiniger, 1975). Benthic foraminifera are highly responsive to ecological changes at the sea floor (Murray, 2006). The proximity of the channel creates a highly dynamic paleoenvironment with significant lateral biofacies variability ultimately impacting the correlation across the channel-belt by benthic foraminifera analysis (Fig. 2.11) (Grunert et al., 2015; Grunert et al., 2013). This influences the formation boundaries which are based on benthic foraminifera as these changes are very likely to be local rather than basin-wide. This also heavily impacts the correlation across the channel-belt (Fig. 2.11). These problems are manifest in problems with the identification of the LPF/UPF boundary. The boundary is hard to identify (Figs. 2.5, 2.6), facies-dependent (Fig. 2.11), and an artificial one.

The FOs of the nannofossils are facies independent and therefore a more reliable way to correlate strata across the channel-belt and to global chronostratigraphy (Fig. 2.11) (Backman et al., 2012). However, the low abundance, generally poor preservation of nannofossils, and sampling resolution complicate biostratigraphic correlation, resulting in the observed diachroneity of nannofossil datums between wells (Fig. 2.11). On the southern basin slope, the proximity of our sampled locations to their sediment sources created a sedimentological environment that is laterally highly variable (Fig. 2.11c) and further complicated by occasional mass-wasting events (Covault et al., 2009; Hinsch, 2008; Kremer et al., 2018).

2.5.2 Stratigraphic correlation based on $\delta^{13}C_{carb}$, biostratigraphy and temporal duration of unconformities

The newly acquired results from the $\delta^{13}C_{carb}$ analysis are supported by our biostratigraphic results. When compared to the global curve after Cramer et al. (2009), the $\delta^{13}C_{carb}$ data from Well H show similar trends (Fig. 2.9). A prominent feature of the global carbon isotope curve is a plateau of positive values at the beginning of the Aquitanian (NN1 to lower part of NN2, ~23.13 to 21.7 Ma) with four positive peaks. This plateau occurs in the global $\delta^{13}C_{carb}$ stack after a steady increase during the upper part of NP25 interrupted by four local minima, at 23.3 Ma, 23.5 Ma, 23.9 Ma and 24.2 Ma. Data from Well H suggest a similar trend of increasing $\delta^{13}C_{carb}$ values from 2250 m with distinct minima at 2010 – 1960 m, 2090 m, 2120 m and 2200 m (upper NP25). At 24.5 Ma the global $\delta^{13}C_{carb}$ curve indicates a maximum, a similar feature is shown at 2290 m in the data from Well H. These findings imply a duration of ~24.5 to 23.5 – 23.2 Ma for the deposition of the LPF (Fig. 2.9).

The plateau (23.0 to 21.8 Ma, Fig. 2.9) in the $\delta^{13}C_{carb}$ curve (Cramer et al., 2009) is mirrored in the data from Well H between 1890 and 1740 m. This interpretation is in good agreement with the FO *Helicosphaera carteri* at 1920 m, indicating an age of 23.13 Ma.

The global $\delta^{13}C_{carb}$ data decrease quickly from the previous plateau to lower values at ~21.5 Ma and stay at low values during the remaining NN2. Significant negative excursions are noticeable at 20.8 Ma, 20.4 Ma, 20.2 Ma, 20 Ma, 19.6 Ma, and 18.8 Ma (Fig. 2.9). The decrease in isotopic values of the global stack is recorded by the data of Well H at 1710 m, indicating an age of 21.5 Ma and for the minima in $\delta^{13}C_{carb}$ data at 1610 m an age of 20.8 Ma. We correlate the maxima at 1590 m and two minima at 1560 m and 1480 m in the $\delta^{13}C_{carb}$ record from Well H to minima in the global curve at 20.2 Ma, 20 Ma or 19.6 Ma. In contrast to well Hochburg1 (Grunert et al., 2015), erosion at Well H was minor or absent at the BHU (Fig. 2.11). Grunert et al. (2015) assigned an age of 19.5 – 18.9 Ma for the BHU by extrapolating sedimentation rates. We suggest that the negative $\delta^{13}C_{carb}$ values in our samples at the BHU (1510 m) can be correlated to the negative excursion at 19.6 Ma on the global $\delta^{13}C$ curve. This implies a time span of 23.5 – 23.2 Ma to 19.6 Ma for the UPF at Well H (Fig. 2.9).

This interpretation is supported by $^{87}Sr/^{86}Sr$ data from Janz and Vennemann (2005). These authors presented the isotopic composition (O, C, Sr, and Nd) of brackish ostracods from an outcrop at Maierhof at the northern boundary of the NAFB (Fig. 2.4e). The outcrop is interpreted to record a middle Eggenburgian maximum flooding surface (mfs) accompanied by the FO *Elphidium ortenburgense* (Wenger, 1987). Janz and Vennemann (2005) inferred open marine conditions at Maierhof in the middle Eggenburgian from their results. When tuned to the global $^{87}Sr/^{86}Sr$ curve (McArthur et al., 2012), the isotopic values from Maierhof indicate a depositional age of 19.1 to 18.9 Ma. Grunert et al. (2013) postulated that the termination of submarine channel sedimentation in the BHF was associated with a maximum flooding surface at well Hochburg1 and the FO of *Elphidium ortenburgense*. The interpretation that the negative $\delta^{13}C_{carb}$ excursion at 1480 m is related to the negative excursion at 19.6 Ma on the global carbon isotopic stack is supported by these ages, as there is no other large negative excursion at that time in the global record (Fig. 2.9). Increasing $\delta^{13}C_{carb}$ values above the BHF can be correlated to the global stack of Cramer et al. (2009) at 19 Ma. These results imply a time span of 19.6 to 19.1 – 18.9 Ma for the BHF and the timing of the BHU on the overbanks. From 1370 m until the top of the section, the $\delta^{13}C_{carb}$ data from Well H do not reflect global trends.

Diagenetic alteration of the original $\delta^{13}C_{carb}$ signal due to the release of ^{12}C from sedimentary organic matter or clay minerals (Marshall, 1992) is unlikely to explain the trend in $\delta^{13}C_{carb}$ in Well H. In most samples from Well H, the $CaCO_3$ content is > 20 wt% and statistical analysis shows no correlation between carbonate content and the carbon isotope record (R^2 = 0.03).

Only in samples from 1740 – 1510 m, $CaCO_3$ contents are low (≥ 7 wt%), nevertheless, the CaCO3 and $\delta^{13}C_{carb}$ values show no correlation (R^2 = 0.07) in this part. The $\delta^{13}C_{carb}$ and the $\delta^{18}O_{carb}$ data from Well H do not correlate (R^2 = 0.1). Therefore, we argue against an influence of diagenetic alteration to this dataset.

The $\delta^{13}C_{carb}$ values from Well W (Fig. A4) do not resemble the trends of the global stack or the wells H and Hochburg1 (Cramer et al. (2009). The $\delta^{13}C_{carb}$ values from Well W show a moderate correlation (R^2=0.58) to the $\delta^{18}O_{carb}$ values of the section, we thus refrained from using the data due to a diagenetic overprint.

In Well Z, the $\delta^{13}C_{carb}$ data of the lowermost section show a plateau with three distinct peaks (1435 m, 1395 m, 1325 m, Fig. 2.9). Based on the FO of *Helicosphaera scissura* at 1490 m (Fig. 2.7), we suggest a lower NN2 age for the base of the well. The rapid decrease to negative values (-0.67 ‰) at 1295 m may represent the abrupt decrease of the global $\delta^{13}C_{carb}$ curve at 20.8 Ma. The FO of *Helicosphaera ampliaperta* at 1190 m in Well Z supports the interpretation that the second negative excursion represents the global decrease at 20.44 Ma in the global $\delta^{13}C_{carb}$ curve. From 1190 m upward, the $\delta^{13}C_{carb}$ data of Well Z are highly variable making unambiguous correlation to the global stack difficult (Fig. 2.9). These findings indicate a timespan from 20.92 Ma to < 20.44 Ma for the investigated section of the UPF, with the BHU having an age of < 20.44 Ma.

In context of possible alteration of the isotopic signal due to ^{12}C from organic matter or clays (Marshall, 1992), the data from Well Z indicate only sporadic samples with $CaCO_3$ values of < 20 wt%. The isotopic data from the UPF section shows no correlation with the $CaCO_3$ content (R^2=0.03), but the data from above the BHU indicate a weak correlation (R^2=0.39). Therefore, diagenetic alteration is considered unlikely for the samples within the UPF, whereas in the HFM such a bias may be present.

2.5.3 Revisiting the stratigraphic concept for the Upper Austrian Molasse

Grunert et al. (2015) have introduced a new stratigraphic concept for the Puchkirchen Group and the overlying Hall Formation. The results presented here support, improve and expand this concept (Fig. 2.12). The samples from the ZFM in Well H and Well W suggest an intra-NP24 age. This intra-NP24 age is in agreement with the results of Soliman (2012) and Sachsenhofer et al. (2010) from dinoflagellate cysts and calcareous nannoplankton, respectively. Furthermore, Soliman (2012) stated that the ZFM contains the Rupelian/Chattian boundary (28.09 Ma), indicated by a peak in *Rhombodinium draco* in the lower part of the ZFM. Therefore, a depositional age of 29.6 to 28.1 - 26.9 Ma for the ZFM is likely.

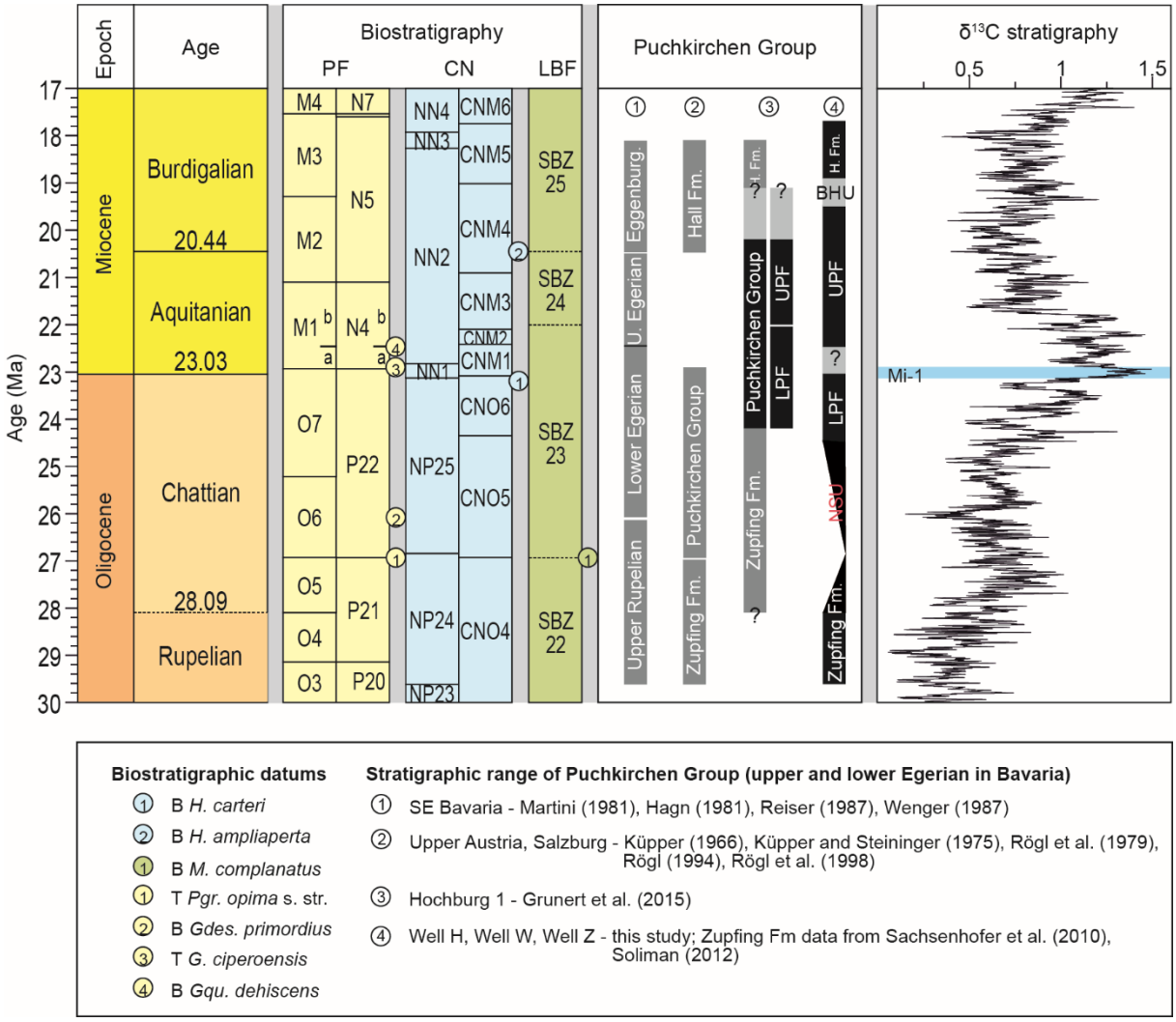

Figure 2.12: Summary of the proposed stratigraphic concepts (number 1, 2, 3) of the Puchkirchen Group and the concept presented here (4). Planktonic foraminifera (PF) zonation follows Wade et al. (2011) and Gradstein et al. (2012); calcareous nannoplankton (CN) zonation follows Backman et al. (2012); Gradstein et al. (2012), and Agnini et al. (2014); larger benthic foraminifera zonation follows Cahuzac and Poignant (1997) and Gradstein et al. (2012). Global $\delta^{13}C_{carb}$ stack from Cramer et al. (2009). Gray bars indicate uncertainties, BHF summarized as BHU. See text for details. Redrawn after Grunert et al. (2015).

The base of the Puchkirchen Group on the northern slope is now well dated to ~ 24.5 Ma based on the data from this study and Grunert et al. (2015). Sedimentation on the northern basin slope started after a period of non-deposition from < 28.1 Ma (Soliman, 2012) to ~ 24.5 Ma (Fig. 2.12), which is expressed in the NSU (Masalimova et al., 2015). Nevertheless, it is unclear whether a similar hiatus is present along the axis of the basin or if deposition of the Puchkirchen Group began earlier here than on the northern slope. In the 3D seismic-reflection data, no indication for a large-scale hiatus was found. Our efforts to date the ZFM/LPF boundary in Well W were unsuccessful due to diagenetic alteration of $\delta^{13}C_{carb}$ and further investigations are necessary to solve this question. Today, a difference in depth of ~600 m is

separating the ZFM/LPF boundary in Well H and W (Fig. 2.11). The diachronic deposition of sediments on a passive margin and the axial part is a well-documented feature of underfilled, wedge-shaped foreland basin (DeCelles and Giles, 1996) and has also been described in the western part of the NAFB (Sinclair, 1997). Therefore, we argue against a significant hiatus in the central part of the basin and propose an age of 26.9 Ma (base NP25) to 24.5 Ma for the base of the LPF (Fig. 2.12).

The age of the boundary between the Lower and Upper Puchkirchen Formation can be constrained by carbon isotope data to ~ 23.5 Ma in Well H (Fig. 2.9), from calcareous nannoplankton in Well W to 23.1 – 20.4 Ma (Fig. 2.6) and to > 20.4 Ma from chemo- and biostratigraphy in Well Z (Fig. 2.7). Grunert et al. (2015) postulated an age of 22.2 – 22.0 Ma (Fig. 2.12). The differences can be explained by the facies dependency of the foraminiferal index taxa (section 5.1).

The top of the UPF in Well W and Well Z has been eroded precluding unambiguous correlation with global chronostratigraphy. Nannofossils from Well W and Z indicate an age of < 23.1 Ma and < 20.4 Ma, respectively. At Well H, seismic reflections show no erosion at the BHU (Fig. 2.11). Carbon isotopic correlation indicates an age of ~ 19.6 Ma (Fig. 2.12), which is in good agreement with estimates of Grunert et al. (2015) and $^{87}Sr/^{86}Sr$ data by Janz and Vennemann (2005). The termination of channel sedimentation and the BHF at 19.1 – 18.9 Ma result from a sea-level increase resulting in a mfs at Hochburg1 (Grunert et al., 2013) and Maierhof (Janz and Vennemann, 2005; Wenger, 1987). This correlates well with the middle Eggenburgian mfs which was correlated to global 3rd order sequence Bur2 (Piller et al., 2007) and the mfs in the Swiss NAFB (Garefalakis and Schlunegger, 2019). Nannofossil biostratigraphy from Well H suggests an age of 18.1 Ma for the base of the Ottnangian Innviertel Group above the Hall Formation, which is in good accordance with previous results (Grunert et al., 2013; Grunert et al., 2010).

This stratigraphic framework with the Puchkirchen Group on the northern basin margin ranging from 24.5 to 19.6 Ma – in the axial part of the basin, sedimentation of the Puchkirchen Group is likely to have started before 24.5 Ma – and the Hall Formation spanning from 19.6 to 18.1 Ma agrees with the data from Grunert et al. (2015, 2013) but differs significantly (Fig. 2.12) from previous concepts (Küpper and Steininger, 1975; Rögl et al., 1979). Reasons for these differences were discussed by Grunert et al. (2015). These authors also discussed the complications of the stratigraphic correlation in the Paratethys which arise from the assignment of lithostratigraphic units to regional stages. The regional stages are often defined by locally restricted ecostratigraphy what hampers the correlation (Grunert et al., 2015).

2.5.4 External forcings detected in SARs

Comparing the SARs between the channel and overbank models is not straightforward as sediment is eroded in the channel (Hubbard et al., 2009). Furthermore, the channel continues towards the east where it is affected by thrust tectonics. Hence, the channel in the study area is also subject to sediment bypass and does not form the ultimate sediment sink of the sedimentary system. In fact, the position of the final sink, the submarine fan that is associated with this submarine channel is currently unknown (Hubbard et al., 2009). The Puchkirchen channel system represents a sediment-transfer zone for the Alpine detritus. Therefore, decreased channel SARs may be interpreted as decreased sediment supply or as periods of increased sediment bypass. Sediment on the northern overbanks might remain in the basin over longer time scales as it is remobilized only by channel-meander bend migration and associated erosion into the underlying overbank deposits, channel avulsion (undocumented in the study area), and/or levee breaches (Hubbard et al., 2009). Therefore, the overbanks may represent a local, terminal sink.

Overbank geobody 2 shows a 3.5-fold increase in SAR from 23.5 to 23.1 Ma (Fig. 2.10). On the shelf, Zweigel (1998) showed prograding and aggrading clinoforms with a high SAR which might be linked to increased sediment flux from the exhumation of the Lepontine Dome. This is followed by a sea-level highstand at the Oligocene/Miocene boundary as indicated by the deposition of marly claystones (Zweigel, 1998). The increase in the overbank SAR around 23.5 Ma might be related to the high SARs on the shelf before the Chattian/Aquitanian boundary, which in turn may be related to the exhumation on the Lepontine Dome.

However, we favor an alternative explanation related to an autogenic process within the channel system, because of the drastic SAR increase and the short duration (~0.4 m.y.) of increase: During the deposition of overbank geobody 1, the channel showed a slightly sinuous course and a northward-directed, subtle meander bend located on the northern edge of the seismic cube (Fig. 2.13a). During the deposition of overbank geobody 2, the channel meander adjacent to the overbank volume abruptly changed its course to the south (Fig. 2.13b) forming a pronounced meander bend and a broad northern overbank plain (Figs. 2.2, 2.8, 2.13). The channel was forced to change its geometry due to plugging by debris-flow deposits sourced from the west (Masalimova et al., 2015). The increase in sinuosity probably led to an increase of flow stripping of the upper part of channel-traversing turbidity currents onto the northern overbanks. The upper surface of the NSU is characterized by southward (channel)- directed gullies, that transported material into the main channel belt (Fig. 2.13a, Masalimova et al. (2015)). Such gullies are absent after the change in channel-meander geometry (Fig. 2.13b). Increased flow stripping and the absence of gullies have led to a uniform and widespread

deposition of sandstones on the overbanks (Masalimova et al., 2015). Therefore, the dramatic increase in SAR between 23.5 and 23.1 Ma (Fig. 2.10b) is interpreted to be the result of an autogenic change in channel geometry.

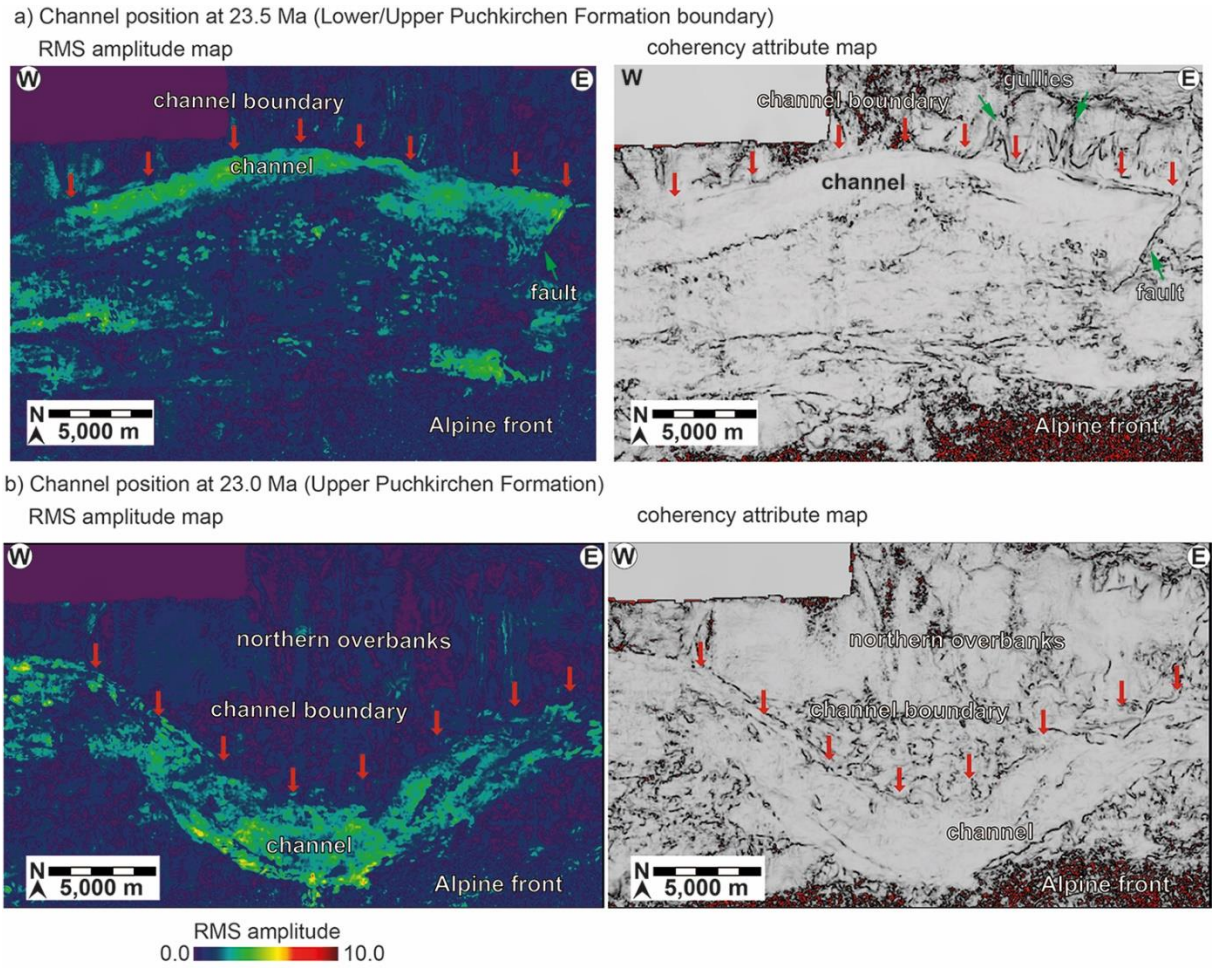

Figure 2.13: RMS amplitude and coherency maps of the channel and overbank area (for position see Figure 3b) at 23.5 Ma a) and 23.0 Ma b). At 23.5 Ma a) the channel is close to the northern border of the seismic cube, the overbanks are narrow. Until 23.0 Ma b) the channel changes its position close to the Alpine thrust front and creates wide, northern overbanks. Red arrows mark the channel boundary, green arrows the gullies on the NSU and a fault.

Results from laboratory and numerical models suggest, that overbanks of high sinuous channels show increased SARs due to overspill than those overbanks of low sinuous channels (Amos et al., 2010; Huang et al., 2012). The observed increase in sinuosity of the channel from ~1.05 at 23.5 Ma to ~1.14 at 23.0 Ma (Fig. 2.13) is in line with these results and further supports our interpretation of an autogenic SAR increase. Furthermore, on the Monterey Fan and channel system, Fildani et al. (2006) observed a similar fourfold increase in sedimentation rates in areas of increased flow stripping when compared with background overbank sedimentation.

Geobody 5 records stable and low SAR on the overbanks (compare to geobody 4 overlap within their standard deviation; Fig. 2.10, Tab. 2.1). As reported by de Ruig and Hubbard (2006), the uppermost UPF and BHF show a decrease in grain size and an increase in mud content, which suggests a reduction of turbidity-current height, density and/or competence. The turbidity currents in the channel became less efficient in spilling their diluted tops onto the overbanks. This process also explains the two characteristics of the BHU in the seismic-reflection data (Fig. 2.2): Whereas on the northern overbanks the section above and below the BHU is characterized by continuous, high-amplitude reflectors, the channel around the BHU is highly erosive – evidenced by truncated reflectors and the biostratigraphic results from Well W (Figs. 2.2, 2.6, 2.11, late appearance of *H. ampliaperta*, see section 5.1 for discussion).

The SARs from the channel and overbank model in the time interval from 19.6-19.0 Ma are directly linked to the process which has caused the formation of the BHU. Zweigel (1998) pointed out that on the Bavarian Shelf the SAR became negative (erosion) in her Sequence 4a (interval below BHU, Fig. 2.3). Sequence stratigraphy (Jin et al., 1995; Zweigel, 1998) as well as foraminifera analysis (Wenger, 1987) indicate a major sea-level decrease in the eastern NAFB. Erosion on the shelf (Zweigel, 1998) points to a redeposition of shelf sediments into the deeper basin in the period from 19.6 – 19.0 Ma also evident by the foraminiferal fauna in the channel sediments in Hochburg1 (Fig. 2.1) (Grunert et al., 2013). If from 19.6 – 19.0 Ma the channel was mainly fed by redeposited material from the Bavarian Shelf, sediment-supply rates from the hinterland must have dropped accordingly within this period to maintain the relatively constant and low SARs. Consistently, Kuhlemann (2000) described on the Egerian/Eggenburgian boundary (Fig. 2.12) a ~45% decrease in sediment-supply rates from the Eastern Alps and a decrease of ~35% in rates from the Central Alps.

Zweigel (1998) explained her findings on the shelf (sediment starvation, an angular unconformity, uplift in the northern part of the NAFB, decrease in sea level, deepening of the basin at the axis) with the visco-elastic relaxation of the European Plate that has caused an uplift of the forebulge, propagation of the bulge towards the orogenic front and a decrease in elevation in the hinterland. This would explain the decrease in sea level, the erosion and redeposition of older foreland sediments into the deeper basin through uplift and subareal exposure of parts of the shelf, and the decrease in sediment-supply rates and grain size related to a decrease in elevation in the Alpine hinterland. Zweigel's (1998) model is further in line with the ceasing of northward progradation of the Eastern Alpine front during the UPF (Hinsch, 2013). The uplift and progradation of the forebulge does not require a northward progradation of the thrust front as the stress relaxation of the lithospheric plate is dependent on temperature, rheology, and initial stress (Beaumont, 1981). The doubling in lag times in apatite fission track ages from the proximal archives of the paleo-Inn from 2-4 Ma in Aquitanian to 6-8 Ma in

Burdigalian sediments (Kuhlemann et al., 2006) further support relief reduction in the hinterland. We therefore interpret the BHU as the result of a period of non-sedimentation on the overbanks and, likely, in the channel, followed by a period when the channel was fed by remobilized shelf sediments. Grunert et al. (2013) pointed out that the channel in Hochburg1 (Fig. 2.1) cuts into the UPF, deposited middle Eggenburgian strata but lower Eggenburgian strata (Fig. 2.3) is missing. Therefore, we suggest that the period of non-sedimentation extends over the entire early Eggenburgian.

After the mfs at 19 Ma, the SAR indicates an 8-fold increase compared to the geobody 5 (Fig. 2.10, 4.5-fold increase compared to geobody 3). During this period – the beginning of the Upper Marine Molasse – channel sedimentation terminated and hemipelagic sedimentation (Figs. 2.2, 2.3, 2.4) was established (middle Eggenburgian), which was replaced by clinoform progradation from the southern margin into the basin in the late Eggenburgian. These clinoforms indicate a sediment transport direction roughly from S to N (Figs. 2.2, 2.8, A1.1) (Grunert et al., 2013). It is likely that the clinoform progradation caused the tremendous increase in the SAR from 19 to 18.1 Ma (Fig. 2.12).

During the period from 19.0 to 18.1 Ma, the basin shallowed from 1,000 – 1,500 m water-depth (Grunert et al., 2013) to water-depths < 200 m (Grunert et al., 2012). The basin was transformed from an underfilled foreland basin (characterized by wedge-shaped deposits) to a filled one (sedimentary deposits tabular) (Fig. 2.2), an evolution that occurred ~ 11 Myr earlier in the Swiss part of the NAFB (Sinclair, 1997). The shallowing trend cannot be explained by eustatic sea-level fall (Haq et al., 1987) or a drastic change in subsidence patters in the basin (Genser et al., 2007). Instead, the basin was filled-up by sediments deposited by prograding clinoforms (Figs. 2.2, 2.10). The migration direction of the clinoforms (from S to N, Figs. 2.2, A1.1) indicate a southern source. Detrital zircon U-Pb ages further suggest a change in provenance, when compared to the underlying UPF (Sharman et al., 2018). The provenance change and the predominantly northward directed sediment supply is consistent with redeposition of the Augenstein Formation on top of today's Northern Calcareous Alps (Frisch et al., 2001).

Two of the four expected external forcings are mirrored in the SARs of the Oligocene/Miocene Upper Austrian NAFB; the visco-elastic relaxation of the European Plate at 19.6 – 19 Ma and the unroofing and redeposition of the Augenstein Formation from 19.0 Ma onward. However, our data do not record the initially hypothesized doubling in SAR in connection with the external signals of the exhumation of the Lepontine Dome and the Tauern Window. Both signals were described within the proximal sedimentary archives in the Swiss NAFB (Schlunegger and Norton, 2015) and the south-east German NAFB (Fig. 2.4; Ganss, 1977). In case of the external forcing of the Lepontine Dome, signal shredding may have occurred within the fluvial

sediment-transfer zone. Sediments travelled a distance of ~500-600 km from the proximal archives into the deep-marine sink. The intermittent basins, the Swiss and German NAFB, created transient accommodation space along the sediment-routing system in which the excessive sediment load was stored (Kuhlemann and Kempf, 2002) and, hence, the tectonic signal is not manifested in the SARs of the marine transfer zone of the study area.

The increase in SAR of ~65–100 % (Ganss, 1977) described from the deep-marine section (Wenger, 1987) of the Chiemgau Fan (Fig. 2.4) and related to the exhumation of the Tauern Window in the Eastern Alps is also not recorded in our SAR results. At present, the Chiemgau Fan is located merely ~70 km south-west of our research area (Fig. 2.4). This implies that the Puchkirchen channel system has been very efficient in bypassing sediments. The channel system is characterized by low sinuosity (1.05 – 1.5; (De Ruig and Hubbard, 2006)) and the absence of avulsions (Hubbard et al., 2009) throughout the >7.4 Myrs of channel activity, possibly due to the lack of available space in the narrow (<20 km) foreland (Hubbard et al., 2009). These channel characteristics may increase bypass efficiency through the reduction of areas of sediment deposition, such as channel-avulsion strata and lateral accretion at inner meander bends. The bypass efficiency of the system may be an additional reason for the non-recording of the signal from Lepontine-Dome exhumation.

After the reorganization of the NAFB at 19 Ma, resulting in the termination of channel sedimentation and the decrease of bypass efficiency of the sediment-routing system, the basin in the study area evolved from the marine transfer zone to the marine, terminal sediment sink. Hence, the sedimentary archive in the Upper Austrian NAFB was able to record the redeposition of the Augenstein Formation.

2.5.5 Geodynamic implications

With the new stratigraphic results, we are able to further constrain the evolution of the basin. The NSU formed between 28.1 (Soliman, 2012) and 26.9 Ma (Fig. 2.14). Masalimova et al. (2015) suggested a tectonically-induced oversteepening of the northern basin slope due to a deepening of the basin axis. A temporal correlation exists with a northward advance of the Alpine thrust front (Kuhlemann and Kempf, 2002) as well as the final nappe stacking and crustal thickening in the Eastern Alps (Frisch et al., 2000). Both processes lead to an extra load onto the European Plate and could account for the basin deepening.

During the deposition of the Puchkirchen Group, sedimentation rates in the basin were mainly controlled by autogenic processes (Fig. 2.14). However, minor tectonic activity is evident in the basin on the southern slope where Penninic and Helvetic thrust sheets overthrusted and partly

incorporated Puchkirchen strata (Covault et al., 2009; Hinsch, 2013). The northward progradation of the Alpine front ceased in the UPF and the deformation stepped back into the orogenic wedge (Hinsch, 2013).

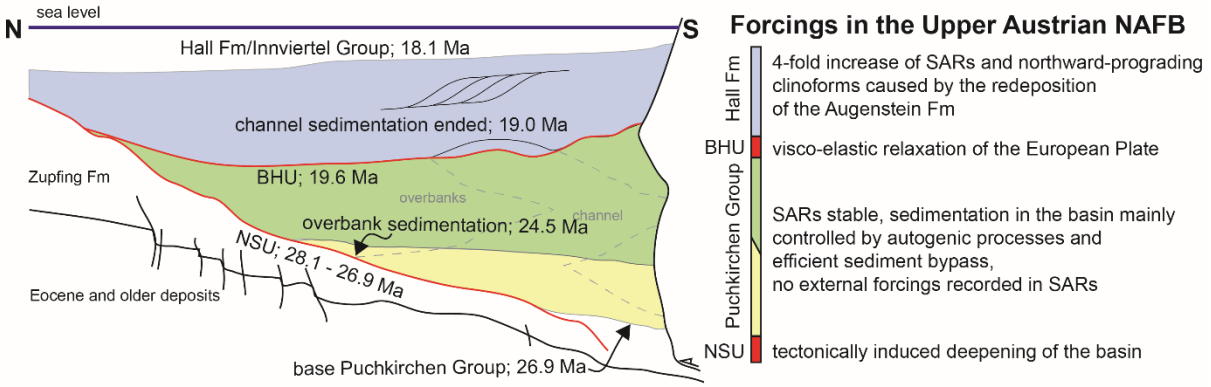

Figure 2.14: Schematic cross section through the Upper Austrian NAFB, with the Puchkirchen Group (yellow and green) and the Hall Fm (blue) and the dominating processes in the basin. Important steps in basin evolution were newly dated with the NSU (lower red line) being established at 28.1 – 26.9 Ma. Puchkirchen Group sedimentation started at 26.9 Ma in the axial part of the basin and at 24.5 Ma on the overbanks. The BHU (upper red line) is now dated to 19.6 – 19.0 Ma and the termination of channel sedimentation to 19.0 Ma. The Hall Fm (19.6 – 18.1 Ma) recorded the filling of the basin. See text for discussion.

The northern NAFB was uplifted (Zweigel, 1998) at 19.6-19.0 Ma, reflected in the change in sediment-transport direction (Figs. 2.2, 2.4, 2.14). The Puchkirchen channel consistently funneled sediments to the east (De Ruig and Hubbard, 2006) indicating an eastward-directed slope in the basin. The northward migration of the clinoforms in the HFM (Figs. 2.4, A1.1) indicate that either the deep eastern basin part was cut off from the Puchkirchen Trough or the eastern part was uplifted. In the upper HFM (19.0-18.1 Ma), the Upper Austrian NAFB turned from an underfilled basin to a filled one further indicating an absence of subsidence (Fig. 2.14). In contrast, the Southern Alpine Foreland Basin (Venetian and Friuli Basin) of the Eastern Alps from late Burdigalian (~17 Ma) onward experienced higher subsidence rates and South-Alpine thrusts emerged (Mellere et al., 2000). These findings might indicate that the former pro-wedge foreland basin, the NAFB, was turned into a retro-wedge position, and the former retro-wedge basin, the Southern Alpine Foreland Basin, into a pro-wedge one. Taking this interpretation further, our and Zweigels (1998) findings could be interpreted as the surface expression of the postulated northward retreat and tearing event of European lithospheric mantle underneath the Eastern Alps at 25-20 Ma (Handy et al., 2015) as part of an early Miocene switch in subduction polarity to present northward subduction of the Adriatic Plate (Lippitsch et al., 2003). However, the subduction polarity switch and the exact timing and geometry of slab tearing are subject of extensive ongoing research (Handy et al., 2015, ongoing research of the

Priority Program “SPP – Mountain building processes in 4D” of the German Research Foundation). At the current stage, the model of a slab polarity switch fails to explain the uplift of the forebulge in the German NAFB (Zweigel, 1998) and the redeposition of shelf strata into the deeper basin. Therefore, at present we prefer the model of visco-elastic relaxation of the lithosphere (Zweigel, 1998) to explain our results.

2.6 Conclusion

The results from the analysis of foraminifera, calcareous nannoplankton, geochemistry (TOC, S, $CaCO_3$, $\delta^{13}C_{carb}$) and spatially averaged SARs provide new constraints for the evolution of the Upper Austrian NAFB. Deep-marine sedimentation in the basin started with the Zupfing Formation (NP24), the Puchkirchen Group formed during NP25 to NN2 (26.9 – 19.6 Ma), and the Hall Formation accumulated during NN2 – NN3 (19.6 – 18.1 Ma). Deposits of the Puchkirchen Group are diachronic between the central basin axis and the northern overbanks. The differentiation between Upper and Lower Puchkirchen Formation first postulated by Papp and Steininger (1975) and perpetuated in most following studies proved to be difficult to identify and facies dependent.

Both large-scale unconformities in the basin were dated. The NSU was established between 28.1 – 26.8 Ma, possibly due to a tectonically induced oversteepening of the basin caused by an extra load onto the European Plate either related to a thrust front progradation or the final nappe stacking period in the Eastern Alps. The BHU (19.6 – 19.0 Ma) resulted from a period of non-sedimentation in the basin, followed by a period of redeposition of sediments from the shelf in Bavaria (Grunert et al., 2013).

The results of our SAR calculation show changes in SARs which are possibly related to two of the four expected tectonic forcings in the Oligocene/Miocene Upper Austrian NAFB. We did not detect the hypothesized doubling of SAR caused by the exhumation of the Lepontine Dome (Central Alps) and the Tauern Window (Eastern Alps), which is present in proximal (Bavarian and Swiss) sediment archives. These signals were either ‘shredded’ in the foreland during long (500-600 km) eastward sediment transport or not recorded in the deep-marine setting due to efficient sediment bypass within the submarine channel system.

A change in the foraminiferal assemblages suggests sediment reworking on the shelf and stable SARs despite a sea-level fall from 19.6-19.0 Ma. This period of sediment remobilization is interpreted as the result of the visco-elastic relaxation of the European Plate. This relaxation induced uplift in the shelf area of the basin and a decrease in relief in the hinterland, leading to stable SARs by the enhanced input of reworked shelf sediment.

The maximum SARs from 19.0 Ma onward are interpreted to result from unroofing and redeposition of the Augenstein Formation. This interpretation is furthermore supported by a shift in sediment-transport direction from east to north via northward prograding clinoforms and a major shift in sediment provenance (Sharman et al., 2018). During this time, the study area was transformed from a deep-marine transfer zone to a final sediment sink, efficiently preserving the tectonic signal in the SARs.

In the Hall Formation (19.6 – 18.1 Ma), the Upper Austrian NAFB experienced major changes in basin geometry (from underfilled to filled), subsidence, drainage network, and the ceasing of deformation along the Alpine thrust front (Hinsch, 2013). These changes may point to a large-scale orogen-wide reorganization triggered by a change in slab polarity (Handy et al., 2015; Lippitsch et al., 2003) which turned the former pro-wedge (>19.0 Ma) Upper Austrian NAFB into a retro-wedge setting.

Chapter 3: Detrital apatite geochemistry and thermochronology from the Oligocene/Miocene Alpine foreland record the early exhumation of the Tauern Window

This chapter has been published as:
Hülscher J., Sobel E. R., Verwater V., Groß P., Chew D., and Bernhardt A. (2021). Detrital apatite geochemistry and thermochronology from the Oligocene/Miocene Alpine foreland record the early exhumation of the Tauern Window. In Basin Research, v. 33, p. 3021– 3044. DOI: 10.1111/bre.12593

Abstract

The early exhumation history of the Tauern Window in the European Eastern Alps and its surface expression is poorly dated and quantified, partly because thermochronological and provenance information are sparse from the Upper Austrian Northern Alpine Foreland Basin. For the first time, we combine a single-grain double-dating approach (Apatite Fission Track and U-Pb dating) with trace-element geochemistry analysis on the same apatites to reconstruct the provenance and exhumation history of the late Oligocene/early Miocene Eastern Alps. The results from 22 samples from the Chattian to Burdigalian sedimentary infill of the Upper Austrian Northern Alpine Foreland Basin were integrated with a 3D seismic-reflection dataset and published stratigraphic reports. Our highly discriminative dataset indicates an increasing proportion of apatites (from 6 % to 23 %) with Sr/Y values <0.1 up section and an increasing amount of apatites (from 24 % to 38 %) containing >1000 ppm light rare-earth elements from Chattian to Burdigalian time. The number of U-Pb ages with acceptable uncertainties increases from 40 % to 59 % up section, with mostly late Variscan/Permian ages, while an increasing number of grains (10 % to 27 %) have Eocene or younger apatite fission track cooling ages. The changes in the apatite trace-element geochemistry and U-Pb data mirror increased sediment input from an ≥ upper amphibolite-facies metamorphic source of late Variscan/Permian age - probably the Ötztal-Bundschuh nappe system - accompanied by increasing exhumation rates indicated by decreasing apatite fission track lag times. We attribute these changes to the surface response to upright folding and doming in the Penninic units of the future Tauern Window starting at 29-27 Ma. This early period of exhumation (0.3-0.6 mm/a) is triggered by early Adriatic indentation along the Giudicarie Fault System.

This chapter has been published in Basin Research and can be found online under the following DOI: https://doi.org/10.1111/bre.12593.

Chapter 4: Early bird apatites overhaul clays in provenance-change recording by 4-5 m.y.

This chapter will be submitted to Geology as:
Hülscher J., Sobel E. R., Kallnik N., Hoffmann J.E., Millar I.L., Hartmann K., and Bernhardt A. (XXXX). Early bird apatites overhaul clays in provenance-change recording by 4-5 m.y.

Abstract

Extracting information about past environmental changes from sedimentary archives is a key objective of provenance research. With the unprecedented combination of Nd isotopic composition of the bulk-rock clay-size fraction and apatite single-grain analysis, we gain information about the extent of the area affected by the environmental change. Rupelian to Burdigalian sediments of the eastern Northern Alpine Foreland Basin (NAFB) were sampled to investigate signal propagation in response to tectonically induced Tauern Window exhumation from 28 ± 1 Ma onward. At 23.3 Ma, the detrital apatite source changed from Permo-Mesozoic and late Variscan low-grade metamorphic sources with εNd values ~ -4.9 to late Variscan high-grade metamorphic source with εNd values ~ -2.0. In contrast, εNd values of the bulk rock clay-sized fraction remain stable ~ -9.7 from 27 to 19 Ma but increase afterwards to ~ -9.1. The inferred total signal-lag time of the Tauern Window exhumation is 4-5 m.y. longer in the clay-sized bulk-rock data (8.0-10.3 m.y.) than in the apatite single-grain distribution (3.4-6.0 m.y.). This delay is controlled by the characteristics of the methods applied. Whereas single-grain distributions of orogen-wide sediment-routing systems can be dominated by geographically small areas with high erosion and mineral fertility rates, bulk-rock methods integrate over entire drainage areas diminishing extreme values. By combining those two methods, this areal information is highlighted enabling a previously unattained understanding of the underlying environmental change.

4.1 Introduction

Changes in sediment flux, architecture, and/or provenance in response to an extrinsic forcing – so-called environmental signals – are key to reconstruct Earth's climatic and tectonic history from sedimentary archives (Tofelde et al., 2021). Provenance changes of orogen-wide sediment-routing systems (SRSs) have been interpreted to reflect climatic or tectonic perturbations (Anfinson et al., 2020; Fildani et al., 2018) but making this distinction based on a sedimentary archive remains challenging (Sharman et al., 2019). Climatic perturbations interact with the entire continental and marine SRS (Blum et al., 2018). Resulting provenance changes reflect either a changing erosional focus (Clift and Giosan, 2014) or a drainage reorganization (Fildani et al., 2018). Tectonic perturbations can trigger large-scale drainage reorganizations, leading to changes in sedimentary provenance (e.g. river-capturing processes (Tatzel et al., 2015)); however, tectonic exhumation processes interfere only with segments of an orogen-wide SRS. Related provenance changes imply the exposure of a new

source rock (Anfinson et al., 2020) or a drainage-divide migration driven by surface uplift (Mark et al., 2016).

These differences in the extent of the perturbated area can be emphasized by the application of a combined single-grain and bulk-rock approach. Single-grain analyses deliver specific source-rock information from the investigated grains (von Eynatten and Dunkl, 2012). Fast-eroding areas with a high mineral fertility are highlighted in the single-grain distribution of orogen-wide SRSs (Malusà et al., 2017). In contrast, bulk-rock methods integrate over the entire SRS upstream of the sediment archive (Tofelde et al., 2021), diluting extreme values in e.g. erosion rates or isotopic ratios in the SRS (Wittmann et al., 2016). We hypothesize that these methodical properties are expressed in a temporally delayed provenance change between bulk-rock and single-grain methods in response to tectonic exhumation. The areal exposure of a new source rock in the orogen-wide SRS may initially be too small to change the bulk sediment (isotopic) composition in the sedimentary archive, but large enough to change its single-grain distribution. We test this hypothesis by quantifying total signal-lag times (*sensu* Tofelde et al. (2021)) of a changing sedimentary provenance in response to the tectonic exhumation of the Tauern Window from 28 ± 1 Ma onward (Favaro et al., 2015; Hülscher et al., 2021) by using the exceptional combination of Nd isotope clay-sized bulk-rock and apatite single-grain analysis on Oligocene/Miocene marine clastic sediment of the Upper Austrian NAFB (Fig. 4.1).

4.2 Geological overview

In contrast to the continental depositional environment in the western NAFB from ~28 to 20 Ma (Kuhlemann and Kempf, 2002), the NAFB east of Munich (Fig. 4.1) remained at deep-marine conditions from 28.1 to 18.3 Ma (Grunert et al., 2013; Hülscher et al., 2019). In the Puchkirchen Group and the basal Hall Formation (~27 to 19 Ma, Figs. 4.2, A3.1), depositional processes were controlled by a deep-marine, eastward transporting, gravity-flow dominated channel system along the basin axis (Hubbard et al., 2009; Hülscher et al., 2019). The channel was bounded by wide northern overbanks built from silty marls and sandstones (Hubbard et al., 2009). From the tectonically active southern basin margin, submarine fans prograded into the basin (Hinsch, 2008). East-directed channelized sediment transport terminated after a basin-wide sea-level highstand at 19 Ma and dominantly northward-directed sediment routing via prograding clinoforms commenced (Grunert et al., 2013; Hülscher et al., 2019).

The Upper Austrian NAFB received clastic detritus from 28 to 19 Ma via three SRSs. 1) From Oligocene onward, the Eastern Alps were drained northeastward by the paleo-Inn river (Fig.

4.1) (Brügel et al., 2003). Its headwaters reached the Periadriatic Line in the south and the western Lower Austroalpine nappes (Brügel et al., 2003) and delivered sediment to the northern slope of the Upper Austrian NAFB (Hülscher et al., 2021; Sharman et al., 2018). 2) Upper Austroalpine nappes and the Periadriatic plutons supplied sediment to the southern slope via the Augenstein Formation (Fig. 4.1) (Frisch et al., 2001; Hülscher et al., 2021). 3) A delta system close to Munich (Fig. 4.1) contributed Central Alpine material to the channel (Füchtbauer, 1964; Sharman et al., 2018). The flooding of the NAFB at 19 Ma cut off this SRS (Kuhlemann and Kempf, 2002).

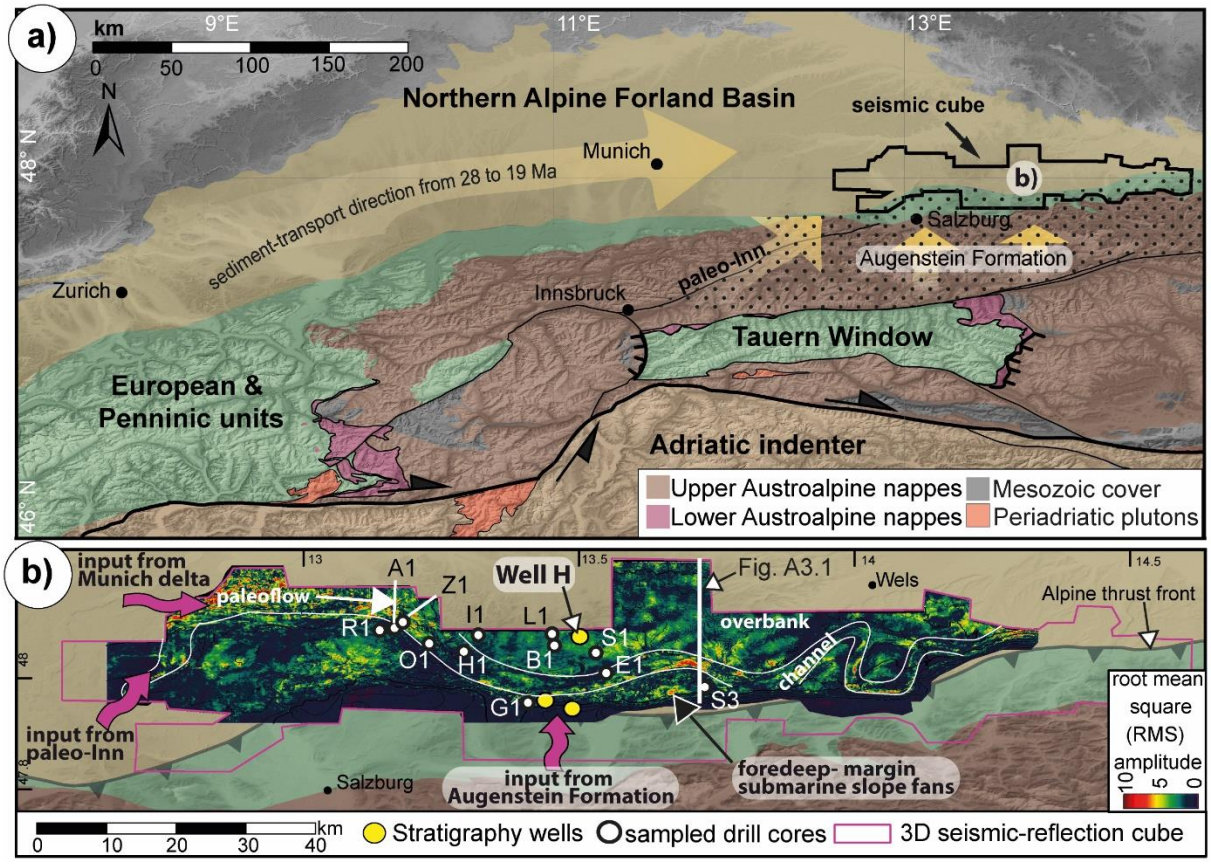

Figure 4.1: Simplified geological map (after Schmid et al. (2004)) of the Alps (a) with the Tauern Window in the east bounded by two normal faults. The location of the seismic cube in the Upper Austrian NAFB is enlarged in (b), where the sample locations are shown. The inset shows an RMS amplitude map in the Hall Formation outlining the meandering, axial channel, the extensive northern overbank deposits and the slope fans on the southern tectonically active margin.

We investigate the environmental response to the tectonically driven Tauern Window exhumation starting at 28 ± 1 Ma (Favaro et al., 2015; Hülscher et al., 2021). After the late Eocene onset of continental collision in the Eastern Alps (Schmid et al., 2004), the ongoing convergence between the upper Adriatic and lower European plate led to large-scale upright folding in the Penninic units of the future Tauern Window (Favaro et al., 2015; Schneider et

al., 2015). This shortening caused exhumation (0.3-0.6 mm/a) of the overlying Upper Austroalpine nappes (Favaro et al., 2015; Hülscher et al., 2021). A resulting provenance change in the detrital apatites in the Upper Austrian NAFB at 23.3 ± 0.3 Ma mirrors an increasing input from a newly exposed late Variscan, high-grade metamorphic Upper Austroalpine source (Fig. 4.2) (Hülscher et al., 2021).

4.3 Samples and Methods

4.3.1 Clay-sized fraction Nd isotope analysis

Drill-cuttings from Well H (Fig. 4.1) on the northern basin slope were analyzed for Nd isotopes in clays-sized sediment. These were separated from the samples via centrifuging and decantation of the suspended fraction. Organic material was removed by ashing at 830°C in a muffle furnace or by chemical dissolution. Neodymium was separated by ion-exchange resin chemistry (see the supplementary material) and analyzed for $^{143}Nd/^{144}Nd$ composition with a Thermo Scientific Neptune Plus multi-collector inductively coupled plasma mass spectrometer at the Institut für Mineralogie (Westfälische Wilhelms-Universität Münster). Results are reported in εNd notation (DePaolo and Wasserburg, 1976) with errors as 2σ standard deviations.

4.3.2 Apatite Sm-Nd isotope analysis

The single-grain analyses were run on the same apatites as used by Hülscher et al. (2021); information about sample preparation and depositional ages can be found there. Nd isotope analyses were carried out at the Geochronology and Tracers Facility of the British Geological Survey (Keyworth, UK) using a Thermo Scientific Neptune Plus MC-ICP-MS coupled to a New Wave Research UP193UC Excimer laser ablation system. For neodymium isotope analysis, $^{142}Ce+^{142}Nd$, ^{143}Nd, $^{144}Nd+^{144}Sm$, ^{145}Nd, ^{146}Nd, ^{147}Sm, ^{149}Sm, ^{150}Nd and ^{151}Eu were measured simultaneously during static 30 second ablation analyses. Apatites were analyzed with a 35-50 µm laser spot size due to the small grain-size. Correction for ^{144}Sm on the ^{144}Nd peak was carried out using the method of Yang et al. (2014). Madagascar apatite was used as the primary reference material for laser-ablation analysis. Data reduction was carried out using the Iolite data-reduction package (Paton et al., 2011) (see the supplementary material for further information).

4.4 Results

4.4.1 Nd isotopic composition of clay-sized fraction

Thirty samples were analyzed for their Nd isotopic composition, six of them twice with different protocols during preparation (see supplementary material). The replicated analyses agree within 2σ uncertainties. The dataset shows only little variation around -9.67 (± 0.54; Fig. 4.2) in the 25 samples from ~27 to 19 Ma. In the 5 samples younger 19 Ma, the εNd values became more positive (-9.12 ± 0.52). We applied a Monte-Carlo method for robust estimation of the difference in mean εNd values between the two subgroups (>19 Ma and <19 Ma). The results indicate that the samples <19 Ma are significantly higher (95% confidence level: $\delta\mu \in [0.5520, 0.5536]_{95\%CI}$) in their mean εNd value than the samples >19 Ma.

Table 4.1: Results of the apatite Sm-Nd analysis and their statistical analysis of the different subgroups

		LM	HM	UM	IM
Number of grains		127	173	10	96
εNd	Median	-4.88	-1.95	-7.18	-5.85
	5th Percentile	-10.46	-9.37	-11.24	-10.39
	95th Percentile	2.57	3.00	1.03	0.64
$^{147}Sm/^{144}Nd$	Median	0.28100	0.27044	0.23302	0.26414
	5th Percentile	0.21279	0.169758	0.132629	0.110525
	95th Percentile	0.44667	0.413336	0.331158	0.380225
KS-Test p-values εNd distribution	LM	-	0%	27%	11%
	HM	-	-	0%	0%
	UM	-	-	-	56%

4.4.2 Apatite Sm-Nd isotopic composition

406 detrital apatite grains were analyzed for their $^{147}Sm/^{144}Nd$ and $^{143}Nd/^{144}Nd$ isotopic composition. Apatites were grouped based on their trace-element geochemistry (Hülscher et al., 2021) into four source rocks: mafic igneous rocks (IM); low- and medium-grade metamorphic (<upper amphibolite-facies) (LM); high-grade metamorphic rocks (HM); and ultramafic rocks (UM) following O'Sullivan et al. (2020). Note that the apatites from S-type granitoids and HM sources, as differentiated by O'Sullivan et al. (2020), are grouped together in this study as HM apatites for simplicity. εNd values are the highest in the HM apatite group (Tab. 4.1, Figs. 4.2, A3.2). Our dataset is biased towards REE-rich apatites (with high Sm and Nd contents). LM apatites are depleted in REEs (O'Sullivan et al., 2020), and are

underrepresented in our Nd isotope dataset (31 %) compared to the trace-element dataset (47 %) of Hülscher et al. (2021).

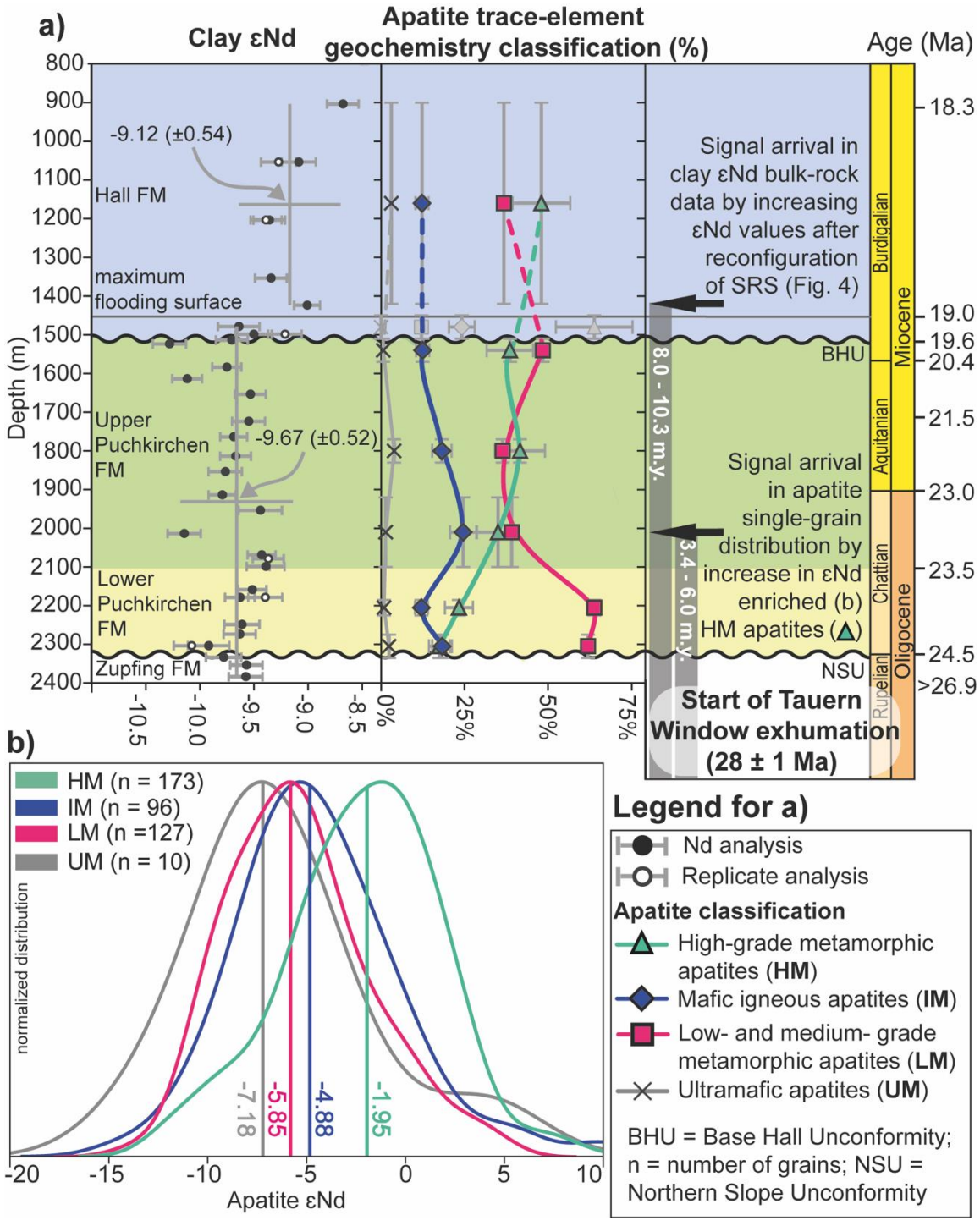

Figure 4.2: Section of Well H (a) (age-depth model from Hülscher et al. (2019)) showing results from the clay-sized Nd isotopic composition analysis, trends in the apatite classification (Hülscher et al., 2021) and total signal lag times of the grain-size fractions. Apatite samples between 19.6 and 19.0 Ma disregarded from trend because fission track and foraminiferal analysis indicate sediment recycling (Grunert et al., 2013; Hülscher et al., 2021). b) Kernel density estimation plot of the apatite single-grain εNd values separated in subgroups with their median shown as vertical lines.

A Kolgomorov–Smirnov (K-S) Test (Hodges, 1958) was performed to test whether the εNd single-grain distributions of differently classified apatites result from random sampling of the same parent population or are significantly different. P-values of the K-S Test of the HM apatites are <0.01% when compared to the remaining apatite groups, indicating a significantly different εNd distribution of the HM group, in contrast to the other apatite groups which show similar εNd distributions (Tab. 4.1). The $^{147}Sm/^{144}Nd$ ratios are similar between the different apatite groups (Tab. 4.1).

4.5 Discussion

Our data show a striking contrast in provenance-change recording between the single-grain and the bulk-rock analysis. Hülscher et al. (2021) interpreted the changing apatite trace-element geochemistry and U-Pb thermochronology at 23.3 ± 0.3 Ma as a provenance change triggered by an exposure of a new Upper Austroalpine nappe following the onset of Tauern Window exhumation (Fig. 4.2). The significantly increased εNd values in the HM apatites compared to the IM, LM and UM grains show that the HM apatite source rocks are more positive in their εNd values (Tab. 4.1, Figs. 4.2, A3.2). This εNd increased source became a significant contributor (~40% HM apatites) for the sand-sized sediment in the Upper Austrian NAFB (Hülscher et al., 2021). The total signal-lag time of the provenance change in the apatite single-grain distributions in response to the early Tauern Window exhumation is 3.4 – 6.0 m.y. (Fig. 4.2).

In contrast, the consistent εNd values in the bulk-rock clay-sized fraction from ~27 to 19 Ma suggests a stable provenance in this interval (Fig. 4.2). Hence, the exposure of the new Upper Austroalpine source with increased εNd values was not recorded by the εNd values of the clay-sized fraction at 23.3 Ma. However, the significant increase in the εNd values of the clay-sized fraction after 19 Ma reflects the change in provenance that occurred 4 – 5.3 m.y. earlier in the sand-sized apatites (Fig. 4.2). The total signal-lag time of the Tauern Window exhumation in the clay-sized fraction is 8.0 – 10.3 m.y. The characteristics of the applied methods are responsible for the delayed provenance-change recording. Until 19 Ma, the Upper Austrian NAFB was partly source from a western Central Alpine SRS (Füchtbauer, 1964; Kuhlemann and Kempf, 2002), which was larger than the Eastern Alpine SRSs via the paleo-Inn and the Augenstein Formation (Fig. 4.3) (Winterberg, 2019). The changing εNd values in the clay-size fraction after the tectonically induced (Zweigel, 1998) cut off of the western SRS at 19 Ma indicate that the western SRS represented a significant source for clay-sized material in the Upper Austrian NAFB. The input from the small (~3,125 km^2; Favaro et al. (2017)) source area

with increased εNd values above the future Tauern Window was diluted in the SRSs by the overwhelming contribution of the remaining sources. After 19 Ma, the relative proportion of the future Tauern Window in the source area increased from ~3% to ~8%, enabling the bulk-rock clay-sized fraction to record the changing provenance (Fig. 4.3).

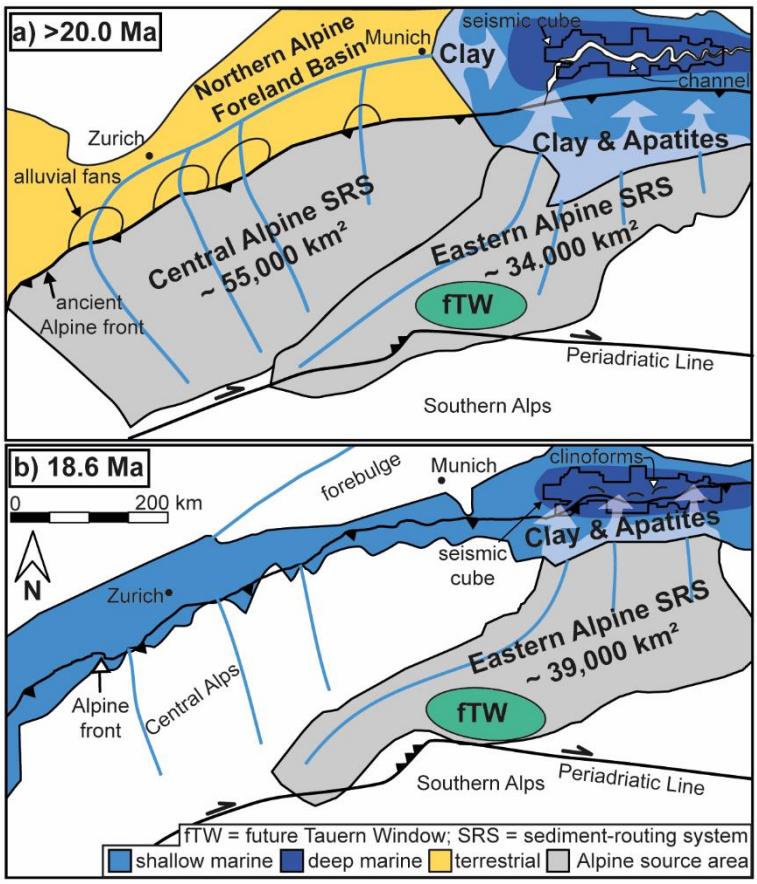

Figure 4.3: Paleogeographic reconstruction of the Rupelian to Burdigalian SRSs in the Alps following Winterberg (2019). From 28 to 19 Ma (a) an eastward sediment routing persisted in the NAFB. This changed to a dominantly northward sediment transport after the flooding of the NAFB at 19 Ma (b). The Central Alpine SRS was cut off from the Upper Austrian NAFB what significantly reduced the sediment-source area.

The 4 – 5 m.y. earlier provenance change in the apatite single-grain distribution is due to the tendency of single-grain methods to highlight rapidly eroding mountain areas with high mineral fertility (Malusà et al., 2017) and the tendency of coarser grain-size fractions to be biased towards more proximal sources (Gemignani et al., 2019; Hülscher et al., 2018). Therefore, the proximal, rapidly eroding Upper Austroalpine Nappes above the future Tauern Window (Hülscher et al., 2021) represented a significant source for the Upper Austrian NAFB sand-sized sediment.

4.6 Conclusion

Analysis of sand-sized single-grains and clay-sized bulk-rock revealed time-delayed recording of provenance changes in Rupelian to Burdigalian sediments of the Upper Austrian NAFB. Whereas the sand-sized apatites record the exhumation and erosion of the small source area above the future Tauern Window in the Eastern Alps from 23.3 Ma onward, the clay-sized sediment fraction shows no significant provenance change until 19 Ma. The changing clay-size sediment provenance at 19 Ma is related to the cut off of the Central Alpine SRS and the reduction of the Upper Austrian NAFB source area. This selective recording of the tectonic forcing in the hinterland in the sediment archive is controlled by the dilution and concentration of the signal in the bulk-rock clay-size fraction and single-grain analysis, respectively.

By quantifying total signal-lag times of changes in sedimentary provenance with different methods, valuable information about the underlying perturbation is gained as the different methods emphasize or de-emphasize different aspects of the same process. In our study, the small area of the newly exposed source rocks is likely to explain the delay of the area-averaged εNd signal in the clay-sized sediment fraction. However, a process affecting large parts of a source area is likely to contemporaneously change the single-grain distribution and bulk-rock results in the sedimentary archive. Such a contemporaneous provenance change has been described in response to Holocene climate change (Clift and Giosan, 2014; Fildani et al., 2018). Obtaining information about the areal extent of a perturbation affecting a SRS by provenance analysis holds great potential to gain insights about the forcing mechanism of environmental changes in ancient SRSs.

Chapter 5: Conclusion

5.1 Conceptual research questions on the sediment-routing system approach

This study has shown that two of three tectonic events in the Oligocene/Miocene Alps – the exhumation of the Lepontine Dome in the Central Alps starting at ~32 Ma (Schlunegger and Castelltort, 2016); the exhumation of the Tauern Window in the Eastern Alps starting at ~28 Ma (Favaro et al., 2015); and the redeposition of the Augenstein Formation into the NAFB starting at ~21 Ma (Frisch et al., 2001) – can be detected by applying different proxies to the sedimentary sections in the Upper Austrian NAFB. The early exhumation of the Tauern Window is by far the best recognizable tectonic event in the provenance and thermochronological studies presented in Chapter 3 and 4. However, the total signal-lag times (Tofelde et al., 2021) related to the Tauern Window exhumation differ significantly between different methods.

As proposed in Chapter 3, the doubling of the sediment-discharge rates from the Eastern Alps at 29 Ma (Kuhlemann et al., 2001) can be regarded as the response to the early exhumation of the Tauern Window. This implies a response of the rates to the tectonically driven exhumation (Fig. 5.1) well below the uncertainties of the timing of the tectonic forcing (± 1 m.y.) and the stratigraphic model (± 0.5 m.y.) of Kuhlemann et al. (2001). In line with this interpretation, numerical modeling studies predict an immediate increase in sediment flux to the foreland when uplift rates in the hinterland increase (Li et al., 2018; Sharman et al., 2019). In Chapter 3, the decreasing AFT lag times from Oligocene to late Miocene deposits are interpreted as the surface expression of the early exhumation of the Tauern Window (Fig. 5.1). Following this interpretation, this sedimentary proxy arrives in the sedimentary archive with a total signal lag time of 2.7 to 5.1 m.y. as the onset of the decreasing AFT lag times was described at 24.1 (± 0.2) Ma. The total signal-lag time of this method is controlled by the exhumation rate and the paleo-geothermal gradient in the hinterland (Malusà and Fitzgerald, 2019). The overlying rock units containing the apatites that record the pre-28 Ma exhumation period must have been removed first, before the rapidly cooled rocks became exposed and eroded.

The provenance tools applied in Chapters 3 and 4 – apatite single grain analysis and Nd analysis of clay-sized bulk-rock samples – revealed a significantly different total signal lag time. Whereas the apatite single-grain distribution changed 3.4 – 6 m.y. after the onset of the Tauern Window exhumation, the clay-sized bulk-rock analysis revealed the related provenance

change 8 – 10.3 m.y. after the onset (Fig. 5.1). This delay in signal recording is controlled by the characteristics of the applied methods. Whereas bulk rock methods integrate over the entire sediment-routing system (Tofelde et al., 2021), the single-grain method delivers point-source information from their source rocks (von Eynatten and Dunkl, 2012). In combination with the tendency of both methods to highlight (Malusà et al., 2017) or dim (Wittmann et al., 2016) extreme values in erosion rates or mineral fertility, the signal is diluted or amplified over the course of the SRS.

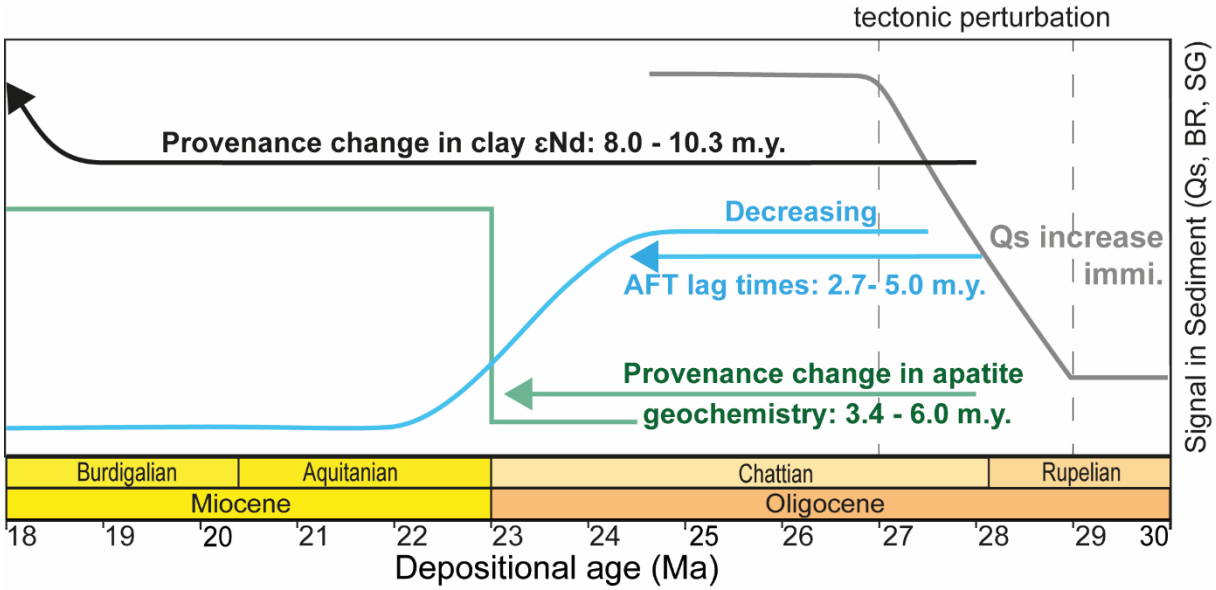

Figure 5.1: Schematic comparison of the different signal-arrival times for different applied methods in response to the Tauern Window exhumation from 28 ± 1 Ma onward. Sediment-discharge rates (Qs) (Kuhlemann et al., 2001) reacted immediately after the onset of the exhumation. The single-grain (SG) and bulk-rock (BR) methods needed several m.y. to mirror the changing conditions in the sediment-routing system. The calculated signal-lag time included the uncertainties on the stratigraphic model and on the onset of the tectonic perturbation.

The second event that can be found in the Upper Austrian NAFB is the redeposition of the Augenstein Formation from 21 Ma onward (Frisch et al., 2001). An immediate response has been recognized by changes in the apatite single-grain thermochronology and geochemistry of the southern slope samples in Chapter 3. The AFT results also reveal a contribution from the Augenstein Formation into the Hall Formation – the Variscan and non-Variscan subgroups differ significantly in their AFT ages – in the line with interpretation from Chapter 2. There, the four-fold increase in sediment-accumulation rates (SARs) is related to the redeposition of the Augenstein Formation. The redeposition is therefore first expressed in the provenance proxies applied to the sediments on the southern slope (Chapter 3) and with a delay of 2 m.y. in the SARs. This is in contrast to the order of signal arrivals in response to the Tauern Window exhumation, where the sediment-discharge rates first increased and then the provenance

changed (Chapter 3). However, no SARs have been quantified on the southern basin slope which likely explains this difference in signal arrival times.

Remarkably, the exhumation of the Lepontine Dome – the largest tectonic exhumation event during our time of interest in the Alps in terms of eroded sediment volume (Kuhlemann et al., 2001) – neither led to an increase in the SARs (Chapter 2) nor changed the sand-sized sediment provenance (Chapter 3) in the Upper Austrian NAFB. This is even more remarkable as the signal of the exhumation is detected in the proximal Swiss NAFB (Schlunegger and Castelltort, 2016; Spiegel et al., 2004; von Eynatten et al., 1999) as well as in the distal German NAFB close to Munich in provenance analysis and SARs (Füchtbauer, 1964; Zweigel, 1998). There, a delta system received sediment from the Central Alps during the deposition of the Lower Freshwater Molasse (Kuhlemann and Kempf, 2002) and a direct connection via a submarine canyon existed to the Puchkirchen channel (De Ruig and Hubbard, 2006; Zweigel, 1998). Either the Lepontine Dome exhumation signal was diluted by the material shed from the Eastern Alps and – therefore – was not recognized in the sand-sized provenance analysis of the Puchkirchen channel system, or the apatites were stored on the shelf and were never transported into the deeper parts of the Upper Austrian NAFB. However, in the Nd isotopic composition of the clay-sized sediments, an influence of the Central Alpine source is recognizable (Chapter 4). The isotopic composition changed after this source was cut off from the Upper Austrian NAFB and therefore, the western SRS must have contributed to the clay-sized fraction before the cut-off.

This thesis has quantified the total signal-lag times of different methods in response to a tectonic environmental perturbation. Whereas the sediment-discharge rates responded immediately to the tectonic exhumation of the Tauern Window, the AFT results and the sand-sized provenance datasets mirror the changed conditions in the hinterland after several million years. This delayed signal arrival in the sediment archive is related to the signal-onset time (*sensu* Tofelde et al. (2021)) as the measurable changes in the hinterland must first be exhumed to the surface before they can be eroded and transported into the sink. The great unknown in this context is the signal-transfer time (*sensu* Tofelde et al. (2021)), the period of time the signal needs to travel from the source to the sink. Based on the available datasets, a quantification is not possible for the studied signals. However, research from other regions suggests that signal-transfer times play a subordinated role in total signal lag times (Bernet et al., 2004; Clift and Giosan, 2014; Fildani et al., 2018), especially in geological deep-time.

The described difference between bulk-rock and single-grain provenance analysis (Chapter 4) holds great potential to further gain insights on the response of SRSs to environmental perturbations. In the presented case the combination of the provenance characterization by the bulk-rock and single-grain approach reveals information about the areal extent of the

perturbed area (Chapter 4). However, taking this idea even further, the characterization of the same sedimentary parameter (flux or provenance) of a sediment-routing system with different methods holds great potential. For example, the quantification of SARs and exhumation rates via low-temperature thermochronology may reveal insights about the underlying exhumation processes, whether they are erosional or tectonically driven.

5.2 Implications for the Evolution of the Eastern Alps

As outlined in Chapter 1, the results of this thesis have also major implications for ongoing debates about the tectonic evolution of the Eastern Alps. In Chapter 2, the newly acquired stratigraphic results were used to constrain the basin evolution. The Puchkirchen Group was deposited between 26.9 and 19.6 Ma and is overlain by the Hall Formation with sedimentation ages between 19.6 and 18.1 Ma. The two regional unconformities in the basin, the NSU and BHU, have been dated to 28.1-26.9 Ma and 19.6 Ma, respectively. Furthermore, the biostratigraphic results highlight the complexity of such a dynamic environment as the Oligocene/early Miocene Upper Austrian NAFB for stratigraphic interpretations. The Puchkirchen channel created a spatially and temporally variable environment, which controlled the appearances of benthonic index taxa, hampering the attempt to correlate stratigraphic units even within the Upper Austrian NAFB.

Comparing the results from Chapter 2 with the evolutionary time steps in the German and Swiss NAFB highlights the completely different basin evolution. Whereas the basin in Upper Austria deepened around 28.1 – 26.9 Ma, the NAFB in Switzerland turned at the same time from an underfilled to filled basin; the transition marks the onset of the deposition of the Lower Freshwater Molasse (Sinclair, 1997). Several authors have pointed out that this temporal difference in basin evolution is related to a difference in slab geometry underneath the Eastern and Central Alps (Garefalakis and Schlunegger, 2019; Handy et al., 2015; Schlunegger and Kissling, 2015). Whereas the Central Alpine slab broke off around ~32 Ma, causing the transition from flysch-type to molasse-type sedimentation (Schlunegger and Castelltort, 2016; Schlunegger and Kissling, 2015), the Eastern Alpine slab broke off partly and the rest rolled back and dragged the Upper Austrian NAFB down, enabling an ongoing flysch-type sedimentation (Handy et al., 2021; Handy et al., 2015). Furthermore, previous studies have pointed out that the change in sediment transport direction found in Chapter 2 at 19 Ma was caused by a slab-unloading underneath the Eastern Alps (Garefalakis and Schlunegger, 2019; Handy et al., 2021; Handy et al., 2015). If such a break-off underneath the Eastern Alps occurred around 20 Ma, a significant part of the estimated 260 km subducted continental

lithosphere since 35 Ma (Le Breton et al., 2021) would have been removed. The length of the present-day detached European slab underneath the Eastern Alps (300-500 km) (Handy et al., 2021) stands in conflict to this idea because it would require significantly more subduction to compensate the slab length removed by the breakoff. Furthermore, the unloading related to the potential slab breakoff around 20 Ma should have led to a significant surface uplift not only in the basin (Neumeister, 2021; Zweigel, 1998) but also in the Eastern Alpine hinterland. As shown in Chapter 3 such a hinterland uplift has not been detected. Apart from the nowadays exposed Tauern Window, the Eastern Alps were already in Oligocene/Miocene times a slowly (<0.1 mm/a) exhuming mountain range.

In Chapter 3, the sedimentary products of the surface response to the early exhumation of the Tauern Window have been described in the proximal foreland deposits. This early exhumation has caused an erosion of 3.3 – 4.7 km (0.3-0.6 mm/a) of Upper Austroalpine rocks above the future Tauern Window until 20 Ma, which is in good agreement with the sediment discharge rates from the same period (Kuhlemann et al., 2001). The early start of the exhumation and its occurrence only north of the Adriatic Indenter, highlights the importance of the indentation (Ratschbacher et al., 1991) also in this early period of Tauern Window exhumation. From 23-21 Ma, onward the exhumation rates of the Tauern Window significantly increased (1.5-2 mm/a; Frisch et al. (2000)) which is due to the beginning of lateral escape (Scharf et al., 2013a).

Chapter 6: Outlook

The data and interpretation of this thesis brought up new questions and ideas which might be worth to consider when thinking about future research projects. In the following a few of them will be pointed out, again ordered in ideas of interest for the entire SRS community and of more regional interest.

- As outlined above, the signal from the Lepontine Dome exhumation was not found in the provenance dataset of the sand-sized apatites. To validate this interpretation, a U-Pb dating of detrital zircon from the Upper Austrian NAFB could be applied. The provenance change related to the surface exposure of the Lepontine Dome has been recently described by a study in the proximal Swiss NAFB as an significant increase of Permian detrital U-Pb zircon ages in sediments younger than 22 Ma (Anfinson et al., 2020). A zircon U-Pb study on Upper Austrian NAFB deposits between 23 and 19 Ma could reveal such a change in zircon provenance. Such a dataset could potentially help to quantify signal-progradation rates.
- The findings of Chapter 4 about the differences in provenance recording between bulk-rock and single-grain methods hold great potential to further enhance our understanding about signal propagation in SRSs and their underlying perturbations. To further investigate this idea, a numerical modelling approach should be chosen. This should be accompanied by a provenance study of a climatic perturbation in geological deep-time that includes a single-grain and a bulk-rock method. Taken together these studies could help to better understand the delay controlling mechanism.
- Researchers in the NAFB would benefit greatly from a uniform basin-wide stratigraphic framework. Attempts to establish such a framework have been made in the past (Berger et al., 2005a; Berger et al., 2005b; Kuhlemann and Kempf, 2002) but need to be updated and expanded. To succeed, such an attempt would require stratigraphic reanalysis of the deposits on the Munich delta and the Inn valley with absolute age dating.
- What were the source rocks of the Augenstein Formation? In Chapter 3 some information has been found in the southern slope samples, but a comprehensive picture is still missing. Such an attempt should include zircon U-Pb dating and apatite helium dating. These results could further constrain the position of the drainage divide in Oligocene times, forming an important indicator of the shape of the Eastern Alpine orogenic wedge.

- How did the Eastern Alpine drainage network react to the lateral escape from 23-21 Ma onward? The location of the drainage-divide for the paleo-Inn catchment is now quite well defined for the time from 28 Ma onward (Chapter 3) but the drainage configuration further to the east (east of the Katschberg normal fault) is still not well investigated. This study should include a comprehensive provenance analysis of the intramountain basins in the eastern Eastern Alps.
- When was the Adamello Pluton cut-off from the paleo-Inn drainage network? The erosional products of the Adamello Pluton can be found in the NAFB from the Oligocene (Dunkl et al., 2009) until ~9 Ma (Brügel et al., 2000) but today Adamello is drained towards the south. A study which applies U-Pb dating of detrital zircons on southern and northern foreland depositions which are younger than 9 Ma has the potential to reveal when this drainage reorganization happened. The study will have an important impact onto our understanding of the Eastern Alps as an orogenic wedge and whether its evolution was driven by tectonic or climatic processes.

Bibliography

Agnini, C., Fornaciari, E., Raffi, I., Catanzariti, R., Pälike, H., Backman, J., and Rio, D., 2014, Biozonation and biochronology of Paleogene calcareous nannofossils from low and middle latitudes: Newsletters on Stratigraphy, v. 47, no. 2, p. 131-181.

Allen, P. A., 2008, From landscapes into geological history: Nature, v. 451, no. 7176, p. 274-276.

Amos, K. J., Peakall, J., Bradbury, P. W., Roberts, M., Keevil, G., and Gupta, S., 2010, The influence of bend amplitude and planform morphology on flow and sedimentation in submarine channels: Marine and Petroleum Geology, v. 27, no. 7, p. 1431-1447.

Anfinson, O. A., Stockli, D. F., Miller, J. C., Möller, A., and Schlunegger, F., 2020, Tectonic exhumation of the Central Alps recorded by detrital zircon in the Molasse Basin, Switzerland: Solid Earth, v. 11, no. 6, p. 2197-2220.

Aubry, M.-P., 1984, Handbook of Cenozoic calcareous nannoplankton, Micropaleontology Press, American Museum of Natural History.

-, 1988, Handbook of Cenozoic Calcareous Nannoplankton, book 2, Ortholithae (Holococcoliths, Ceratoliths, Ortholiths and Other): Am. Mus. Nat. Hist. Micropaleontol. Press, New York, v. 1279.

-, 1989, Handbook of Cenozoic Calcareous Nannoplankton: Ortholithae (Pentaliths, and Others); Heliolithae (Fasciculiths, Sphenoliths and Others), Micropaleontology Press.

-, 1999, Handbook of Cenozoic Calcareous Nannoplankton: Book 5: Heliolithae (Zygoliths and Rhabdoliths), Micropaleontology Press, the American Museum of Natural History.

-, 2013, Cenozoic Coccolithophores: Braarudosphaerales, Micropaleontology Press.

Backman, J., Raffi, I., Rio, D., Fornaciari, E., and Pälike, H., 2012, Biozonation and biochronology of Miocene through Pleistocene calcareous nannofossils from low and middle latitudes: Newsletters on Stratigraphy, v. 45, no. 3, p. 221-244.

Beaumont, C., 1981, Foreland basins: Geophysical Journal International, v. 65, no. 2, p. 291-329.

Behrmann, J. H., 1988, Crustal-scale extension in a convergent orogen: the Sterzing-Steinach mylomte zone in the Eastern Alps: Geodinamica Acta, v. 2, no. 2, p. 63-73.

Belousova, E., Griffin, W., O'Reilly, S., and Fisher, N., 2002, Apatite as an indicator mineral for mineral exploration: trace-element compositions and their relationship to host rock type: Journal of Geochemical Exploration, v. 76, no. 1, p. 45-69.

Belousova, E., Walters, S., Griffin, W., and O'Reilly, S., 2001, Trace-element signatures of apatites in granitoids from the Mt Isa Inlier, northwestern Queensland: Australian Journal of Earth Sciences, v. 48, no. 4, p. 603-619.

Berger, J. P., Reichenbacher, B., Becker, D., Grimm, M., Grimm, K., Picot, L., Storni, A., Pirkenseer, C., Derer, C., and Schaefer, A., 2005a, Paleogeography of the Upper Rhine Graben (URG) and the Swiss Molasse Basin (SMB) from Eocene to Pliocene: International Journal of Earth Sciences, v. 94, no. 4, p. 697-710.

Berger, J. P., Reichenbacher, B., Becker, D., Grimm, M., Grimm, K., Picot, L., Storni, A., Pirkenseer, C., and Schaefer, A., 2005b, Eocene-Pliocene time scale and stratigraphy of the Upper Rhine Graben (URG) and the Swiss Molasse Basin (SMB): International Journal of Earth Sciences, v. 94, no. 4, p. 711-731.

Bernet, M., 2019, Exhumation studies of mountain belts based on detrital fission-track analysis on sand and sandstones, Fission-Track Thermochronology and its Application to Geology, Springer, p. 269-277.

Bernet, M., Brandon, M., Garver, J., Balestieri, M., Ventura, B., and Zattin, M., 2009, Exhuming the Alps through time: Clues from detrital zircon fission-track thermochronology: Basin Research, v. 21, no. 6, p. 781-798.

Bernet, M., Brandon, M. T., Garver, J. I., and Molitor, B. R., 2004, Fundamentals of detrital zircon fission-track analysis for provenance and exhumation studies with examples from the European Alps: Geological Society of America Special Papers, v. 378, p. 25-36.

Bernhard, F., Klötzli, U., Thöni, M., and Hoinkes, G., 1996, Age, origin and geodynamic significance of a polymetamorphic felsic intrusion in the Ötztal Crystalline Basement, Tirol, Austria: Mineralogy and Petrology, v. 58, no. 3-4, p. 171-196.

Bernhardt, A., Stright, L., and Lowe, D. R., 2012, Channelized debris-flow deposits and their impact on turbidity currents: The Puchkirchen axial channel belt in the Austrian Molasse Basin: Sedimentology, v. 59, no. 7, p. 2042-2070.

Bertrand, A., Rosenberg, C. L., Rabaute, A., Herman, F., and Fügenschuh, B., 2017, Exhumation mechanisms of the Tauern Window (Eastern Alps) inferred from apatite and zircon fission track thermochronology: Tectonics, v. 36, no. 2, p. 207-228.

Blanckenburg, F. v., Früh-Green, G., Diethelm, K., and Stille, P., 1992, Nd-, Sr-, O-isotopic and chemical evidence for a two-stage contamination history of mantle magma in the Central-Alpine Bergell intrusion: Contributions to Mineralogy and Petrology, v. 110, no. 1, p. 33-45.

Blanckenburg, F. v., Villa, I., Baur, H., Morteani, G., and Steiger, R., 1989, Time calibration of a PT-path from the Western Tauern Window, Eastern Alps: the problem of closure temperatures: Contributions to Mineralogy and Petrology, v. 101, no. 1, p. 1-11.

Blum, M., Rogers, K., Gleason, J., Najman, Y., Cruz, J., and Fox, L., 2018, Allogenic and autogenic signals in the stratigraphic record of the deep-sea Bengal Fan: Scientific Reports, v. 8, no. 1, p. 1-13.

Boote, D., Sachsenhofer, R., Tari, G., and Arbouille, D., 2018, Petroleum provinces of the Paratethyan region: Journal of Petroleum Geology, v. 41, no. 3, p. 247-297.

Borsi, S., 1978, New geopetrologic and radiometric data on the Alpine history of the Austridic continental margin south of the Tauern Window (Eastern Alps), Società cooperativa tipografica.

Borsi, S., Del Moro, A., Sassi, F., and Zirpoli, G., 1979, On the age of the Vedrette di Ries (Rieserferner) massif and its geodynamic significance: Geologische Rundschau, v. 68, no. 1, p. 41-60.

Bousquet, R., Oberhansli, R., Schmid, S., Berger, A., Wiederkeher, M., Robert, C., Moller, A., Rosenberg, C. L., Zeilinger, G., and Molli, G., 2012, Metamorphic framework of the Alps-Carte metamorphique des Alpes CCGM/CGMW, CCGM/CGMW.

Bown, P., 1998, Calcareous nannofossil biostratigraphy, Chapman and Hall; Kluwer Academic.

Brügel, A., 1998, Provenances of Alluvial Conglomerates from the Eastalpine Foreland: Oligo-Miocene Denudation History and Drainage Evolution of the Eastern Alps; 10 Tabellen.

Brügel, A., Dunkl, I., Frisch, W., Kuhlemann, J., and Balogh, K., 2000, The record of Periadriatic volcanism in the Eastern Alpine Molasse zone and its palaeogeographic implications: Terra Nova, v. 12, no. 1, p. 42-47.

-, 2003, Geochemistry and geochronology of gneiss pebbles from foreland molasse conglomerates: geodynamic and paleogeographic implications for the Oligo-Miocene evolution of the Eastern Alps: The Journal of geology, v. 111, no. 5, p. 543-563.

Cahuzac, B., and Poignant, A., 1997, Essai de biozonation de l'Oligo-Miocène dans les bassins européens à l'aide des grands foraminifères néritiques: Bulletin de la Société géologique de France, v. 168, no. 2, p. 155-169.

Caracciolo, L., 2020, Sediment generation and sediment routing systems from a quantitative provenance analysis perspective: Review, application and future development: Earth-Science Reviews, p. 103226.

Carlson, W. D., Donelick, R. A., and Ketcham, R. A., 1999, Variability of apatite fission-track annealing kinetics: I. Experimental results: American mineralogist, v. 84, no. 9, p. 1213-1223.

Carter, A., 2019, Thermochronology on sand and sandstones for stratigraphic and provenance studies, Fission-Track Thermochronology and its Application to Geology, Springer, p. 259-268.

Carvajal, C., and Steel, R., 2011, Source-to-sink sediment volumes within a tectono-stratigraphic model for a Laramide shelf-to-deep-water basin: Methods and results: Tectonics of sedimentary basins: Recent advances, p. 131-151.

Castelltort, S., and Van Den Driessche, J., 2003, How plausible are high-frequency sediment supply-driven cycles in the stratigraphic record?: Sedimentary geology, v. 157, no. 1-2, p. 3-13.

Chamberlain, K. R., and Bowring, S. A., 2001, Apatite–feldspar U–Pb thermochronometer: a reliable, mid-range (~ 450° C), diffusion-controlled system: Chemical Geology, v. 172, no. 1-2, p. 173-200.

Chew, D., O'Sullivan, G., Caracciolo, L., Mark, C., and Tyrrell, S., 2020, Sourcing the sand: Accessory mineral fertility, analytical and other biases in detrital U-Pb provenance analysis: Earth-Science Reviews, v. 202, p. 103093.

Chew, D., Petrus, J., and Kamber, B., 2014, U–Pb LA–ICPMS dating using accessory mineral standards with variable common Pb: Chemical Geology, v. 363, p. 185-199.

Chew, D., Sylvester, P. J., and Tubrett, M. N., 2011, U–Pb and Th–Pb dating of apatite by LA-ICPMS: Chemical Geology, v. 280, no. 1-2, p. 200-216.
Christensen, J. N., Selverstone, J., Rosenfeld, J. L., and DePaolo, D. J., 1994, Correlation by Rb-Sr geochronology of garnet growth histories from different structural levels within the Tauern Window, Eastern Alps: Contributions to Mineralogy and Petrology, v. 118, no. 1, p. 1-12.
Cicha, I., Rogl, F., and Rupp, C., 1998, Oligocene-Miocene foraminifera of the central Paratethys: Abh./Senckenberg. naturforschende Ges.
Cliff, R., Droop, G., and Rex, D., 1985, Alpine metamorphism in the south-east Tauern Window, Austria: 2. Rates of heating, cooling and uplift: Journal of metamorphic Geology, v. 3, no. 4, p. 403-415.
Clift, P., and Giosan, L., 2014, Sediment fluxes and buffering in the post-glacial Indus Basin: Basin Research, v. 26, no. 3, p. 369-386.
Clift, P. D., 2006, Controls on the erosion of Cenozoic Asia and the flux of clastic sediment to the ocean: Earth and Planetary Science Letters, v. 241, no. 3-4, p. 571-580.
Clift, P. D., Hodges, K. V., Heslop, D., Hannigan, R., Van Long, H., and Calves, G., 2008, Correlation of Himalayan exhumation rates and Asian monsoon intensity: Nature geoscience, v. 1, no. 12, p. 875-880.
Ćorić, S., and Spezzaferri, S., 2009, ZIEG - 1: Mikropaläontologische und biostratigraphische Auswertung (750m – 1500m): RAG Internal Report.
Covault, J. A., Hubbard, S. M., Graham, S. A., Hinsch, R., and Linzer, H.-G., 2009, Turbidite-reservoir architecture in complex foredeep-margin and wedge-top depocenters, Tertiary Molasse foreland basin system, Austria: Marine and Petroleum Geology, v. 26, no. 3, p. 379-396.
Cramer, B., Toggweiler, J., Wright, J., Katz, M., and Miller, K., 2009, Ocean overturning since the Late Cretaceous: Inferences from a new benthic foraminiferal isotope compilation: Paleoceanography, v. 24, no. 4.
De Ruig, M. J., and Hubbard, S. M., 2006, Seismic facies and reservoir characteristics of a deep-marine channel belt in the Molasse foreland basin, Puchkirchen Formation, Austria: AAPG bulletin, v. 90, no. 5, p. 735-752.
DeCelles, P. G., and Giles, K. A., 1996, Foreland basin systems: Basin research, v. 8, no. 2, p. 105-123.
Del Moro, A., Puxeddu, M., Di Brozolo, F. R., and Villa, I., 1982, Rb-Sr and K-Ar ages on minerals at temperatures of 300–400 C from deep wells in the Larderello geothermal field (Italy): Contributions to Mineralogy and Petrology, v. 81, no. 4, p. 340-349.
DePaolo, D., and Wasserburg, G., 1976, Nd isotopic variations and petrogenetic models: Geophysical Research Letters, v. 3, no. 5, p. 249-252.
Duller, R. A., Armitage, J. J., Manners, H. R., Grimes, S., and Jones, T. D., 2019, Delayed sedimentary response to abrupt climate change at the Paleocene-Eocene boundary, northern Spain: Geology, v. 47, no. 2, p. 159-162.
Dunkl, I., Frisch, W., and Grundmann, G., 2003, Zircon fission track thermochronology of the southeastern part of the Tauern Window and the adjacent Austroalpine margin, Eastern Alps: Eclogae Geologicae Helvetiae, v. 96, no. 2, p. 209-218.
Dunkl, I., Frisch, W., Kuhlemann, J., and Brügel, A., 2009, Pebble population dating as an additional tool for provenance studies-examples from the Eastern Alps: Geological Society, London, Special Publications, v. 324, no. 1, p. 125-140.
Favaro, S., Handy, M. R., Scharf, A., and Schuster, R., 2017, Changing patterns of exhumation and denudation in front of an advancing crustal indenter, Tauern Window (Eastern Alps): Tectonics, v. 36, no. 6, p. 1053-1071.
Favaro, S., Schuster, R., Handy, M. R., Scharf, A., and Pestal, G., 2015, Transition from orogen-perpendicular to orogen-parallel exhumation and cooling during crustal indentation—key constraints from 147Sm/144Nd and 87Rb/87Sr geochronology (Tauern Window, Alps): Tectonophysics, v. 665, p. 1-16.
Fildani, A., Hessler, A. M., Mason, C. C., McKay, M. P., and Stockli, D. F., 2018, Late Pleistocene glacial transitions in North America altered major river drainages, as revealed by deep-sea sediment: Scientific reports, v. 8, no. 1, p. 1-8.
Fildani, A., Normark, W. R., Kostic, S., and Parker, G., 2006, Channel formation by flow stripping: Large-scale scour features along the Monterey East Channel and their relation to sediment waves: Sedimentology, v. 53, no. 6, p. 1265-1287.

Foeken, J. P., Persano, C., Stuart, F. M., and Ter Voorde, M., 2007, Role of topography in isotherm perturbation: Apatite (U-Th)/He and fission track results from the Malta tunnel, Tauern Window, Austria: Tectonics, v. 26, no. 3.

Frisch, W., Dunkl, I., and Kuhlemann, J., 2000, Post-collisional orogen-parallel large-scale extension in the Eastern Alps: Tectonophysics, v. 327, no. 3, p. 239-265.

Frisch, W., Kuhlemann, J., Dunkl, I., and Brügel, A., 1998, Palinspastic reconstruction and topographic evolution of the Eastern Alps during late Tertiary tectonic extrusion: Tectonophysics, v. 297, no. 1, p. 1-15.

Frisch, W., Kuhlemann, J., Dunkl, I., and Székely, B., 2001, The Dachstein paleosurface and the Augenstein Formation in the Northern Calcareous Alps–a mosaic stone in the geomorphological evolution of the Eastern Alps: International Journal of Earth Sciences, v. 90, no. 3, p. 500-518.

Füchtbauer, H., 1964, Sedimentpetrographische Untersuchungen in der älteren Molasse nördlich der Alpen: Eclogae Geologicae Helvetiae, v. 57.

Fügenschuh, B., Mancktelow, N. S., and Schmid, S. S., 2012, Comment on Rosenberg and Garcia: estimating displacement along the Brenner Fault and orogen-parallel extension in the Eastern Alps, Int J Earth Sci (Geol Rundsch)(2011) 100: 1129–1145: International Journal of Earth Sciences, v. 101, no. 5, p. 1451-1455.

Fügenschuh, B., Mancktelow, N. S., and Seward, D., 2000, Cretaceous to Neogene cooling and exhumation history of the Oetztal-Stubai basement complex, eastern Alps: A structural and fission track study: Tectonics, v. 19, no. 5, p. 905-918.

Fügenschuh, B., Seward, D., and Mancktelow, N., 1997, Exhumation in a convergent orogen: the western Tauern window: Terra Nova, v. 9, no. 5-6, p. 213-217.

Galović, I., and Young, J., 2012, Revised taxonomy and stratigraphy of Middle Miocene calcareous nannofossils of the Paratethys: Micropaleontology, p. 305-334.

Ganss, O., 1977, Geologische Karte von Bayern 1: 25 000, Erläuterungen zum Blatt Nr. 8140 Prien a. Chiemsee und Blatt Nr. 8141 Traunstein: Bayerisches Geologisches Landesamt.

Garçon, M., Boyet, M., Carlson, R. W., Horan, M. F., Auclair, D., and Mock, T. D., 2018, Factors influencing the precision and accuracy of Nd isotope measurements by thermal ionization mass spectrometry: Chemical Geology, v. 476, p. 493-514.

Garefalakis, P., and Schlunegger, F., 2019, Tectonic processes, variations in sediment flux, and eustatic sea level recorded by the 20 Myr old Burdigalian transgression in the Swiss Molasse basin: Solid Earth, v. 10, no. 6, p. 2045-2072.

Garver, J. I., Brandon, M. T., Roden-Tice, M., and Kamp, P. J., 1999, Exhumation history of orogenic highlands determined by detrital fission-track thermochronology: Geological Society, London, Special Publications, v. 154, no. 1, p. 283-304.

Gemignani, L., Kuiper, K., Wijbrans, J., Sun, X., and Santato, A., 2019, Improving the precision of single grain mica 40Ar/39Ar-dating on smaller and younger muscovite grains: Application to provenance studies: Chemical Geology, v. 511, p. 100-111.

Genser, J., Cloetingh, S. A., and Neubauer, F., 2007, Late orogenic rebound and oblique Alpine convergence: New constraints from subsidence analysis of the Austrian Molasse basin: Global and Planetary Change, v. 58, no. 1, p. 214-223.

Genser, J., and Neubauer, F., 1989, Low angle normal faults at the eastern margin of the Tauern window (Eastern Alps): Mitteilungen der Österreichischen Geologischen Gesellschaft, v. 81, no. 1988, p. 233-243.

Gleadow, A., 1981, Fission-track dating methods: what are the real alternatives?: Nuclear Tracks, v. 5, no. 1-2, p. 3-14.

Glodny, J., Ring, U., Kühn, A., Gleissner, P., and Franz, G., 2005, Crystallization and very rapid exhumation of the youngest Alpine eclogites (Tauern Window, Eastern Alps) from Rb/Sr mineral assemblage analysis: Contributions to Mineralogy and Petrology, v. 149, no. 6, p. 699-712.

Govin, G., van der Beek, P., Najman, Y., Millar, I., Gemignani, L., Huyghe, P., Dupont-Nivet, G., Bernet, M., Mark, C., and Wijbrans, J., 2020, Early onset and late acceleration of rapid exhumation in the Namche Barwa syntaxis, eastern Himalaya: Geology, v. 48, no. 12, p. 1139-1143.

Gradstein, F., Ogg, J., Schmitz, M., and Ogg, G., 2012, The Geologic Time Scale 2012. 1176 pp: Amsrerdam: Elsevier.

Gross, D., Sachsenhofer, R., Bechtel, A., Gratzer, R., Grundtner, M. L., Linzer, H. G., Misch, D., Pytlak, L., and Scheucher, L., 2018, Petroleum systems in the Austrian sector of the North Alpine Foreland Basin: an overview: Journal of Petroleum Geology, v. 41, no. 3, p. 299-317.

Groß, P., Pleuger, J., Handy, M. R., Germer, M., and John, T., 2020, Evolving temperature field in a fossil subduction channel during the transition from subduction to collision (Tauern Window, Eastern Alps): Journal of Metamorphic Geology.

Grundmann, G., and Morteani, G., 1985, The young uplift and thermal history of the central Eastern Alps (Austria/Italy), evidence from apatite fission track ages: Jahrb. Geol. Bundesanst, v. 128, p. 197-216.

Grunert, P., Auer, G., Harzhauser, M., and Piller, W. E., 2015, Stratigraphic constraints for the upper Oligocene to lower Miocene Puchkirchen Group (North Alpine Foreland Basin, Central Paratethys): Newsletters on Stratigraphy, v. 48, no. 1, p. 111-133.

Grunert, P., Hinsch, R., Sachsenhofer, R. F., Bechtel, A., Ćorić, S., Harzhauser, M., Piller, W. E., and Sperl, H., 2013, Early Burdigalian infill of the Puchkirchen trough (North Alpine Foreland Basin, Central Paratethys): facies development and sequence stratigraphy: Marine and Petroleum Geology, v. 39, no. 1, p. 164-186.

Grunert, P., Soliman, A., Ćorić, S., Roetzel, R., Harzhauser, M., and Piller, W. E., 2012, Facies development along the tide-influenced shelf of the Burdigalian Seaway: An example from the Ottnangian stratotype (Early Miocene, middle Burdigalian): Marine Micropaleontology, v. 84, p. 14-36.

Grunert, P., Soliman, A., Ćorić, S., Scholger, R., Harzhauser, M., and Piller, W. E., 2010, Stratigraphic re-evaluation of the stratotype for the regional Ottnangian stage (Central Paratethys, middle Burdigalian): Newsletters on Stratigraphy, v. 44, no. 1, p. 1-16.

Guillocheau, F., Rouby, D., Robin, C., Helm, C., and Rolland, N., 2012, Quantification and causes of the terrigeneous sediment budget at the scale of a continental margin: a new method applied to the Namibia-South Africa margin: Basin Research, v. 24, no. 1, p. 3-30.

Gulick, S. P., Jaeger, J. M., Mix, A. C., Asahi, H., Bahlburg, H., Belanger, C. L., Berbel, G. B., Childress, L., Cowan, E., and Drab, L., 2015, Mid-Pleistocene climate transition drives net mass loss from rapidly uplifting St. Elias Mountains, Alaska: Proceedings of the National Academy of Sciences, v. 112, no. 49, p. 15042-15047.

Gusterhuber, J., Dunkl, I., Hinsch, R., Linzer, H.-G., and Sachsenhofer, R., 2012, Neogene uplift and erosion in the Alpine foreland basin (upper Austria and Salzburg): Geologica Carpathica, v. 63, no. 4, p. 295-305.

Gusterhuber, J., Hinsch, R., and Sachsenhofer, R., 2014, Evaluation of hydrocarbon generation and migration in the Molasse fold and thrust belt (Central Eastern Alps, Austria) using structural and thermal basin models: AAPG bulletin, v. 98, no. 2, p. 253-277.

Habler, G., Thöni, M., and Grasemann, B., 2009, Cretaceous metamorphism in the Austroalpine Matsch Unit (Eastern Alps): the interrelation between deformation and chemical equilibration processes: Mineralogy and Petrology, v. 97, no. 3-4, p. 149.

Habler, G., Thöni, M., and Miller, C., 2007, Major and trace element chemistry and Sm–Nd age correlation of magmatic pegmatite garnet overprinted by eclogite-facies metamorphism: Chemical Geology, v. 241, no. 1-2, p. 4-22.

Habler, G., Thöni, M., and Sölva, H., 2006, Tracing the high pressure stage in the polymetamorphic Texel Complex (Austroalpine basement unit, Eastern Alps): P–T–t–d constraints: Mineralogy and Petrology, v. 88, no. 1-2, p. 269-296.

Handy, M., Schmid, S., Paffrath, M., Friederich, W., and the AlpArray Working, G., 2021, European tectosphere and slabs beneath the greater Alpine area – Interpretation of mantle structure in the Alps-Apennines-Pannonian region from teleseismic Vp studies: Solid Earth Discuss., v. 2021, p. 1-61.

Handy, M. R., Schmid, S. M., Bousquet, R., Kissling, E., and Bernoulli, D., 2010, Reconciling plate-tectonic reconstructions of Alpine Tethys with the geological–geophysical record of spreading and subduction in the Alps: Earth-Science Reviews, v. 102, no. 3-4, p. 121-158.

Handy, M. R., Ustaszewski, K., and Kissling, E., 2015, Reconstructing the Alps–Carpathians–Dinarides as a key to understanding switches in subduction polarity, slab gaps and surface motion: International Journal of Earth Sciences, v. 104, no. 1, p. 1-26.

Haq, B. U., Hardenbol, J., and Vail, P. R., 1987, Chronology of fluctuating sea levels since the Triassic: Science, v. 235, no. 4793, p. 1156-1167.

Hawkesworth, C., 1976, Rb/Sr geochronology in the eastern Alps: Contributions to Mineralogy and Petrology, v. 54, no. 3, p. 225-244.

Heinrichs, T., Siegesmund, S., Frei, D., Drobe, M., and Schulz, B., 2012, Provenance signatures from whole-rock geochemistry and detrital zircon ages of metasediments from the Austroalpine basement south of the Tauern Window (Eastern Tyrol, Austria): Geo Alp, v. 9, p. 156-185.

Hejl, E., and Grundmann, G., 1989, Apatit-Spaltspurendaten zur thermischen Geschichte der Nördlichen Kalkalpen, der Flysch-und Molassezone: Jahrbuch der Geologischen Bundesanstalt, v. 132, no. 1, p. 191-212.

Henrichs, I. A., O'Sullivan, G., Chew, D., Mark, C., Babechuk, M. G., McKenna, C., and Emo, R., 2018, The trace element and U-Pb systematics of metamorphic apatite: Chemical Geology.

Hinsch, R., 2008, New insights into the Oligocene to Miocene geological evolution of the Molasse Basin of Austria: OIL GAS-EUROPEAN MAGAZINE, v. 34, no. 3, p. 138-143.

-, 2013, Laterally varying structure and kinematics of the Molasse fold and thrust belt of the Central Eastern Alps: Implications for exploration: AAPG bulletin, v. 97, no. 10, p. 1805-1831.

Hodges, J. L., 1958, The significance probability of the Smirnov two-sample test: Arkiv för Matematik, v. 3, no. 5, p. 469-486.

Hoinkes, G., Thöni, M., Lichem, C., Bernhard, F., Kaindl, R., Schweigl, J., Tropper, P., and Cosca, M., 1997, Metagranitoids and associated metasediments as indicators for the pre-Alpine magmatic and metamorphic evolution of the western Austroalpine Ötztal Basement (Kaunertal, Tirol): Schweiz Mineral Petrogr Mitt, v. 77, p. 299-314.

Holcová, K., 2009, Morphometrical variability of Helicosphaera ampliaperta (calcareous nannoplankton) in the Central Paratethys: biostratigraphic and paleogeographic applications: Neues Jahrbuch für Geologie und Paläontologie-Abhandlungen, v. 253, no. 2-3, p. 341-356.

Horváth, F., Bada, G., Szafián, P., Tari, G., Ádám, A., and Cloetingh, S., 2006, Formation and deformation of the Pannonian Basin: constraints from observational data: Geological Society, London, Memoirs, v. 32, no. 1, p. 191-206.

Hu, D., Böning, P., Köhler, C. M., Hillier, S., Pressling, N., Wan, S., Brumsack, H. J., and Clift, P. D., 2012, Deep sea records of the continental weathering and erosion response to East Asian monsoon intensification since 14 ka in the South China Sea: Chemical Geology, v. 326, p. 1-18.

Huang, H., Imran, J., and Pirmez, C., 2012, The depositional characteristics of turbidity currents in submarine sinuous channels: Marine Geology, v. 329, p. 93-102.

Hubbard, S. M., de Ruig, M. J., and Graham, S. A., 2009, Confined channel-levee complex development in an elongate depo-center: deep-water Tertiary strata of the Austrian Molasse basin: Marine and Petroleum Geology, v. 26, no. 1, p. 85-112.

Huber, B., Bahlburg, H., Berndt, J., Dunkl, I., and Gerdes, A., 2018, Provenance of the Surveyor Fan and precursor sediments in the Gulf of Alaska—Implications of a combined U-Pb,(U-Th)/He, Hf, and rare earth element study of detrital zircons: The Journal of Geology, v. 126, no. 6, p. 577-600.

Hülscher, J., Bahlburg, H., and Pfänder, J., 2018, New geochemical results indicate a non-alpine provenance for the Alpine Spectrum (epidote, garnet, hornblende) in quaternary Upper Rhine sediment: Sedimentary geology, v. 375, p. 134-144.

Hülscher, J., Fischer, G., Grunert, P., Auer, G., and Bernhardt, A., 2019, Selective Recording of Tectonic Forcings in an Oligocene/Miocene Submarine Channel System: Insights From New Age Constraints and Sediment Volumes From the Austrian Northern Alpine Foreland Basin: Frontiers in Earth Science, v. 7, no. 302.

Hülscher, J., Sobel, E. R., Verwater, V., Groß, P., Chew, D., and Bernhardt, A., 2021, Detrital apatite geochemistry and thermochronology from the Oligocene/Miocene Alpine foreland record the early exhumation of the Tauern Window: Basin Research.

Hurford, A. J., and Green, P. F., 1983, The zeta age calibration of fission-track dating: Chemical Geology, v. 41, p. 285-317.

Inger, S., and Cliff, R., 1994, Timing of metamorphism in the Tauern Window, Eastern Alps: Rb-Sr ages and fabric formation: Journal of metamorphic Geology, v. 12, no. 5, p. 695-707.

Jacobsen, S. B., and Wasserburg, G., 1980, Sm-Nd isotopic evolution of chondrites: Earth and Planetary Science Letters, v. 50, no. 1, p. 139-155.

Jäger, E., 1967, Die Bedeutung der Biotit-alterswerte. Rb–Sr Alterbestimmungen am Glimmern der Zentralalpen: Beiträge zur Geologischen Karte der Schweiz, v. 134, p. 28-31.

Jäger, E., Karl, F., and Schmidegg, O., 1969, Rubidium-Strontium-Altersbestimmungen an Biotit-Muskowit-Granitgneisen (Typus Augen-und Flasergneise) aus dem nördlichen Großvenedigerbereich (Hohe Tauern): Tschermaks mineralogische und petrographische Mitteilungen, v. 13, no. 3-4, p. 251-272.

Janz, H., and Vennemann, T. W., 2005, Isotopic composition (O, C, Sr, and Nd) and trace element ratios (Sr/Ca, Mg/Ca) of Miocene marine and brackish ostracods from North Alpine Foreland deposits (Germany and Austria) as indicators for palaeoclimate: Palaeogeography, Palaeoclimatology, Palaeoecology, v. 225, no. 1-4, p. 216-247.

Jerolmack, D. J., and Paola, C., 2010, Shredding of environmental signals by sediment transport: Geophysical Research Letters, v. 37, no. 19.

Ji, W. Q., Malusà, M. G., Tiepolo, M., Langone, A., Zhao, L., and Wu, F. Y., 2019, Synchronous Periadriatic magmatism in the Western and Central Alps in the absence of slab breakoff: Terra Nova, v. 31, no. 2, p. 120-128.

Jin, J., Aigner, T., Luterbacher, H., Bachmann, G. H., and Müller, M., 1995, Sequence stratigraphy and depositional history in the south-eastern German Molasse Basin: Marine and Petroleum Geology, v. 12, no. 8, p. 929-940.

Kagami, H., Ulmer, P., Hansmann, W., Dietrich, V., and Steiger, R. H., 1991, Nd-Sr isotopic and geochemical characteristics of the southern Adamello (northern Italy) intrusives: Implications for crustal versus mantle origin: Journal of Geophysical Research: Solid Earth, v. 96, no. B9, p. 14331-14346.

Kohn, B., Chung, L., and Gleadow, A., 2019, Fission-track analysis: field collection, sample preparation and data acquisition, Fission-track thermochronology and its application to geology, Springer, p. 25-48.

Kremer, C. H., McHargue, T., Scheucher, L., and Graham, S. A., 2018, Transversely-sourced mass-transport deposits and stratigraphic evolution of a foreland submarine channel system: Deep-water tertiary strata of the Austrian Molasse Basin: Marine and Petroleum Geology, v. 92, p. 1-19.

Krenn, E., Schulz, B., and Finger, F., 2012, Three generations of monazite in Austroalpine basement rocks to the south of the Tauern Window: evidence for Variscan, Permian and Eo-Alpine metamorphic events: Swiss Journal of Geosciences, v. 105, no. 3, p. 343-360.

Kuhlemann, J., 2000, Post-collisional sediment budget of circum-Alpine basins (Central Europe): Mem. Sci. Geol. Padova, v. 52, no. 1, p. 1-91.

Kuhlemann, J., 2007, Paleogeographic and paleotopographic evolution of the Swiss and Eastern Alps since the Oligocene: Global and Planetary Change, v. 58, no. 1, p. 224-236.

Kuhlemann, J., Dunkl, I., Brügel, A., Spiegel, C., and Frisch, W., 2006, From source terrains of the Eastern Alps to the Molasse Basin: Detrital record of non-steady-state exhumation: Tectonophysics, v. 413, no. 3, p. 301-316.

Kuhlemann, J., Frisch, W., Dunkl, I., and Székely, B., 2001, Quantifying tectonic versus erosive denudation by the sediment budget: The Miocene core complexes of the Alps: Tectonophysics, v. 330, no. 1-2, p. 1-23.

Kuhlemann, J., and Kempf, O., 2002, Post-Eocene evolution of the North Alpine Foreland Basin and its response to Alpine tectonics: Sedimentary Geology, v. 152, no. 1, p. 45-78.

Küpper, I., and Steininger, F., 1975, Faziostratotypen der Puchkirchener Schichtengruppe: Chronostratigraphie und Neostratotypen, v. 5, p. 205-229.

Lambert, R., 1970, A potassium-argons study of the margin of the Tauern widow at Dllach, Austria: Eclogae Geologicae Helveticae, v. 63, p. 197205.

Le Breton, E., Brune, S., Ustaszewski, K., Zahirovic, S., Seton, M., and Müller, R. D., 2021, Kinematics and extent of the Piemont–Liguria Basin – implications for subduction processes in the Alps: Solid Earth, v. 12, no. 4, p. 885-913.

Lemcke, K., 1988, Das bayerische Alpenvorland vor der Eiszeit. Geologie von Bayern I, Schweizerbart, Stuttgart.

Li, Q., Gasparini, N. M., and Straub, K. M., 2018, Some signals are not the same as they appear: How do erosional landscapes transform tectonic history into sediment flux records?: Geology, v. 46, no. 5, p. 407-410.

Linzer, H.-G., Decker, K., Peresson, H., Dell'Mour, R., and Frisch, W., 2002, Balancing lateral orogenic float of the Eastern Alps: Tectonophysics, v. 354, no. 3-4, p. 211-237.

Linzer, H.-G., Frisch, W., Zweigel, P., Girbacea, R., Hann, H.-P., and Moser, F., 1998, Kinematic evolution of the Romanian Carpathians: Tectonophysics, v. 297, no. 1-4, p. 133-156.

Lippitsch, R., Kissling, E., and Ansorge, J., 2003, Upper mantle structure beneath the Alpine orogen from high-resolution teleseismic tomography: Journal of Geophysical Research: Solid Earth, v. 108, no. B8.

Malusà, M. G., and Fitzgerald, P. G., 2019, Application of thermochronology to geologic problems: bedrock and detrital approaches, Fission-Track Thermochronology and its Application to Geology, Springer, p. 191-209.
Malusà, M. G., Wang, J., Garzanti, E., Liu, Z.-C., Villa, I. M., and Wittmann, H., 2017, Trace-element and Nd-isotope systematics in detrital apatite of the Po river catchment: Implications for provenance discrimination and the lag-time approach to detrital thermochronology: Lithos, v. 290, p. 48-59.
Mark, C., Cogné, N., and Chew, D., 2016, Tracking exhumation and drainage divide migration of the Western Alps: A test of the apatite U-Pb thermochronometer as a detrital provenance tool: Bulletin, v. 128, no. 9-10, p. 1439-1460.
Marshall, J. D., 1992, Climatic and oceanographic isotopic signals from the carbonate rock record and their preservation: Geological magazine, v. 129, no. 2, p. 143-160.
Martin, S., Prosser, G., and Morten, L., 1993, Tectono-magmatic evolution of sheeted plutonic bodies along the north Giudicarie line (northern Italy): Geologische Rundschau, v. 82, no. 1, p. 51-66.
Martini, E., Standard Tertiary and Quaternary calcareous nannoplankton zonation, *in* Proceedings Proc. II Planktonic Conference, Roma 1970, Roma, Tecnoscienza1971, Volume 2, p. 739-785.
Martini, E., 1981, Nannoplankton in der Ober-Kreide, im Alttertiär und im tieferen Jungtertiär von Süddeutschland und dem angrenzenden Österreich: Geologica Bavarica, v. 82, p. 345-356.
Masalimova, L. U., Lowe, D. R., Mchargue, T., and Derksen, R., 2015, Interplay between an axial channel belt, slope gullies and overbank deposition in the Puchkirchen Formation in the Molasse Basin, Austria: Sedimentology, v. 62, no. 6, p. 1717-1748.
McArthur, J., Howarth, R., and Shields, G., 2012, Strontium isotope stratigraphy, *in* Gradstein, F. M., ed., The Geologic Time Scale, Elsevier, p. 127-144.
McDowell, F. W., McIntosh, W. C., and Farley, K. A., 2005, A precise 40Ar–39Ar reference age for the Durango apatite (U–Th)/He and fission-track dating standard: Chemical Geology, v. 214, no. 3-4, p. 249-263.
Mellere, D., Stefani, C., and Angevine, C., 2000, Polyphase tectonics through subsidence analysis: the Oligo-Miocene Venetian and Friuli Basin, north-east Italy: Basin research, v. 12, no. 2, p. 159-182.
Miller, C., and Thöni, M., 1995, Origin of eclogites from the Austroalpine Ötztal basement (Tirol, Austria): geochemistry and Sm・ Nd vs. Rb・ Sr isotope systematics: Chemical Geology, v. 122, no. 1-4, p. 199-225.
Mosbrugger, V., Utescher, T., and Dilcher, D. L., 2005, Cenozoic continental climatic evolution of Central Europe: Proceedings of the National Academy of Sciences of the United States of America, v. 102, no. 42, p. 14964-14969.
Most, P., 2003, Late Alpine cooling histories of tectonic blocks along the central part of the Transalp-Traverse (Inntal-Gadertal): constraints from geochronology [PhD: Eberhardt-Karls-Universität Tübingen.
Müller, W., Mancktelow, N. S., and Meier, M., 2000, Rb–Sr microchrons of synkinematic mica in mylonites: an example from the DAV fault of the Eastern Alps: Earth and Planetary Science Letters, v. 180, no. 3-4, p. 385-397.
Müller, W., Prosser, G., Mancktelow, N. S., Villa, I. M., Kelley, S. P., Viola, G., and Oberli, F., 2001, Geochronological constraints on the evolution of the Periadriatic Fault System (Alps): International Journal of Earth Sciences, v. 90, no. 3, p. 623-653.
Murray, A. B., Lazarus, E., Ashton, A., Baas, A., Coco, G., Coulthard, T., Fonstad, M., Haff, P., McNamara, D., and Paola, C., 2009, Geomorphology, complexity, and the emerging science of the Earth's surface: Geomorphology, v. 103, no. 3, p. 496-505.
Murray, J. W., 2006, Ecology and applications of benthic foraminifera, Cambridge University Press.
Naeser, C., 1979, Fission-track dating and geologic annealing of fission tracks, Lectures in isotope geology, Springer, p. 154-169.
Neumeister, R., 2021, Subsidence Analysis of the Upper Austrian Molasse Basin, unpublished Master Thesis: Freie Universität Berlin, 62 p.
O'Sullivan, G., Chew, D., Kenny, G., Henrichs, I., and Mulligan, D., 2020, The trace element composition of apatite and its application to detrital provenance studies: Earth-Science Reviews, p. 103044.
O'Sullivan, G., Chew, D., Morton, A., Mark, C., and Henrichs, I., 2018, An Integrated Apatite Geochronology and Geochemistry Tool for Sedimentary Provenance Analysis: Geochemistry, Geophysics, Geosystems, v. 19, no. 4, p. 1309-1326.

Ortner, H., Aichholzer, S., Zerlauth, M., Pilser, R., and Fügenschuh, B., 2015, Geometry, amount, and sequence of thrusting in the Subalpine Molasse of western Austria and southern Germany, European Alps: Tectonics, v. 34, no. 1, p. 1-30.

Ortner, H., Reiter, F., and Brandner, R., 2006, Kinematics of the Inntal shear zone–sub-Tauern ramp fault system and the interpretation of the TRANSALP seismic section, Eastern Alps, Austria: Tectonophysics, v. 414, no. 1-4, p. 241-258.

Ortner, H., and Stingl, V., 2001, Facies and basin development of the Oligocene in the Lower Inn Valley, Tyrol/Bavaria, Wien, Österreichische Akademie der Wissenschaften, Schriftreihe der Erdwissenschaftlichen Kommision, Paleogene of the Eastern Alps, v. 14.

Oxburgh, E., Lambert, R. S. J., Baadsgaard, H., and Simons, J., 1966, Potassium argon age studies across the south-east margin of the Tauern Window, the Eastern Alps: Verhandlungen der Geologischen Bundesanstalt, v. 1966, p. 17-33.

Papp, A., 1975, Die Grossforaminiferen des Egerien: Chronostratigraphie und Neostratotypen Miozän der Zentralen Paratethys (eds. T. Báldi and J. Seneš), p. 289-307.

Papp, A., and Steininger, F., 1975, Die Entwicklung der Puchkirchener Schichtengruppe, der Melker und der Michelstettener Schichten in Österreich, *in* Brestenská, E., ed., Chronostratigraphie und Neostratotypen, Miozän der Zentralen Paratethys 5: OM Egerian. Die Egerer, Pouzdˇraner, Puchkirchener Schichtengruppe und die Bretkaer Formation: Bratislava, Verlag der Slowakischen Akademie derWissenschaften, p. 71-75.

Paton, C., Hellstrom, J., Paul, B., Woodhead, J., and Hergt, J., 2011, Iolite: Freeware for the visualisation and processing of mass spectrometric data: Journal of Analytical Atomic Spectrometry, v. 26, no. 12, p. 2508-2518.

Piller, W. E., Harzhauser, M., and Mandic, O., 2007, Miocene Central Paratethys stratigraphy–current status and future directions: Stratigraphy, v. 4, p. 151-168.

Platt, N. H., and Keller, B., 1992, Distal alluvial deposits in a foreland basin setting—the Lower Freshwater Miocene, Switzerland: sedimentology, architecture and palaeosols: Sedimentology, v. 39, no. 4, p. 545-565.

Pomella, H., Klötzli, U., Scholger, R., Stipp, M., and Fügenschuh, B., 2011, The Northern Giudicarie and the Meran-Mauls fault (Alps, Northern Italy) in the light of new paleomagnetic and geochronological data from boudinaged Eo-/Oligocene tonalites: International Journal of Earth Sciences, v. 100, no. 8, p. 1827-1850.

Pomella, H., Stipp, M., and Fügenschuh, B., 2012, Thermochronological record of thrusting and strike-slip faulting along the Giudicarie fault system (Alps, Northern Italy): Tectonophysics, v. 579, p. 118-130.

Prosser, G., 1998, Strike-slip movements and thrusting along a transpressive fault zone: The North Giudicarie line (Insubric line, northern Italy): Tectonics, v. 17, no. 6, p. 921-937.

-, 2000, The development of the North Giudicarie fault zone (Insubric line, Northern Italy): Journal of Geodynamics, v. 30, no. 1-2, p. 229-250.

Purdy, J., and Jäger, E., 1976, K-Ar ages on rock-forming minerals from the Central Alps: Memorie degli Instituti di Geologia e Mineralogia dell'Universitá di Padova, v. 30.

R Core Team, 2020, R: A language and environment for statistical computing.

Raith, M., Raase, P., Kreuzer, H., and Müller, P., 1978, The age of the Alpidic metamorphism in the western Tauern Window, Austrian Alps, according to radiometric dating, *in* Closs, H., Roeder, D., and Schmidt, K., eds., Alps, Apennines, Hellenides, Volume 38, Inter-Union Comm Geodynamics Sci Rep, p. 140-148.

Ratschbacher, L., Dingeldey, C., Miller, C., Hacker, B. R., and McWilliams, M. O., 2004, Formation, subduction, and exhumation of Penninic oceanic crust in the Eastern Alps: time constraints from 40Ar/39Ar geochronology: Tectonophysics, v. 394, no. 3-4, p. 155-170.

Ratschbacher, L., Frisch, W., Linzer, H. G., and Merle, O., 1991, Lateral extrusion in the Eastern Alps, part 2: structural analysis: Tectonics, v. 10, no. 2, p. 257-271.

Reddy, S., Cliff, R., and East, R., 1993, Thermal history of the Sonnblick Dome, south-east Tauern Window, Austria: implications for heterogeneous uplift within the Pennine basement: Geologische Rundschau, v. 82, no. 4, p. 667-675.

Reiners, P. W., and Brandon, M. T., 2006, Using thermochronology to understand orogenic erosion: Annu. Rev. Earth Planet. Sci., v. 34, p. 419-466.

Reiser, H., 1987, Die Foraminiferen der bayerischen Oligozän-Molasse Systematik, Stratigraphie und Paläobathymetrie: Zitteliana, v. 16.

Richard, P., Shimizu, N., and Allegre, C., 1976, 143Nd/146Nd, a natural tracer: an application to oceanic basalts: Earth and Planetary Science Letters, v. 31, no. 2, p. 269-278.
Roddick, J., Cliff, R., and Rex, D., 1980, The evolution of excess argon in alpine biotites—A40Ar-39Ar analysis: Earth and Planetary Science Letters, v. 48, no. 1, p. 185-208.
Rode, S., Rösel, D., and Schulz, B., 2012, Constraints on the Variscan PT evolution by EMP Th-U-Pb monazite dating in the polymetamorphic Austroalpine Oetztal-Stubai basement (Eastern Alps): Zeitschrift der Deutschen Gesellschaft für Geowissenschaften, v. 163, no. 1, p. 43-67.
Rögl, F., 1994, Globigerina ciperoensis (Foraminiferida) in the Oligocene and Miocene of the Central Paratethys: Ann. Naturhist. Mus. Wien, v. 96, p. 133-159.
-, 1998, Palaeogeographic considerations for Mediterranean and Paratethys seaways (Oligocene to Miocene): Annalen des Naturhistorischen Museums in Wien. Serie A für Mineralogie und Petrographie, Geologie und Paläontologie, Anthropologie und Prähistorie, p. 279-310.
Rögl, F., Hochuli, P., and Muller, C., 1979, Oligocene–early Miocene stratigraphic correlations in the Molasse Basin of Austria: Annales Geologiques des Pays Helleniques. Tome Hors Series, v. 30, p. 1045-1050.
Romans, B. W., Castelltort, S., Covault, J. A., Fildani, A., and Walsh, J., 2016, Environmental signal propagation in sedimentary systems across timescales: Earth-Science Reviews, v. 153, p. 7-29.
Rosenberg, C. L., and Berger, A., 2009, On the causes and modes of exhumation and lateral growth of the Alps: Tectonics, v. 28, no. 6.
Rosenberg, C. L., Brun, J. P., Cagnard, F., and Gapais, D., 2007, Oblique indentation in the Eastern Alps: insights from laboratory experiments: Tectonics, v. 26, no. 2.
Rosenberg, C. L., and Garcia, S., 2011, Estimating displacement along the Brenner Fault and orogen-parallel extension in the Eastern Alps: International Journal of Earth Sciences, v. 100, no. 5, p. 1129-1145.
Rosenberg, C. L., and Kissling, E., 2013, Three-dimensional insight into Central-Alpine collision: Lower-plate or upper-plate indentation?: Geology, v. 41, no. 12, p. 1219-1222.
Rosenberg, C. L., and Schneider, S., 2008, The western termination of the SEMP Fault (eastern Alps) and its bearing on the exhumation of the Tauern Window: Geological Society, London, Special Publications, v. 298, no. 1, p. 197-218.
Rosenberg, C. L., Schneider, S., Scharf, A., Bertrand, A., Hammerschmidt, K., Rabaute, A., and Brun, J.-P., 2018, Relating collisional kinematics to exhumation processes in the Eastern Alps: Earth-Science Reviews, v. 176, p. 311-344.
Royden, L. H., 1988, Late Cenozoic Tectonics of the Pannonian Basin System: Chapter 3.
Sachsenhofer, R., Popov, S., Bechtel, A., Coric, S., Francu, J., Gratzer, R., Grunert, P., Kotarba, M., Mayer, J., and Pupp, M., 2017, Oligocene and Lower Miocene source rocks in the Paratethys: palaeogeographical and stratigraphic controls: Geological Society, London, Special Publications, v. 464, p. SP464. 461.
Sachsenhofer, R. F., Leitner, B., Linzer, H.-G., Bechtler, A., Ćoric, S., Gratzer, R., Reischenbacher, D., and Soliman, A., 2010, Deposition, Erosion and Hydrocarbon Source Potential of the Oligocene Eggerding Formation (Molasse Basin, Austria): Austrian Journal of Earth Sciences, v. 103, p. 1-76.
Sadler, P. M., and Jerolmack, D. J., 2015, Scaling laws for aggradation, denudation and progradation rates: the case for time-scale invariance at sediment sources and sinks: Geological Society, London, Special Publications, v. 404, no. 1, p. 69-88.
Satir, M., 1976, Rb-Sr-und K-Ar-Altersbestimmungen an Gesteinen und Mineralien des südlichen Ötztalkristallins und der westlichen Hohen Tauern: Geologische Rundschau, v. 65, no. 1, p. 394-410.
Satir, M., and Morteani, G., 1982, Petrological study and radiometric age determination of the migmatites in the Penninic rocks of the Zillertaler Alpen (Tyrol/Austria): Tschermaks mineralogische und petrographische Mitteilungen, v. 30, no. 1, p. 59-75.
Scharf, A., Handy, M. R., Favaro, S., Schmid, S. M., and Bertrand, A., 2013a, Modes of orogen-parallel stretching and extensional exhumation in response to microplate indentation and roll-back subduction (Tauern Window, Eastern Alps): International Journal of Earth Sciences, v. 102, no. 6, p. 1627-1654.
Scharf, A., Handy, M. R., Ziemann, M. A., and Schmid, S. M., 2013b, Peak-temperature patterns of polyphase metamorphism resulting from accretion, subduction and collision (eastern Tauern Window, European Alps)–a study with Raman microspectroscopy on carbonaceous material (RSCM): Journal of Metamorphic Geology, v. 31, no. 8, p. 863-880.

Schlunegger, F., and Castelltort, S., 2016, Immediate and delayed signal of slab breakoff in Oligo/Miocene Molasse deposits from the European Alps: Scientific Reports, v. 6.
Schlunegger, F., and Kissling, E., 2015, Slab rollback orogeny in the Alps and evolution of the Swiss Molasse basin: Nature communications, v. 6, no. 1, p. 1-10.
Schlunegger, F., Matter, A., Burbank, D., and Klaper, E., 1997, Magnetostratigraphic constraints on relationships between evolution of the central Swiss Molasse basin and Alpine orogenic events: Geological Society of America Bulletin, v. 109, no. 2, p. 225-241.
Schlunegger, F., and Norton, K. P., 2015, Climate vs. tectonics: the competing roles of Late Oligocene warming and Alpine orogenesis in constructing alluvial megafan sequences in the North Alpine foreland basin: Basin Research, v. 27, no. 2, p. 230-245.
Schmid, S. M., Fügenschuh, B., Kissling, E., and Schuster, R., 2004, Tectonic map and overall architecture of the Alpine orogen: Eclogae Geologicae Helvetiae, v. 97, no. 1, p. 93-117.
Schmid, S. M., Scharf, A., Handy, M. R., and Rosenberg, C. L., 2013, The Tauern Window (Eastern Alps, Austria): a new tectonic map, with cross-sections and a tectonometamorphic synthesis: Swiss Journal of Geosciences, v. 106, no. 1, p. 1-32.
Schneider, S., Hammerschmidt, K., and Rosenberg, C. L., 2013, Dating the longevity of ductile shear zones: Insight from 40Ar/39Ar in situ analyses: Earth and Planetary Science Letters, v. 369, p. 43-58.
Schneider, S., Hammerschmidt, K., Rosenberg, C. L., Gerdes, A., Frei, D., and Bertrand, A., 2015, U–Pb ages of apatite in the western Tauern Window (Eastern Alps): tracing the onset of collision-related exhumation in the European plate: Earth and Planetary Science Letters, v. 418, p. 53-65.
Schoene, B., and Bowring, S. A., 2006, U–Pb systematics of the McClure Mountain syenite: thermochronological constraints on the age of the 40 Ar/39 Ar standard MMhb: Contributions to Mineralogy and Petrology, v. 151, no. 5, p. 615.
Schulz, B., Bombach, K., Pawlig, S., and Brätz, H., 2004, Neoproterozoic to Early-Palaeozoic magmatic evolution in the Gondwana-derived Austroalpine basement to the south of the Tauern Window (Eastern Alps): International Journal of Earth Sciences, v. 93, no. 5, p. 824-843.
Schulz, B., Krause, J., and Zimmermann, R., 2019, Electron microprobe petrochronology of monazite-bearing garnet micaschists in the Oetztal-Stubai Complex (Alpeiner Valley, Stubai): Swiss Journal of Geosciences, v. 112, no. 2-3, p. 597-617.
Schuster, R., Scharbert, S., Abart, R., and Frank, W., 2001, Permo-Triassic extension and related HT/LP metamorphism in the Austroalpine-Southalpine realm: Mitt. Ges. Geol. Bergbaustud. Österr, v. 45, p. 111-141.
Schuster, R., Tropper, P., Krenn, E., Finger, F., Frank, W., and Philippitsch, R., 2015, Prograde Permo-Triassic metamorphic HT/LP assemblages from the Austroalpine Jenig Complex (Carinthia, Austria): Austrian Journal of Earth Sciences, v. 108, no. 1, p. 73-90.
Selverstone, J., 1988, Evidence for east-west crustal extension in the Eastern Alps: Implications for the unroofing history of the Tauern Window: Tectonics, v. 7, no. 1, p. 87-105.
Sharman, G. R., Hubbard, S. M., Covault, J. A., Hinsch, R., Linzer, H.-G., and Graham, S. A., 2018, Sediment Routing Evolution in the Northern Alpine Foreland Basin, Austria: interplay of transverse and longitudinal sediment dispersal: Basin Research, no. 30.3, p. 426-447.
Sharman, G. R., Sylvester, Z., and Covault, J. A., 2019, Conversion of tectonic and climatic forcings into records of sediment supply and provenance: Scientific reports, v. 9, no. 1, p. 1-7.
Simpson, G., and Castelltort, S., 2012, Model shows that rivers transmit high-frequency climate cycles to the sedimentary record: Geology, v. 40, no. 12, p. 1131-1134.
Sinclair, H., 1997, Tectonostratigraphic model for underfilled peripheral foreland basins: An Alpine perspective: Geological Society of America Bulletin, v. 109, no. 3, p. 324-346.
Sissingh, W., 1998, Comparative Tertiary stratigraphy of the Rhine Graben, Bresse Graben and Molasse Basin: correlation of Alpine foreland events: Tectonophysics, v. 300, no. 1-4, p. 249-284.
Skeries, W., and Troll, G., 1991, Der Geröllbestand in Molassekonglomeraten des Chiemgaus (Bayern) und seine paläogeographischen Beziehungen zum alpinen Liefergebiet: Zeitschrift der deutschen geologischen Gesellschaft, p. 43-66.
Soliman, A., 2012, Oligocene dinoflagellate cysts from the North Alpine Foreland Basin: new data from the Eggerding Formation (Austria): Geologica Carpathica, v. 63, no. 1, p. 49-70.

Spiegel, C., Kuhlemann, J., Dunkl, I., and Frisch, W., 2001, Paleogeography and catchment evolution in a mobile orogenic belt: the Central Alps in Oligo-Miocene times: Tectonophysics, v. 341, no. 1-4, p. 33-47.

Spiegel, C., Siebel, W., Kuhlemann, J., and Frisch, W., 2004, Toward a comprehensive provenance analysis: A multi-method approach and its implications for the evolution of the Central Alps: Geological Society of America Special Papers, v. 378, p. 37-50.

Stacey, J. t., and Kramers, J., 1975, Approximation of terrestrial lead isotope evolution by a two-stage model: Earth and planetary science letters, v. 26, no. 2, p. 207-221.

Staufenberg, H., 1987, Apatite fission-track evidence for postmetamorphic uplift and cooling history of the Eastern Tauern Window and the surrounding Austroalpine (Central Eastern Alps, Austria): Jahrb. Geol. Bundesanst, v. 130, p. 571-586.

Stefani, C., Fellin, M. G., Zattin, M., Zuffa, G. G., Dalmonte, C., Mancin, N., and Zanferrari, A., 2007, Provenance and paleogeographic evolution in a multi-source foreland: the Cenozoic Venetian–Friulian Basin (NE Italy): Journal of Sedimentary Research, v. 77, no. 11, p. 867-887.

Straub, K. M., Duller, R. A., Foreman, B. Z., and Hajek, E. A., 2020, Buffered, incomplete, and shredded: The challenges of reading an imperfect stratigraphic record: Journal of Geophysical Research: Earth Surface, v. 125, no. 3, p. e2019JF005079.

Tatzel, M., Dunkl, I., and Eynatten, H., 2015, Provenance of Paleo-Rhine sediments from zircon thermochronology, geochemistry, U/Pb dating, and heavy mineral assemblages: Basin Research.

Thomson, S. N., Gehrels, G. E., Ruiz, J., and Buchwaldt, R., 2012, Routine low-damage apatite U-Pb dating using laser ablation–multicollector–ICPMS: Geochemistry, Geophysics, Geosystems, v. 13, no. 2.

Thöni, M., 2003, Sm–Nd isotope systematics in garnet from different lithologies (Eastern Alps): age results, and an evaluation of potential problems for garnet Sm–Nd chronometry [Chem. Geol. 185 (2002) 255–281]: Chemical Geology, v. 194, no. 4, p. 353-379.

Thöni, M., 2006, Dating eclogite-facies metamorphism in the Eastern Alps–approaches, results, interpretations: a review: Mineralogy and Petrology, v. 88, no. 1-2, p. 123-148.

Thöni, M., and Jagoutz, E., 1993, Isotopic constraints for eo-Alpine high-P metamorphism in the Austroalpine nappes of the Eastern Alps: bearing on Alpine orogenesis: Schweizerische Mineralogische und Petrographische Mitteilungen, v. 73, no. 2, p. 177-189.

Thöni, M., and Miller, C., 1996, Garnet Sm–Nd data from the Saualpe and the Koralpe (Eastern Alps, Austria): chronological and P–T constraints on the thermal and tectonic history: Journal of Metamorphic Geology, v. 14, no. 4, p. 453-466.

Thöni, M., and Miller, C., 2000, Permo-Triassic pegmatites in the eo-Alpine eclogite-facies Koralpe complex, Austria: age and magma source constraints from mineral chemical, Rb-Sr and Sm-Nd isotope data: Schweizerische Mineralogische und Petrographische Mitteilungen, v. 80, no. 2), p. 169-186.

Thöni, M., and Miller, C., 2004, Ordovician meta-pegmatite garnet (N-W Ötztal basement, Tyrol, Eastern Alps): preservation of magmatic garnet chemistry and Sm–Nd age during mylonitization: Chemical geology, v. 209, no. 1-2, p. 1-26.

Thöni, M., and Miller, C., 2009, The “Permian event” in the Eastern European Alps: Sm–Nd and P–T data recorded by multi-stage garnet from the Plankogel unit: Chemical Geology, v. 260, no. 1-2, p. 20-36.

Thöni, M., and Miller, C., 2010, Andalusite Formation in a fast exhuming high-P Wedge: Textural, Microchemical and Sm-Nd and Rb-Sr age constraints for a Cretaceous PTT path at Kienberg, Saualpe Eastern Alps: Austrian Journal of Earth Sciences, v. 103, no. 2.

Tofelde, S., Bernhardt, A., Guerit, L., and Romans, B. W., 2021, Times Associated With Source-to-Sink Propagation of Environmental Signals During Landscape Transience: Frontiers in Earth Science, v. 9, no. 227.

Tumiati, S., Thöni, M., Nimis, P., Martin, S., and Mair, V., 2003, Mantle–crust interactions during Variscan subduction in the Eastern Alps (Nonsberg–Ulten zone): geochronology and new petrological constraints: Earth and Planetary Science Letters, v. 210, no. 3-4, p. 509-526.

Vermeesch, P., 2009, RadialPlotter: A Java application for fission track, luminescence and other radial plots: Radiation Measurements, v. 44, no. 4, p. 409-410.

Verwater, V. F., Le Breton, E., Handy, M. R., Picotti, V., Jozi Najafabadi, A., and Haberland, C., 2021, Neogene kinematics of the Giudicarie Belt and eastern Southern Alpine orogenic front (northern Italy): Solid Earth, v. 12, no. 6, p. 1309-1334.

von Eynatten, H., and Dunkl, I., 2012, Assessing the sediment factory: The role of single grain analysis: Earth-Science Reviews, v. 115, no. 1-2, p. 97-120.
von Eynatten, H., Schlunegger, F., Gaupp, R., and Wijbrans, J. R., 1999, Exhumation of the Central Alps: evidence from Ar-40/Ar-39 laserprobe dating of detrital white micas from the Swiss Molasse Basin: Terra Nova, v. 11, no. 6, p. 284-289.
Wade, B. S., Pearson, P. N., Berggren, W. A., and Pälike, H., 2011, Review and revision of Cenozoic tropical planktonic foraminiferal biostratigraphy and calibration to the geomagnetic polarity and astronomical time scale: Earth-Science Reviews, v. 104, no. 1-3, p. 111-142.
Wagner, L. R., 1998, Tectono-stratigraphy and hydrocarbons in the Molasse Foredeep of Salzburg, Upper and Lower Austria: Geological Society, London, Special Publications, v. 134, no. 1, p. 339-369.
Wenger, W. F., 1987, Die Foraminiferen des Miozän ans der bayerischen Molasse und ihre stratigraphische sowie paläogeographische Auswertung: Zitteliana, v. 16, p. 132.
Winterberg, S., 2019, Evolution of the Drainage Network in the Greater Alpine Region Assessed with Geomorphic Analyses and Paleo-Geographic Modelling: ETH Zurich.
Wittmann, H., Malusà, M. G., Resentini, A., Garzanti, E., and Niedermann, S., 2016, The cosmogenic record of mountain erosion transmitted across a foreland basin: Source-to-sink analysis of in situ 10Be, 26Al and 21Ne in sediment of the Po river catchment: Earth and Planetary Science Letters, v. 452, p. 258-271.
Wolff, R., Hetzel, R., Dunkl, I., Anczkiewicz, A. A., and Pomella, H., 2020, Fast cooling of normal-fault footwalls: Rapid fault slip or thermal relaxation?: Geology.
Yang, Y.-H., Wu, F.-Y., Yang, J.-H., Chew, D. M., Xie, L.-W., Chu, Z.-Y., Zhang, Y.-B., and Huang, C., 2014, Sr and Nd isotopic compositions of apatite reference materials used in U–Th–Pb geochronology: Chemical Geology, v. 385, p. 35-55.
Young, J., Bown, P., and Lees, J., 2014, Nannotax3 website: International Nannoplankton Association, v. 21.
Zattin, M., Stefani, C., and Martin, S., 2003, Detrital fission-track analysis and sedimentary petrofacies as keys of alpine exhumation: the example of the Venetian Foreland (European Southern Alps, Italy): Journal of sedimentary research, v. 73, no. 6, p. 1051-1061.
Zimmermann, R., Hammerschmidt, K., and Franz, G., 1994, Eocene high pressure metamorphism in the Penninic units of the Tauern Window (Eastern Alps): evidence from 40 Ar− 39 Ar dating and petrological investigations: Contributions to Mineralogy and Petrology, v. 117, no. 2, p. 175-186.
Zweigel, J., 1998, Eustatic versus tectonic control on foreland basin fill: Contributions to Sedimentary Geology, v. 20.

Appendix

Appendix 1

Three excel files can be found on the attached CD-ROM with the raw data of this study. They contain the:

- Table A1.1 Results of the foraminiferal analysis of Well H and W
- Table A1.2 Results of the calcareous nannofossils analysis of Well H and W
- Table A1.3 Results from the geochemical analysis (TOC, S, CaCO3, $\delta^{13}C_{carb}$, $\delta^{18}O_{carb}$) of Well H, W, and Z

Well log description

Samples for bio- and chemostratigraphy were collected from three drill sites (sampling interval 10–40 m), two from the southern margin of the basin (Well Z and Well W) and one from the northern margin (Well H; Fig. 2.1). Due to the complex depositional setting, the drilled stratigraphy of the sections differs significantly in thickness and grain-size. The formation boundaries in this section are correlated from other wells in the 3D seismic cube, based on RAG inhouse well log interpretation. All given depths are measured depth and not corrected for well-path deflection.

Well H (Fig. 2.4) penetrates a 2385 m thick section of Oligocene to Holocene sediments and cuts through the NSU at around 2345 m. The BHU is penetrated at around 1510 m, the 835 m thick section between these two unconformities is assumed to be part of the Puchkirchen Group (Grunert et al., 2015). At the BHU, no truncated reflectors are visible in the seismic-reflection data, suggesting that minor erosion occurred. In Well H, the HFM is about 710 m thick. The base of the Innviertel Group was encountered at about 800 m. 151 samples were taken from 2385 m up to 700 m.

Well W (Fig. 2.5) was drilled to a depth of 3555 m. From 3503 to 2913 m the ZFM was drilled with a ~ 50 m thick section of conglomerates and sandstones between 3345 to 3295 m. The BHU is located at 1267.5 m, so the assumed thickness of the Puchkirchen Group is about 1644.5 m which includes a large (~30 km^3) mass-transport deposit (Kremer et al., 2018). A section of ~150 m below the BHU shows truncated reflectors in the seismic-reflection data, indicating the erosional character of the unconformity (Figs. 2.5, 2.11). The Hall Formation comprises a thickness of 835.5 m at this location and the base of the Innviertel Formation is

located at 432 m depth. 103 samples were taken in two intervals from 3640 – 3100 m and from 2200 – 400 m, excluding the mass-transport deposit.

Well Z (Fig. 2.6) is 2099 m deep, deflected and penetrates sediments of late Oligocene to Holocene age. A RAG-internal report on samples between 1500 and 750 m by Ćorić and Spezzaferri (2009) focused on foraminifera and nannoplankton (Fig. 2.6). The appearance of *Uvigerina rudligiensis* indicates the UPF from 1500 m to the BHU at 1120 m. The stratigraphically important appearances of *Helicosphaera carteri*, *Helicosphaera sissura* and *Helicosphaera ampliaperta* at 1500 m, 1490 m and 1190 m, respectively, correlates to nannoplankton zones NN1 and NN2 for the UPF. Truncated reflectors ~ 60 m below the BHU indicate erosion (Fig. 2.8). The first appearance of *Uvigerina posthankeni* at 1110 m indicates the HFM, which continues until the end of the investigated interval at 750 m.

Quantification of sediment transport direction in the upper HFM

To determine the sediment transport direction in the upper part of the HFM, the dip azimuth of 29 prograding clinoforms was calculated. Therefore, ten clinoforms were mapped in the western, eight in the eastern and eleven in the central part of the 3D seismic volume. The results of the calculations are shown in Fig. A1.1. Clinoforms in the western part of the basin are dominated by a depositional dip in N to NE direction. In the central part of the basin, clinoforms dip in N to NNE direction, whereas the eastern clinoforms show a N to NNW dip-direction (Fig. A1.1). Therefore, we interpret sediment transport was directed dominantly from S to N.

Figures

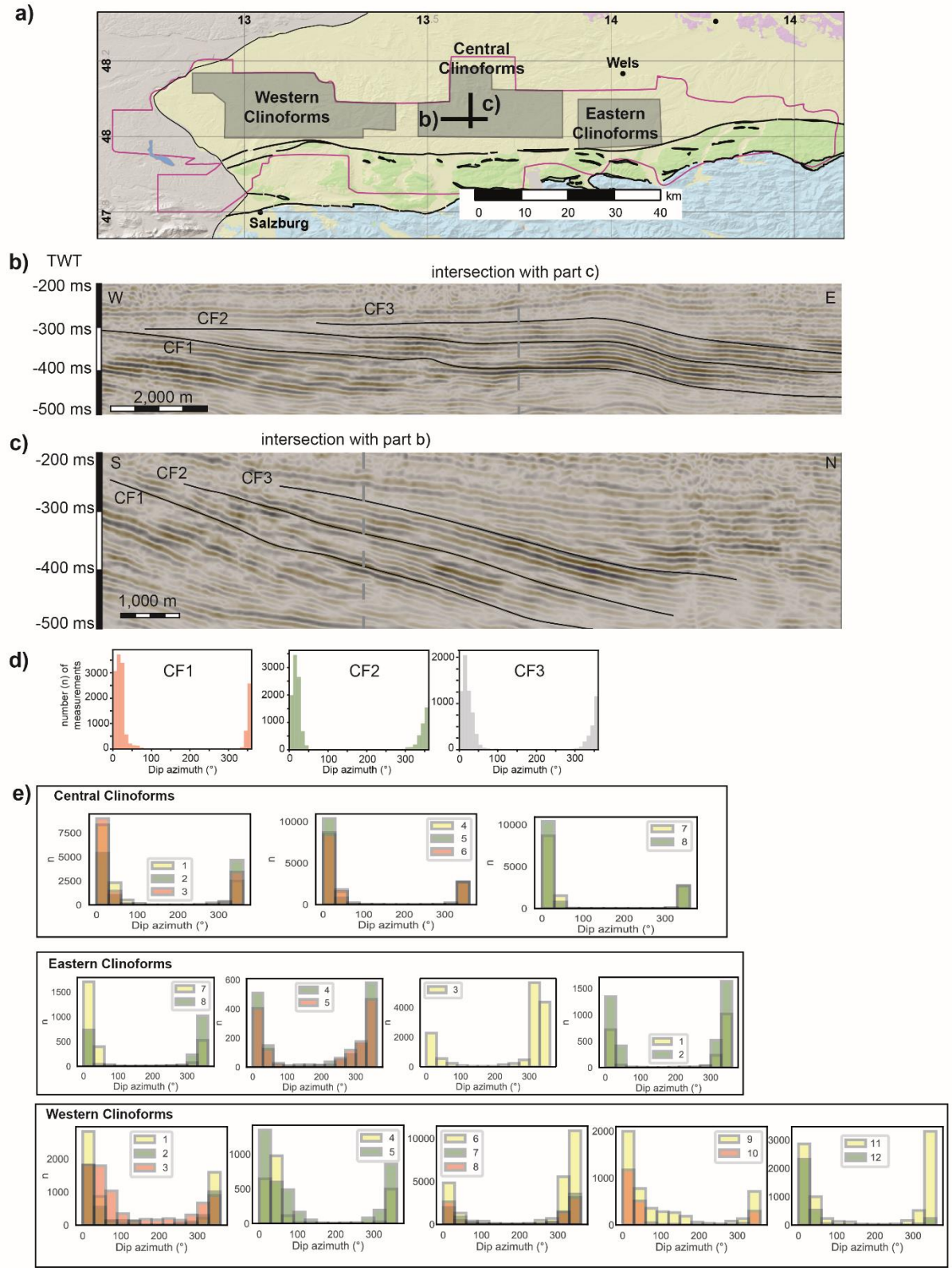

Figure A1.1: Simplified geological map of the Upper Austrian NAFB (a) with the position of seismic cross section in W-E (b) and S-N (c) direction through the upper part of the Hall Formation, please note the prograding clinoforms. The clinoforms indicate a progradation in eastward (b) and northward (c). Three individual bodies were mapped in the 3D seismic volume (for position of cross section see a) and

their dip azimuth was calculated with Petrel(*). The results (d) indicate a domination of an N to NNE dip direction for every individual clinoform. Furthermore, the results from 26 other clinoforms (e) in the upper HFM also indicate a dominantly northward-progradation direction. However, some differences appear between the western and the eastern part of the basin. Whereas in the western part clinoform progradation has an eastward component, in the eastern part of the basin progradation is slightly deflected to the west. This interpretation is hampered by the westward tilting (~0.5 %) of the Austrian NAFB in the Karpatian (Gusterhuber et al., 2012). Seismic cross sections are 10-times vertically exaggerated.

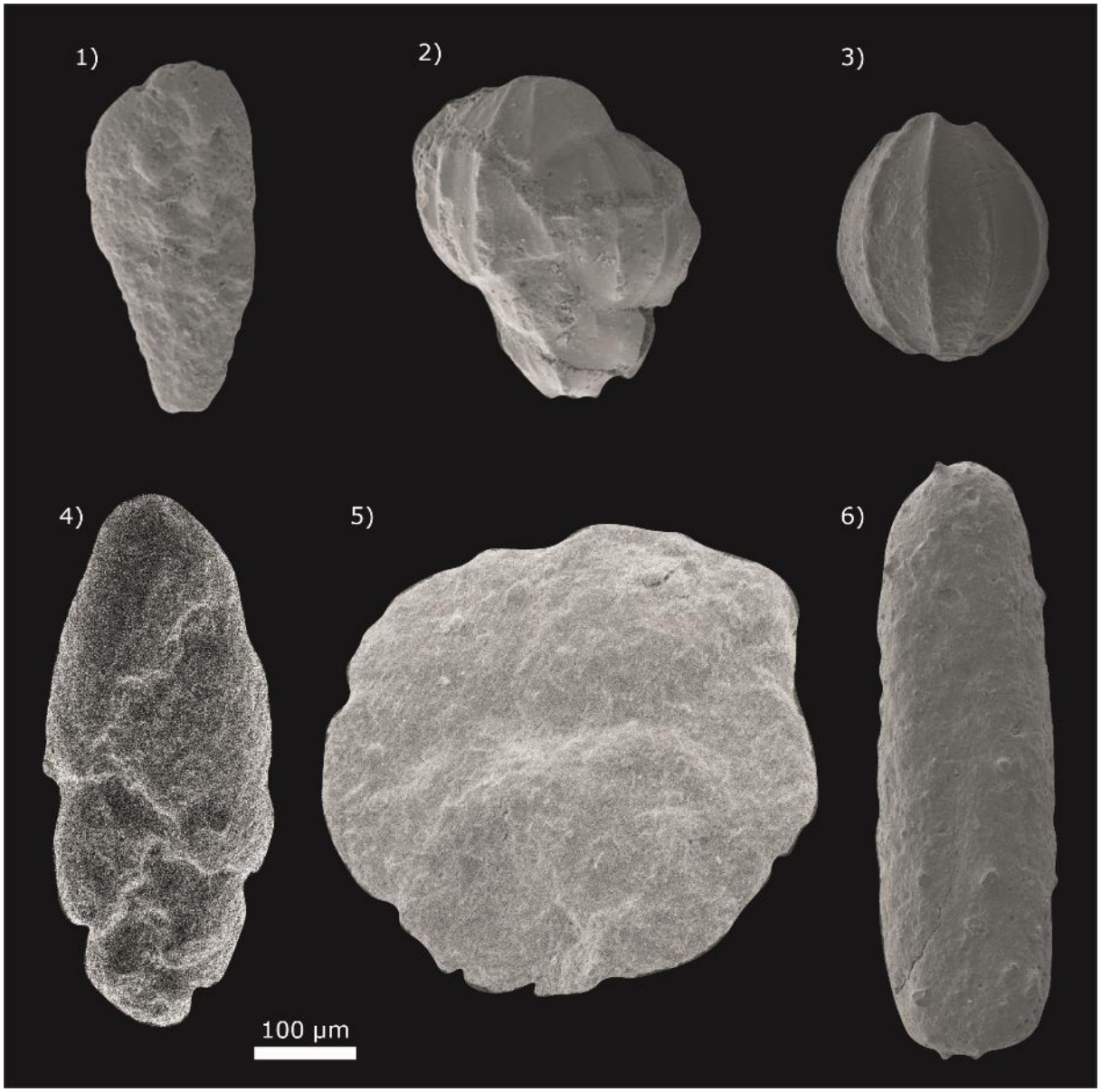

Figure A1.2: SEM pictures of stratigraphic important marker species and their sample number; 1) *Bolivina versatilis* HOFMAN, W-1520; 2) *Uvigerina posthantkeni* PAPP, H-1450; 3) *Amphycorina ottnangensis* TOULA, W-580; 4) *Virgulinella chalkophila* HAGN;, H-2160; 5) *Reticulophragmium aff. amplectens* GRZYBOWSKI, H-2020; 6) *Psammosiphonella cylindrical* GLAESSNER, W-1852

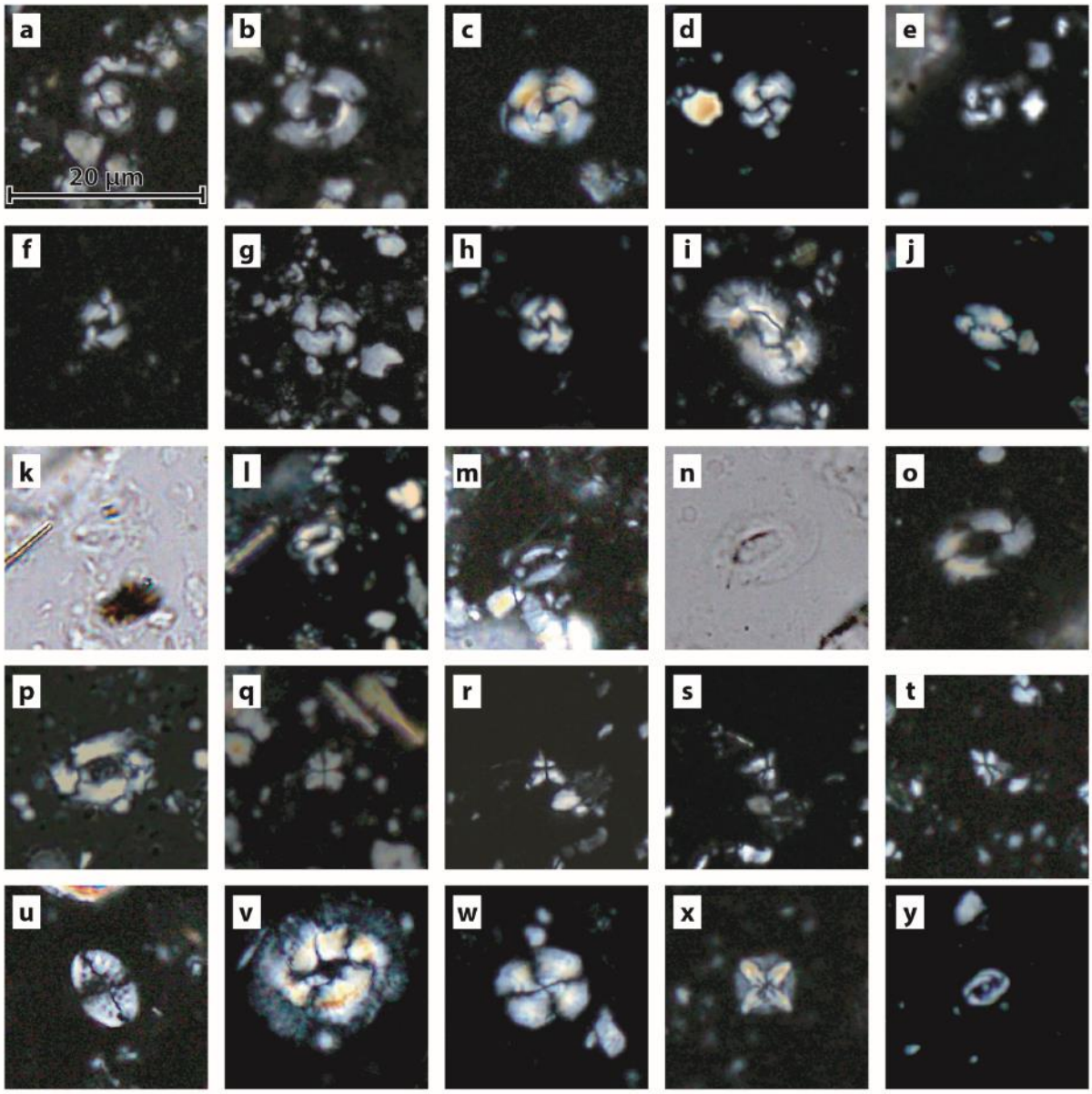

Figure A1.3: Representative calcareous nannofossils from Well W and Well H. Scale bar 20 µm. a) *Coccolithus pelagicus* (Wallich 1877) Schiller, 1930; crossed nicols; Well H: 1000 m; b) *Reticulofenestra umbilicus* (Levin, 1965) Martini & Ritzkowski, 1968; crossed nicols; Well H: 2210 m; c) *Reticulofenestra stavensis* (Levin & Joerger, 1967) Varol, 1989; crossed nicols; Well H: 1000 m; d) *Reticulofenestra bisecta* (Hay, Mohler and Wade, 1966) Roth, 1970; crossed nicols; Well H: 1000 m; e*) Reticulofenestra daviesii* (Haq, 1968) Haq, 1971; crossed nicols; Well H: 1000 m; f) *Reticulofenestra haqii* Backman, 1978; crossed nicols; Well H: 1000 m; g) *Reticulofenestra pseudoumbilicus* (Gartner, 1967) Gartner, 1969; crossed nicols; Well H: 1000 m; h) *Cyclicargolithus floridanus* (Roth & Hay, in Hay et al., 1967) Bukry, 1971; crossed nicols; Well H: 970 m; i) *Helicosphaera euphratis* Haq, 1966; crossed nicols; Well H: 2365 m; j) *Helicosphaera carteri* (Wallich 1877) Kamptner, 1954; crossed nicols; Well H: 1510 m; k) *Helicosphaera scissura* Miller, 1981; parallel nicols; Well H: 1120 m; l) *Helicosphaera scissura* Miller, 1981; crossed nicols; Well H: 1120 m; m) *Helicosphaera ampliaperta* Bramlette and Wilcoxon, 1967 (small); crossed nicols; Well H: 1120 m; n) *Helicosphaera ampliaperta* Bramlette and Wilcoxon, 1967; parallel nicols; Well H: 970 m; o) *Helicosphaera ampliaperta* Bramlette and Wilcoxon, 1967; crossed nicols; Well H: 970 m; p) *Helicosphaera ampliaperta* Bramlette and Wilcoxon, 1967; crossed nicols; Well W: 1260 m; q) *Sphenolithus moriformis* (Brönnimann & Stradner, 1960) Bramlette & Wilcoxon, 1967; crossed nicols; Well H: 1000 m; r) *Sphenolithus delphix* Bukry 1973; crossed nicols (90°); Well W: 1800

m; s) *Sphenolithus delphix* Bukry 1973; crossed nicols (45°); Well W: 1800 m; t) *Sphenolithus disbelemnos* Fornaciari and Rio, 1996; crossed nicols (45°); Sample: Well H: 0850m; u) *Pontosphaera multipora* (Kamptner, 1948 ex Deflandre in Deflandre & Fert, 1954) Roth, 1970; crossed nicols; Sample: Well H: 1000m; v) *Coccolithus eopelagicus* (Bramlette & Riedel, 1954) Bramlette & Sullivan, 1961; crossed nicols; Sample: Well H: 1000m; w) *Watznaueria barnesiae* (Black in Black & Barnes, 1959) Perch Nielsen, 1968; crossed nicols; Sample: Well H: 1000m; x) *Micula staurophora* (Gardet, 1955) Stradner, 1963; crossed nicols; Sample: Well H: 920m; y) *Placozygus fibuliformis* (Reinhardt, 1964) Hoffmann, 1970; crossed nicols; Sample: Well H: 1000m.

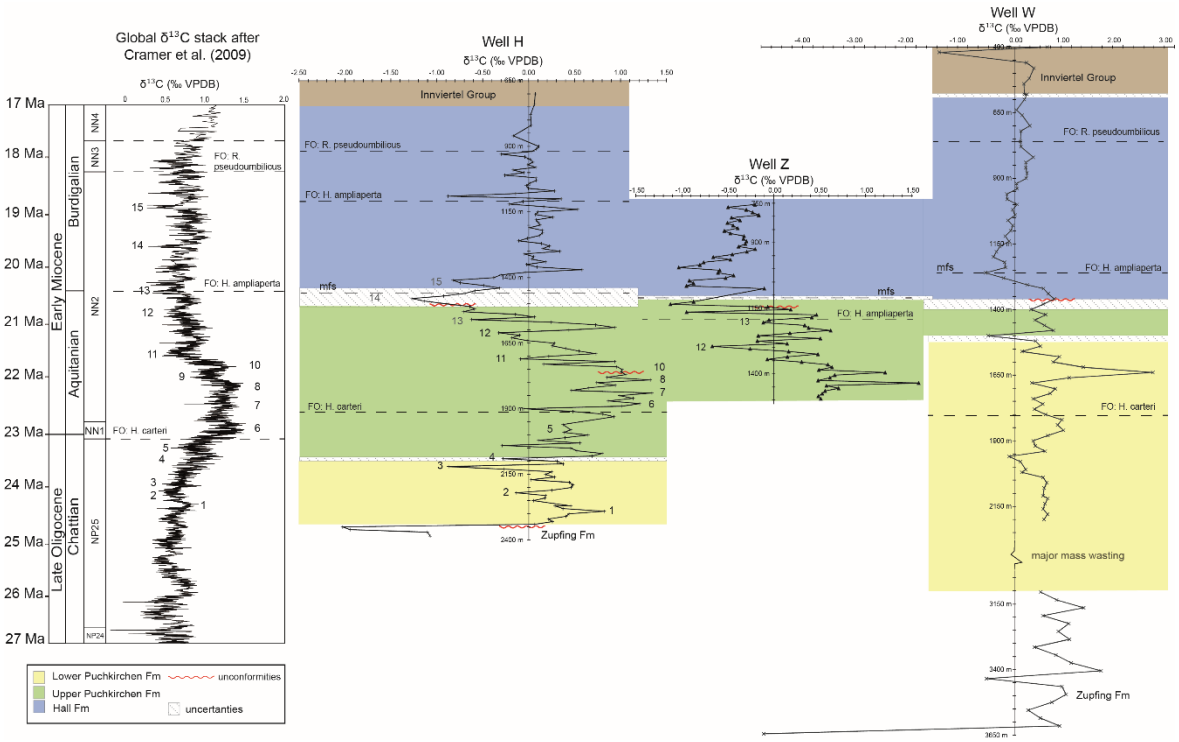

Figure A1.4: Correlation of $^{13}C_{carb}$ data from the Upper Austrian Molasse Basin (Well W, Well H and Z), the global stack of Cramer et al. (2009) and the location of the wells in the 3D seismic cube. Numbers indicate minima and maxima in the global stack that are used for correlation. FO of *Helicosphaera ampliaperta*, *Helicosphaera carteri,* and *Reticulofenestra pseudoumbilicus* are shown. Note that the results of Well W are not suitable for a global correlation due to diagenetic overprint

Appendix 2

Two data tables can be found on the attached CD-ROM. They contain the:

- **Table A2.1:** Results of the Apatite Trace Element Geochemistry and U-Pb isotopic measurements
- **Table A2.2:** Results of the Apatite Fission Track analysis

Sample Locations

Table A2.3: Coordinates and depth of the individual samples in the Upper Austrian Northern Alpine Foreland Basin. Coordinates (Austrian MGI_A_31/Austria GK Centr.-EPSG:31255 coordinate system) are generalized for confidentiality reasons. Depth are given in true vertical depth (TVD) below surface.

Sample	**Latitude (m)**	**Longitude (m)**	**Depth (m, TVD)**
D1	5314000	6000	3300
O1	5346000	-14000	2194
R1	5327000	-14000	2093
F1	5326000	-15000	2145
P1	5325000	4000	2220
L1	5326000	9000	2128
A1	5327000	-13000	1923
T1	5328000	23000	1777
Z1	5326000	-15000	1687
S1	5323000	15000	1781
C1	5329000	22000	1750
H1	5324000	-4000	1850
I1	5326000	-1000	1822
E1	5318000	17000	1175
S2	5327000	-14000	1263
S3	5316000	30000	917
Ü1	5323000	12000	1111
B1	5325000	8000	1169
U1	5315000	20000	2236
N1	5313000	20000	936
G1	5314000	2000	804
FSG1 Coordinates (WGS84)			-
FSG1	48°05’39.85’’N	13°39’50.57’’E	-

Results of the Kolgomorov–Smirnov (K-S) test

Table A2.4a: Results (p values) of the K-S Test of the LREE single-grain geochemistry distribution from the samples of the Puchkirchen Trough. Note that p values <5% indicate that the samples are statistically distinguishable. See text for discussion.

LREE	LPF1	LPF2	LPF3	I1	E1	BHU	HFM	N1	G1
LPF1	-	100%	1%	0%	4%	0%	0%	0%	47%
LPF2	-	-	0%	0%	9%	0%	0%	0%	72%
LPF3	-	-	-	63%	23%	0%	68%	23%	0%
I1	-	-	-	-	24%	1%	53%	38%	2%
E1	-	-	-	-	-	0%	11%	25%	5%
BHU	-	-	-	-	-	-	0%	1%	0%
HFM	-	-	-	-	-	-	-	59%	1%
N1	-	-	-	-	-	-	-	-	0%

Table A2.4b: Results (p values) of the K-S Test of the Sr/Y single-grain geochemistry distribution from the samples of the Puchkirchen Trough. Note that p values <5% indicate that the samples are statistically distinguishable. See text for discussion.

Sr/Y	LPF1	LPF2	LPF3	I1	E1	BHU	HFM	N1	G1
LPF1	-	94%	0%	0%	0%	0%	0%	2%	5%
LPF2	-	-	0%	0%	0%	0%	0%	4%	2%
LPF3	-	-	-	50%	87%	0%	19%	79%	0%
I1	-	-	-	-	39%	2%	75%	41%	0%
E1	-	-	-	-	-	0%	31%	77%	0%
BHU	-	-	-	-	-	-	1%	0%	0%
HFM	-	-	-	-	-	-	-	49%	0%
N1	-	-	-	-	-	-	-	-	0%

Figures

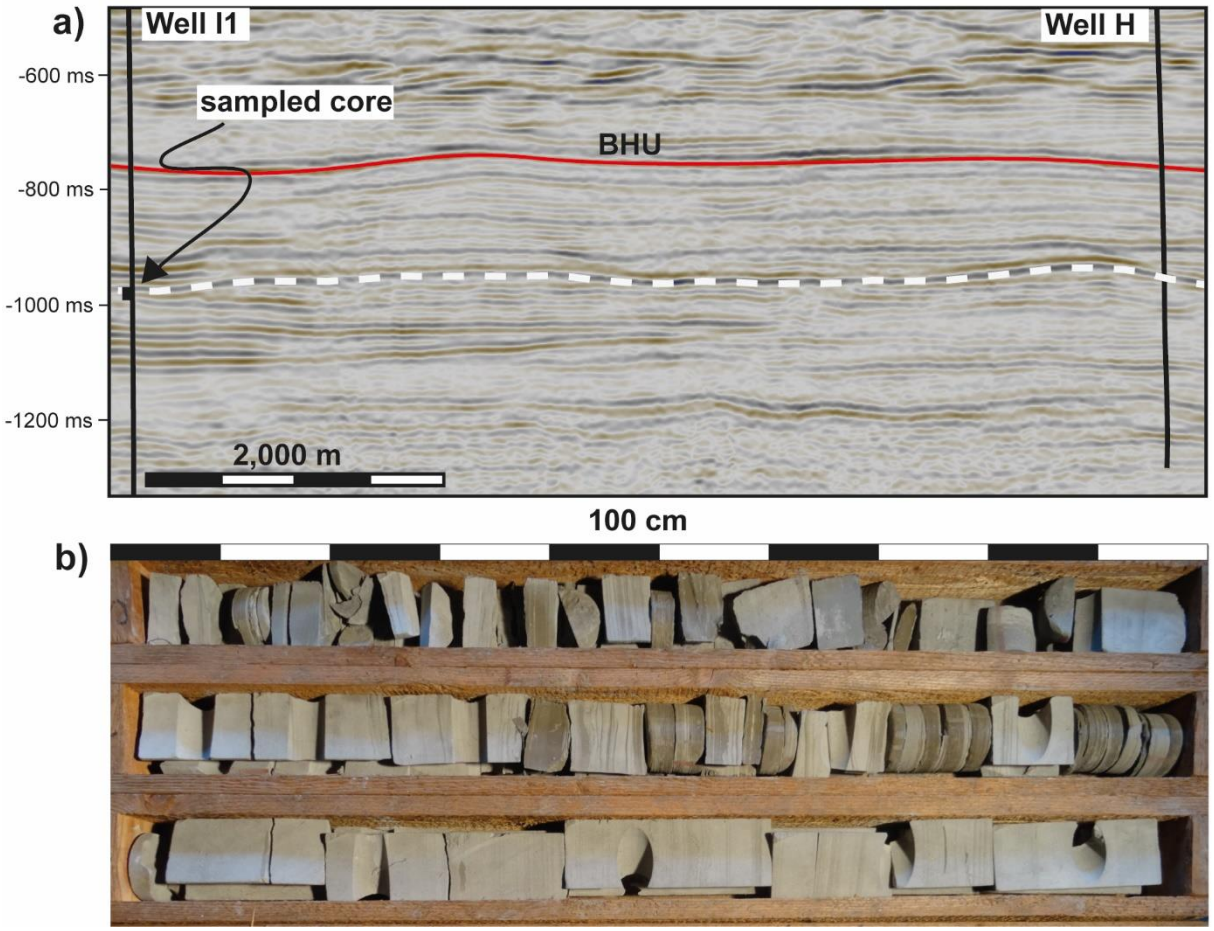

Figure A2.1: a) Seismic cross-section (W-E) on the northern overbanks of the Upper Austrian Northern Alpine Foreland Basin (NAFB) from Well I1 to Well H. Section in Well H was dated via bio- and chemostratigraphy (Hülscher et al., 2019). The depositional age of sample I1 was constrained by correlation of the drill core position via the seismic reflector onto Well H. Seismic reflectors were mapped as timelines. b) Sampled drill core from I1. Individual turbiditic beds were sampled. Note the intercalated sand-rich (lighter color) and marly parts (darker color) of the core. BHU = Base Hall Unconformity.

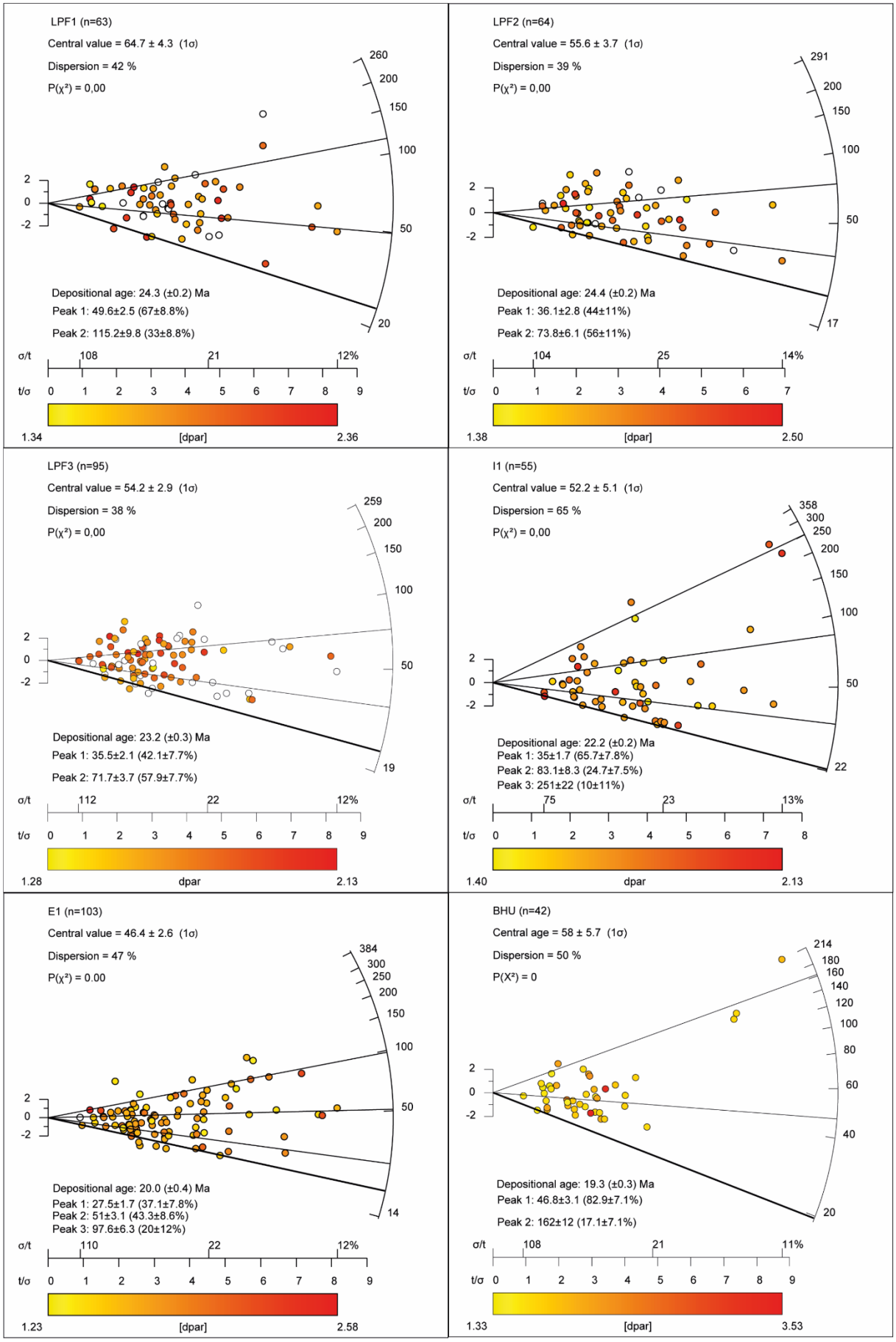
LPF1 (n=63)
Central value = 64.7 ± 4.3 (1σ)
Dispersion = 42 %
P(χ²) = 0,00
Depositional age: 24.3 (±0.2) Ma
Peak 1: 49.6±2.5 (67±8.8%)
Peak 2: 115.2±9.8 (33±8.8%)
σ/t 108 21 12%
t/σ 0 1 2 3 4 5 6 7 8 9
1.34 [dpar] 2.36
LPF2 (n=64)
Central value = 55.6 ± 3.7 (1σ)
Dispersion = 39 %
P(χ²) = 0,00
Depositional age: 24.4 (±0.2) Ma
Peak 1: 36.1±2.8 (44±11%)
Peak 2: 73.8±6.1 (56±11%)
σ/t 104 25 14%
t/σ 0 1 2 3 4 5 6 7
1.38 [dpar] 2.50
LPF3 (n=95)
Central value = 54.2 ± 2.9 (1σ)
Dispersion = 38 %
P(χ²) = 0,00
Depositional age: 23.2 (±0.3) Ma
Peak 1: 35.5±2.1 (42.1±7.7%)
Peak 2: 71.7±3.7 (57.9±7.7%)
σ/t 112 22 12%
t/σ 0 1 2 3 4 5 6 7 8 9
1.28 dpar 2.13
I1 (n=55)
Central value = 52.2 ± 5.1 (1σ)
Dispersion = 65 %
P(χ²) = 0,00
Depositional age: 22.2 (±0.2) Ma
Peak 1: 35±1.7 (65.7±7.8%)
Peak 2: 83.1±8.3 (24.7±7.5%)
Peak 3: 251±22 (10±11%)
σ/t 75 23 13%
t/σ 0 1 2 3 4 5 6 7 8
1.40 dpar 2.13
E1 (n=103)
Central value = 46.4 ± 2.6 (1σ)
Dispersion = 47 %
P(χ²) = 0.00
Depositional age: 20.0 (±0.4) Ma
Peak 1: 27.5±1.7 (37.1±7.8%)
Peak 2: 51±3.1 (43.3±8.6%)
Peak 3: 97.6±6.3 (20±12%)
σ/t 110 22 12%
t/σ 0 1 2 3 4 5 6 7 8 9
1.23 [dpar] 2.58
BHU (n=42)
Central age = 58 ± 5.7 (1σ)
Dispersion = 50 %
P(X²) = 0
Depositional age: 19.3 (±0.3) Ma
Peak 1: 46.8±3.1 (82.9±7.1%)
Peak 2: 162±12 (17.1±7.1%)
σ/t 108 21 11%
t/σ 0 1 2 3 4 5 6 7 8 9
1.33 [dpar] 3.53

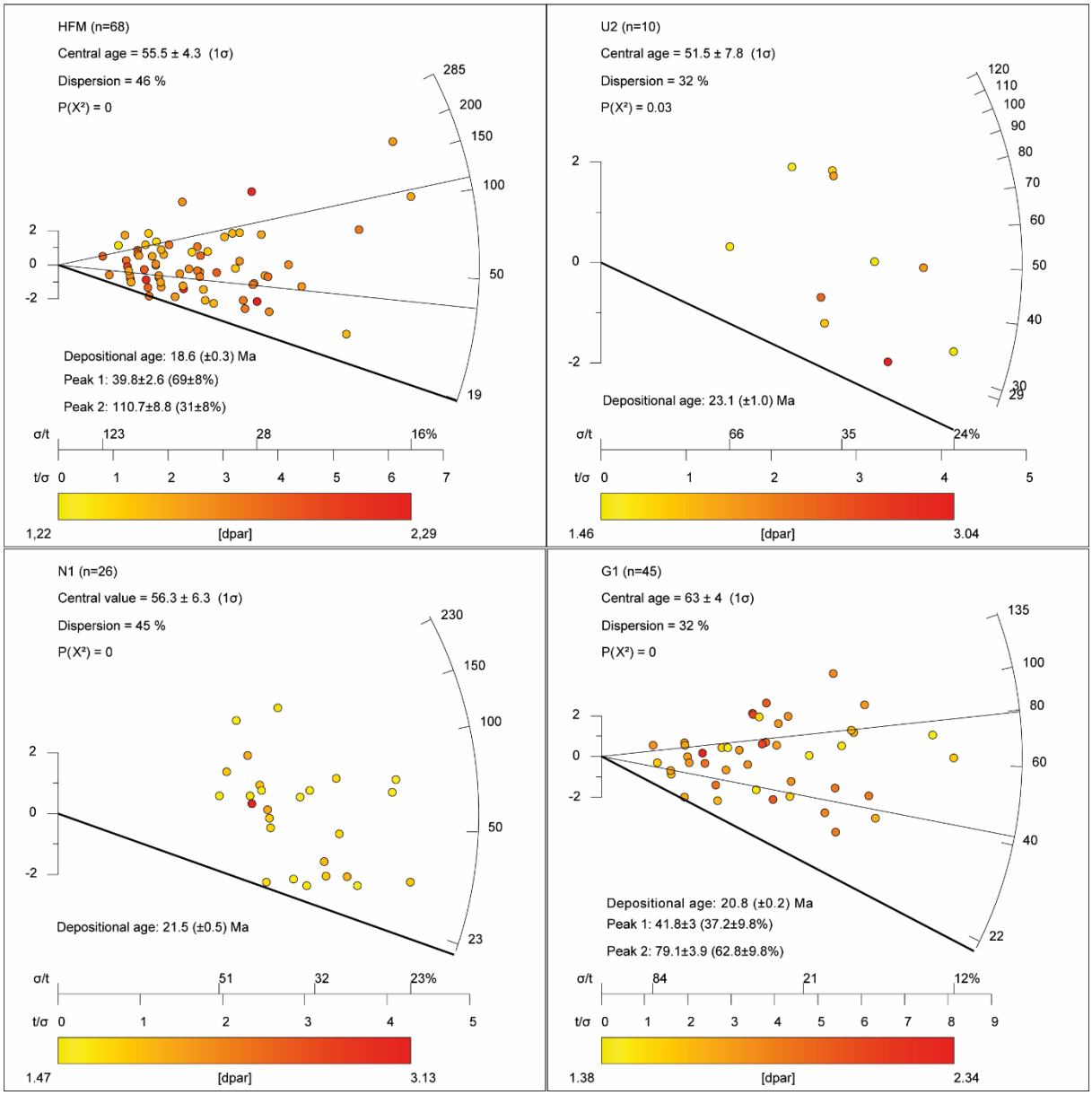

Figure A2.2: Radial plots of the results of the Apatite Fission Track (AFT) Analysis of all dated grains and modelled grain-age populations. Note that all samples fail the χ^2-Test. Colors represents the measured dpar-values of every grain. Thick black line represents the depositional age of the sample group from Tab. 3.1.

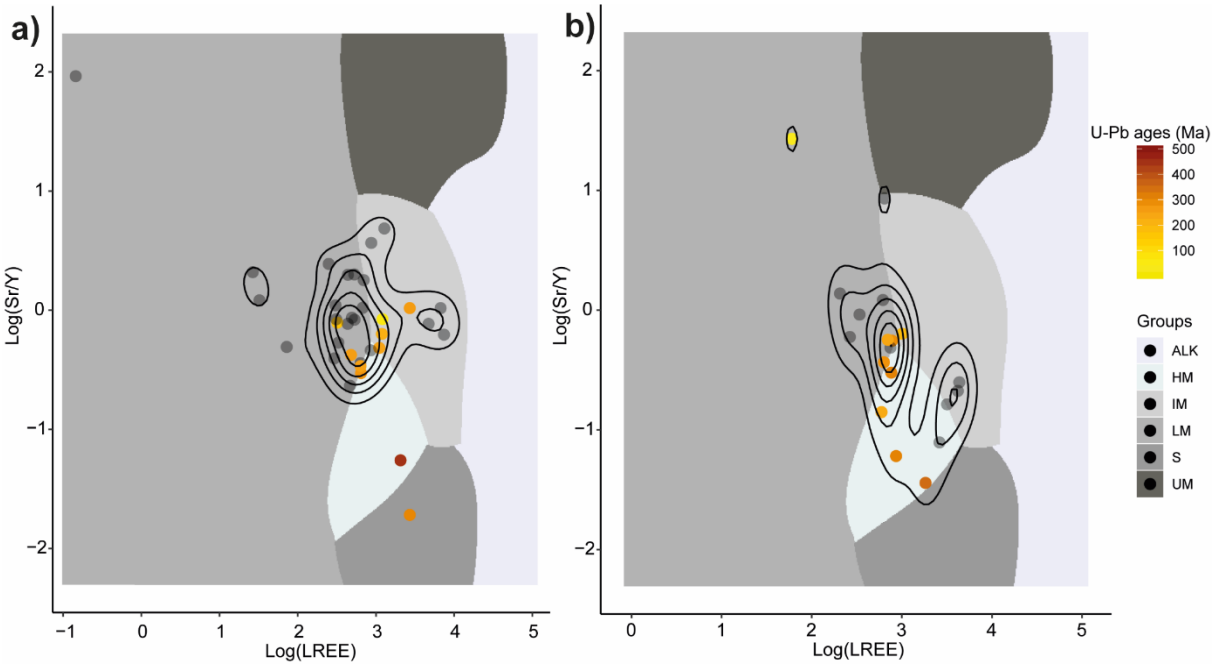

Figure A2.3: Apatite discrimination diagram of samples D1 (a) and U1 (b) after O'Sullivan et al. (2020) (Log (LREE) vs. Log (Sr/Y) plots; alkali-rich igneous rocks (ALK); mafic I-type granitoids and mafic igneous rocks (IM); low- and medium-grade metamorphic (<upper amphibolite-facies) and metasomatic (LM); partial-melts/leucosomes/high-grade metamorphic (HM); S-type granitoids and high aluminum saturation index (ASI>1.1) 'felsic' I-types (S); ultramafic rocks including carbonatites, lherzolites and pyroxenites (UM)). Black lines in the plots are 2D density contours to visualize the density distribution of each sample. Data points are color coded by their U-Pb age (see color bar on the right). Grey points = no U-Pb age.

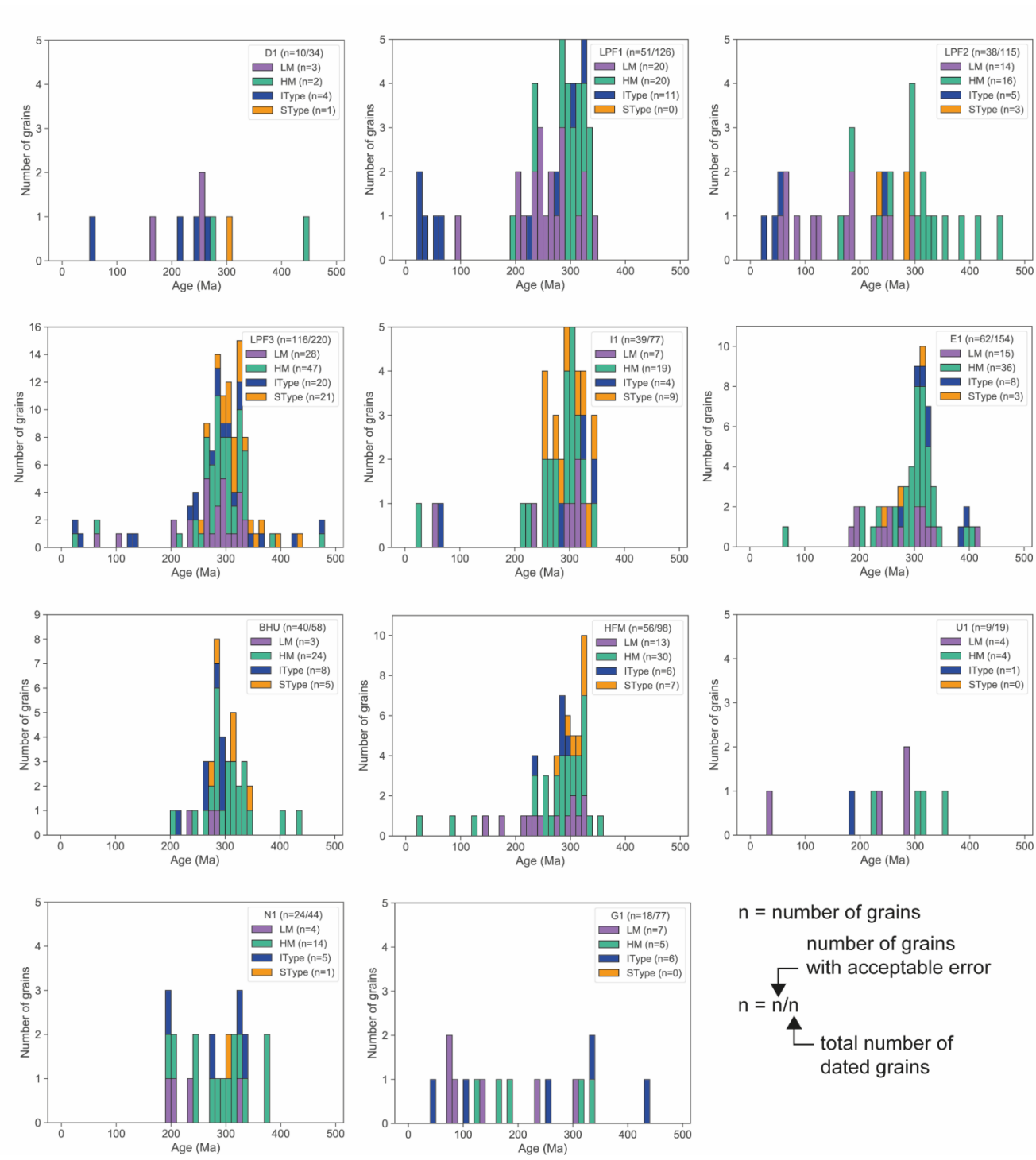

Figure A2.4: Histogram of the accepted apatite U-Pb ages grouped by their samples and colored by the ATE classification following O'Sullivan et al. (2020).

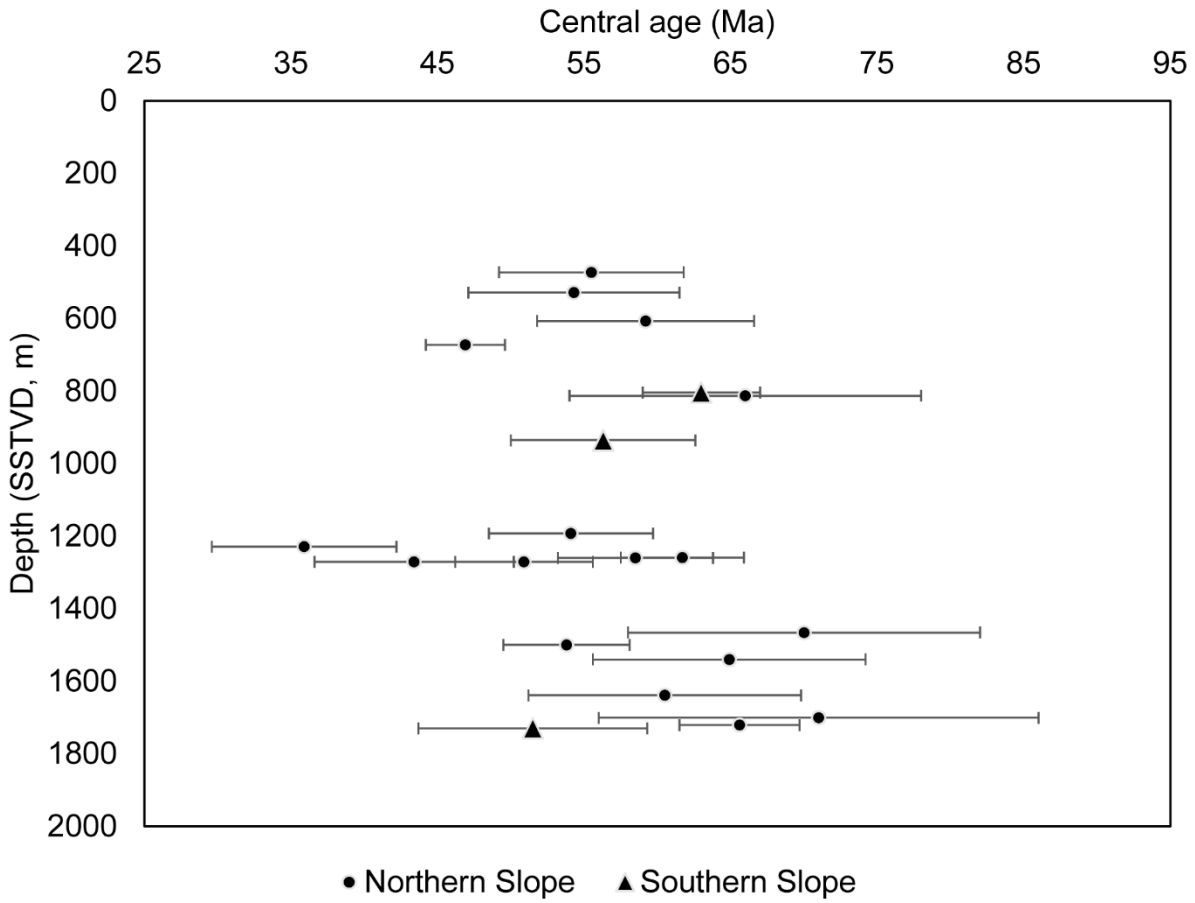

Figure A2.5: Central Age (Ma) vs. Depth (SSTVD (m)) plot of the calculated AFT central ages (error bars represent 1σ standard deviation) against the depth of the sampled drill core (SSTVD = SubSea True Vertical Depth). Note that there is no tendency towards younger central age with increasing sampled depth. Therefore, post-depositional annealing in the basin by burial of the material does not represent a significant source of error in the results.

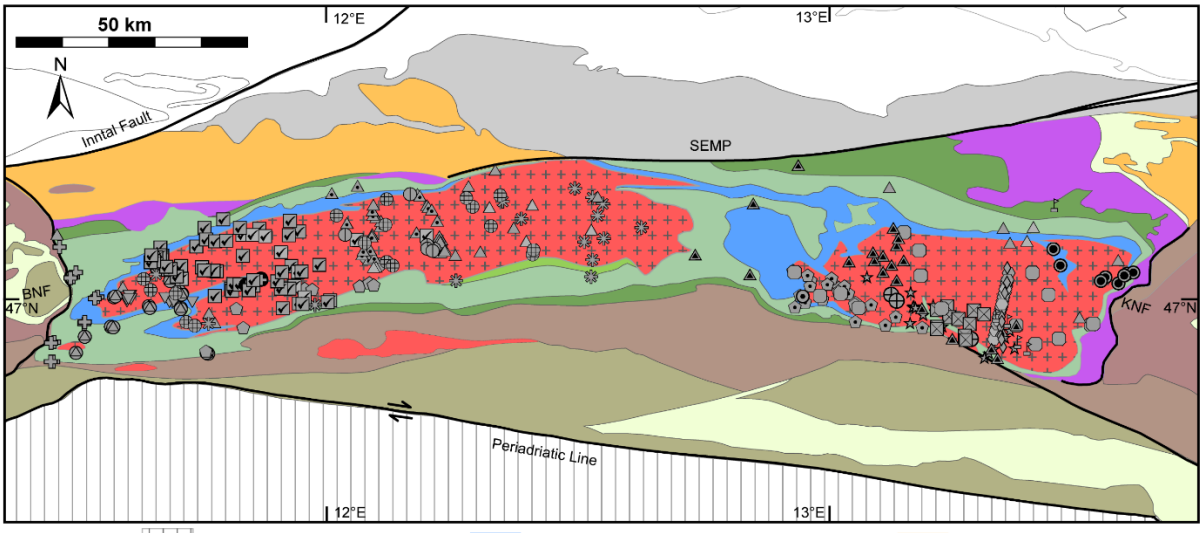

Compiled thermochronological data sets:

Bertrand et al. (2017)	Foeken et al. (2007)	Lambert (1970)	Satir (1976)
Blankenburg et al. (1989)	Fügenschuh et al. (1997)	Most (2003)	Satir & Morteani (1982)
Borsi (1978)	Grundmann & Morteani (1985)	Oxburgh et al. (1966)	Scharf et al. (2013)
Cliff et al. (1985)	Hawkesworth (1976)	Raith (1978)	Schneider et al. (2015)
Dunkl et al. (2003)	Inger & Cliff (1994)	Reddy et al. (1993)	Staufenberg (1987)
Favaro et al. (2015)	Jäger et al. (1969)	Roddick et al. (1980)	

Figure A2.6: Simplified geological map of the Tauern Window (after Schmid et al. (2004)) with sampling locations of the data shown in Fig. 3.10. Compiled literature data: Bertrand et al. (2017); Blanckenburg et al. (1989); Borsi (1978); Cliff et al. (1985); Dunkl et al. (2003); Favaro et al. (2015); Foeken et al. (2007); Fügenschuh et al. (1997); Grundmann and Morteani (1985); Hawkesworth (1976); Inger and Cliff (1994); Jäger et al. (1969); Lambert (1970); Most (2003); Oxburgh et al. (1966); Raith et al. (1978); Reddy et al. (1993); Roddick et al. (1980); Satir (1976); Satir and Morteani (1982); Scharf et al. (2013a); Schneider et al. (2015); Staufenberg (1987).

Appendix 3

Two excel files with the raw data of this study can be found on the attached CD-ROM. They contain the:

- Table A3.1: Results of the Apatite Sm-Nd isotopic analysis
- Table A3.2: Results of Clay Nd isotopic analysis

Methods

Clay Nd isotopic composition

Thirty well-cutting samples were selected for the separation of the clay-size fraction and the analysis of their Nd isotopic composition. Samples were mixed with distilled water and centrifuged for 1 min at 4000 U/min. The suspended fraction was decanted and dried in an oven. The separated clay samples were treated with 10 % acetic acid and washed with Milli-Q water. Because all samples contained significant amounts of organic material, 23 samples were heated up to 830°C in a muffle furnace for combustion of organic materials. In seven samples, organic material was removed by chemical treatment during digestion using conc. HNO_3 and H_2O_2.

100 mg of sample material was digested in a 3:2 mixture of concentrated HF-HNO_3 at 120°C for 24 h. After dry down, they were treated three times with 2 ml HNO_3 and dried. This was followed by 12 h calibration in 6 M HCl. After dry down, each sample was taken up in calibrated 2.5 M HCl and centrifuged. The separation of Nd followed the protocol of Richard et al. (1976). The REE were separated using cation exchange resin (AG 50WX8 resin) with HCl. After dry down at 120°C, the REE cuts were taken up in 0.15 M HCl and Nd was separated from other REE on columns using coated Teflon powder cation exchange resin (PTFE in HDEHP). After extraction, Nd cuts were dried at 120°C and dissolved in 1 ml 0.25 M HNO_3. Procedural blanks were < 20 pg for the samples where organic was combusted. For the unheated samples, the procedural blank was < 130 ng. All blanks were negligible and no correction necessary.

Samples were analyzed for their $^{143}Nd/^{144}Nd$ ratios with a Thermo Scientific Neptune Plus multi-collector inductively coupled plasma mass spectrometer at the Institut für Mineralogie (Westfälische Wilhelms-Universität Münster). JNdi-1 solution was used as reference material during analysis, reavealing $^{143}Nd/^{144}Nd = 0.512096$ (±8, 2σ standard deviation, $n = 17$). The data is reported relative to JNdi-1 $^{143}Nd/^{144}Nd = 0.512099$ (Garçon et al., 2018). Results were normalized to $^{146}Nd/^{144}Nd = 0.7219$ using the exponential law.

Sm-Nd isotope analysis of detrital apatites

Nd isotope analyses were carried out at the Geochronology and Tracers Facility, British Geological Survey, Keyworth, UK, using a Thermo Scientific Neptune Plus MC-ICP-MS coupled to a New Wave Research UP193UC Excimer laser ablation system. Helium was used as the carrier gas through the ablation cell with Ar make-up gas being connected via a T-piece and sourced from a Cetac Aridus II desolvating nebulizer. The instrument was tuned for low oxide production, and 0.008 l/min of nitrogen were introduced via the nebulizer in addition to Ar in order to minimize oxide formation.

For neodymium isotope analysis, $^{142}Ce+^{142}Nd$, ^{143}Nd, $^{144}Nd+^{144}Sm$, ^{145}Nd, ^{146}Nd, ^{147}Sm, ^{149}Sm, ^{150}Nd and ^{151}Eu were measured simultaneously during static 30 second ablation analyses. Because of the relatively small grain size of the apatites, a 35 µm laser spot was used for most samples. Where grain size allowed, a 50 µm spot was used. The laser fluence was 8–10 J/cm^2. Correction for ^{144}Sm on the ^{144}Nd peak was carried out using the method of Yang et al. (2014). Madagascar apatite was used as the primary reference material for laser ablation analysis. The Durango apatite reference material was also analyzed thought the analytical session, along with the standard glasses JNd-i, JNd-i LREE, and NIST 610. Data reduction was carried out the Iolite data reduction package (Paton et al., 2011). Analytical uncertainties for unknowns were propagated by quadratic addition to include the standard error of the mean of the analysis and the reproducibility of the Durango reference material. εNd values were calculated using a ^{147}Sm decay constant of 6.54 x $10^{-12}y^{-1}$ (DePaolo and Wasserburg, 1976) the present-day chondritic $^{147}Sm/^{144}Nd$ value of 0.1967 and $^{147}Sm/^{144}Nd$ ratio of 0.512638 (Jacobsen and Wasserburg, 1980).

Robust estimation of the shift in clay-sized Neodymium isotopic composition

In order to provide a robust estimate of the shift in Neodymium isotopic composition of the clay-sized bulk-rock fraction in mean and variance between the unbalanced subsamples for >19Ma (n1 = 25 (4 double measurements)) and for <19Ma (n2 =5 (+2)) εNd measurements, we performed n_{MC} = 10,000 random sampling from each measurement assuming normal measurement error (Fig. 4.2 µ and 2σ-intervall). Double measurements from replicate analyses have been randomly selected once for all n_{MC} samples. The distribution of the n_{MC} random sample means appears normal distributed for both samples as expected by the Central Limit Theorem with a mean μ_1 = -9.674 (σ_1 = 0.018, >19Ma) and μ_2 = -9.121 (σ_2 = 0.038, <19Ma).

Therefore, we applied a Student's t-test suggesting an increase of 0.5520 to 0.5536 with 95%-confidence and p-value < 10^{-15} under assumption of heteroscedasticity (p-value < 10^{-15}). The statistical analyses were performed in R Vers. 4.0.2 using stats-package (R Core Team, 2020)

Figures

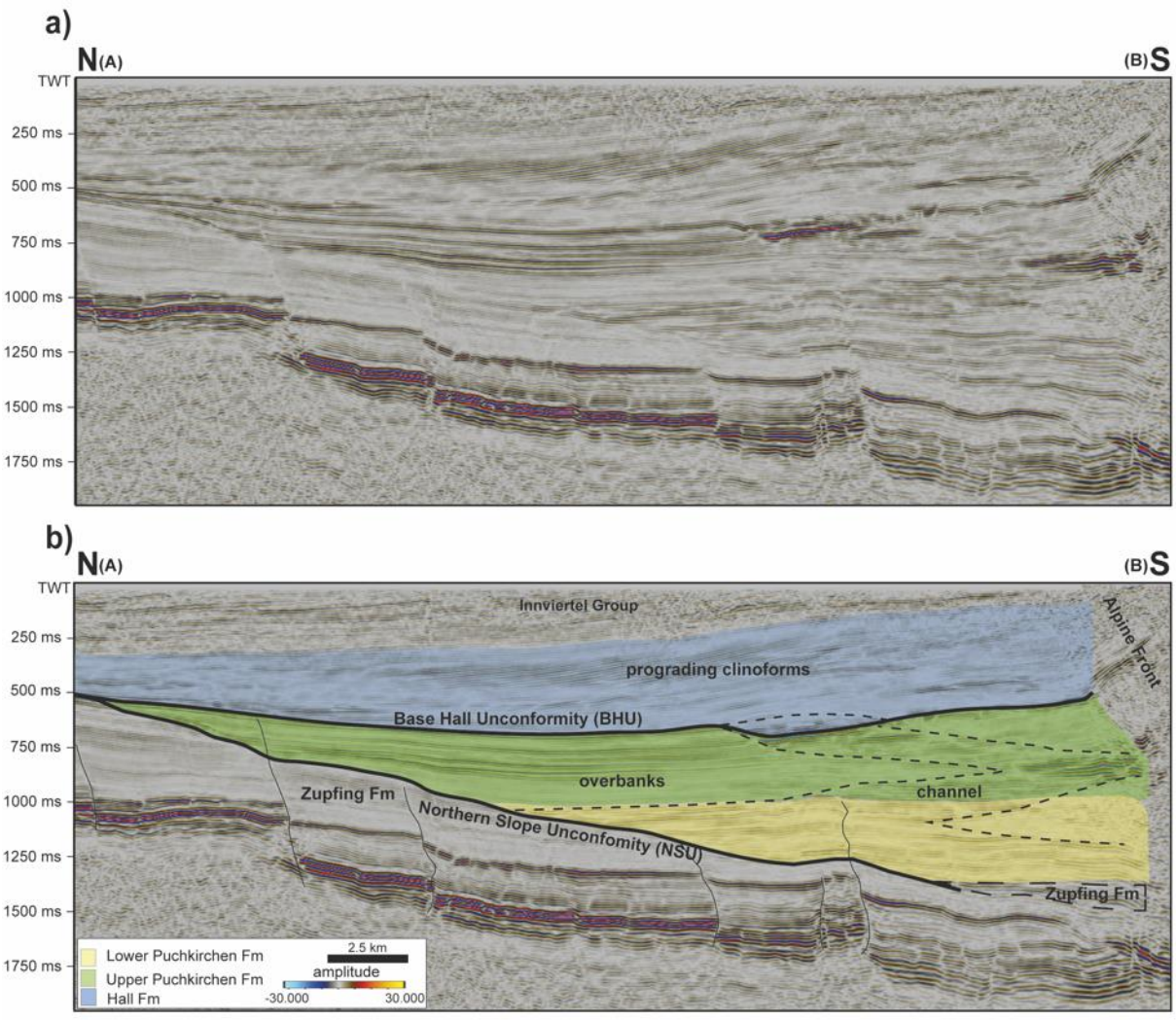

Figure A3.1: Seismic cross-section (N-S) through the Upper Austrian NAFB (see Fig. 4.1 for position), a) uninterpreted, b) interpreted cross section. The channel is located close to the northern alpine thrust front and is lateral mobile through time. To the north the channel is bordered by wide (≤ 15 km) overbanks in which Well H was drilled. The southern board of the Upper Austrian Northern Alpine Foreland Basin is steep, was tectonically active and submarine fans propagated from here into the basin. In the Hall Formation the sediment-transport system changed from an eastward directed to a northward directed transport. Note the BHU, the NSU and the prograding clinoforms in the Hall Formation. The stratigraphic concept is taken from Hülscher et al. (2019).

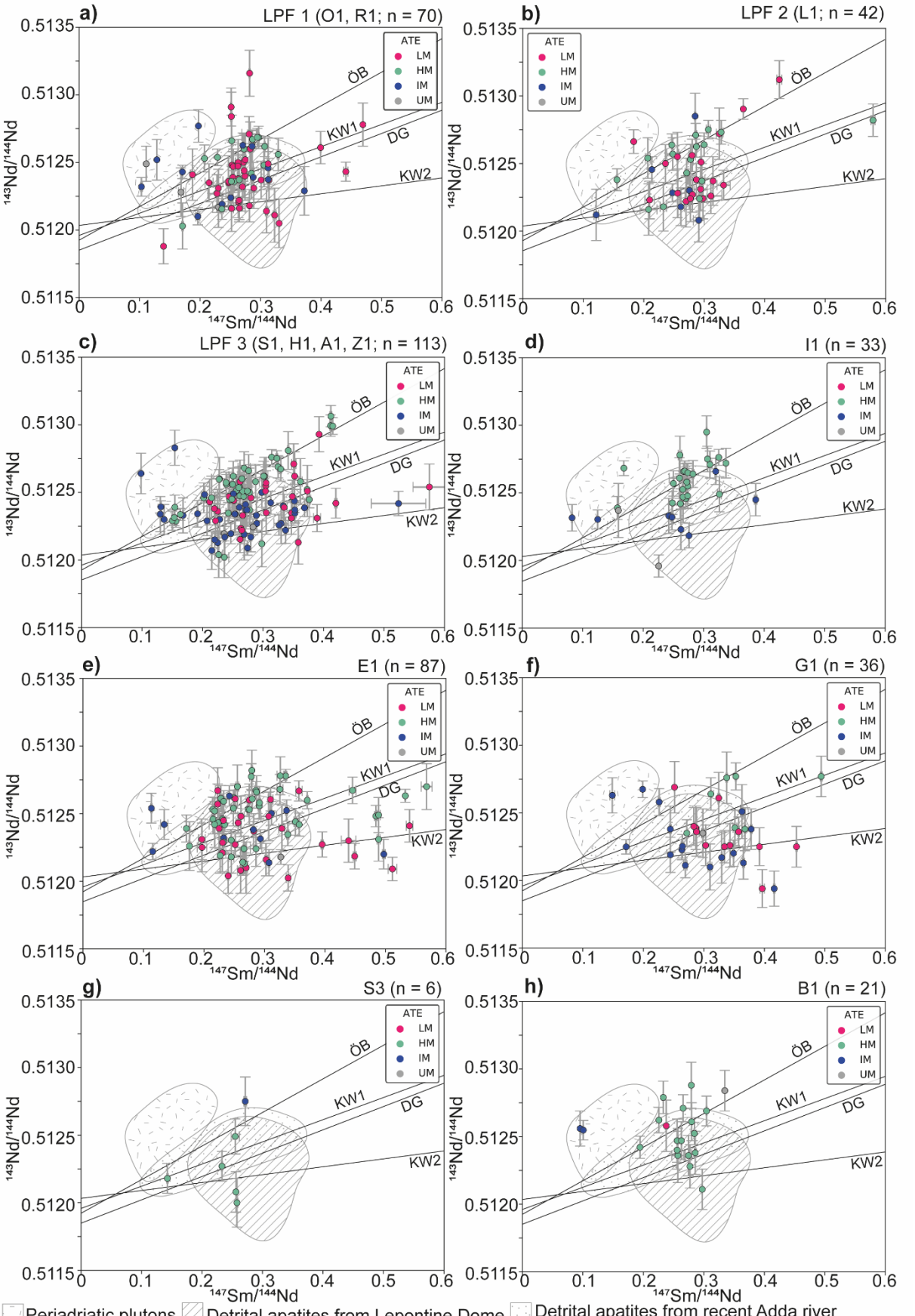
a)
LPF 1 (O1, R1; n = 70)
b)
LPF 2 (L1; n = 42)
c)
LPF 3 (S1, H1, A1, Z1; n = 113)
d)
I1 (n = 33)
e)
E1 (n = 87)
f)
G1 (n = 36)
g)
S3 (n = 6)
h)
B1 (n = 21)
ATE
LM
HM
IM
UM
ÖB
KW1
DG
KW2
143Nd/144Nd
147Sm/144Nd
0.5135
0.5130
0.5125
0.5120
0.5115
0
0.1
0.2
0.3
0.4
0.5
0.6
Periadriatic plutons
Detrital apatites from Lepontine Dome
Detrital apatites from recent Adda river
(Silvretta Seckau & Lower Austroalpine Nappes)

Figure A3.2 (previous page): $^{147}Sm/^{144}Nd$ vs $^{143}Nd/^{144}Nd$ plot of the detrital apatites from the Lower Puckirchen Formation (a-c), the Upper Puchkirchen Formation (d-f) and the Hall Formation (g,h). Note that the samples G1 (f) and S3 (g) were taken from the southern slope of the basin, whereas all other samples were taken from the northern slope of the basin and the channel. Results are color-coded by their source-rock classification based on the apatite trace-element geochemistry (O'Sullivan et al., 2020). IM = mafic I-type granitoids and mafic igneous rocks; LM = low- and medium-grade metamorphic (<upper amphibolite-facies) and metasomatic; HM = partial-melts/leucosomes/high-grade metamorphic and S-type granitoids and high aluminum saturation index (>1.1) 'felsic' I-types; UM = ultramafic rocks including carbonatites, lherzolites and pyroxenites. The lines (ÖB, KW1, DG, KW2) represent pseudoisochrones defined by whole rock and mineral data from the Eastern Alps. To construct those pseudoisochrones, we compiled published data from the different Eastern Alpine nappe systems (ÖB = Ötztal Bundshuh Nappe System; KW1 = Koralpe-Wölz Nappe System with Permian Sm-Nd ages; DG: Drauzug-Gurktal Nappe System; KW2 = Koralpe-Wölz Nappe System with Cretaceous Sm-Nd ages) and calculated Sm-Nd pseudoisochrones for an entire nappe system. Note that all pseudoisochrones have a R^2>0.9. Fields with a signature represent bedrock data from the Periadriatic plutons (Blanckenburg et al., 1992; Kagami et al., 1991) and detrital apatites from recent rivers draining the Penninic nappes of the Lepontine Dome or the Silvretta-Seckau and Lower Austroalpine Nappes (Malusà et al., 2017). Data for pseudoisochrones: Drauzug-Gurktal Nappe System: Heinrichs et al. (2012); Schulz et al. (2004); Schuster et al. (2001); Thöni and Miller (2009); Tumiati et al. (2003); Koralpe-Wölz Nappe System: Habler et al. (2007); Habler et al. (2006); Heinrichs et al. (2012); Schulz et al. (2004); Schuster et al. (2001); Thöni (2003); Thöni (2006); Thöni and Jagoutz (1993); Thöni and Miller (1996); Thöni and Miller (2000); Thöni and Miller (2009); Thöni and Miller (2010); Ötztal-Bundschuh Nappe System: Bernhard et al. (1996); Habler et al. (2009); Hoinkes et al. (1997); Thöni and Miller (2004).